



University of HUDDERSFIELD

University of Huddersfield Repository

Taylor, Jordan

The Design of Helium Ion Accelerators for External Ion Beam Cancer Therapy

Original Citation

Taylor, Jordan (2018) The Design of Helium Ion Accelerators for External Ion Beam Cancer Therapy. Doctoral thesis, University of Huddersfield.

This version is available at <http://eprints.hud.ac.uk/id/eprint/35365/>

The University Repository is a digital collection of the research output of the University, available on Open Access. Copyright and Moral Rights for the items on this site are retained by the individual author and/or other copyright owners. Users may access full items free of charge; copies of full text items generally can be reproduced, displayed or performed and given to third parties in any format or medium for personal research or study, educational or not-for-profit purposes without prior permission or charge, provided:

- The authors, title and full bibliographic details is credited in any copy;
- A hyperlink and/or URL is included for the original metadata page; and
- The content is not changed in any way.

For more information, including our policy and submission procedure, please contact the Repository Team at: E.mailbox@hud.ac.uk.

<http://eprints.hud.ac.uk/>

The Design of Helium Ion Accelerators for External Ion Beam Cancer Therapy

University of
HUDDERSFIELD

Jordan Taylor

Centre for Doctoral Training in Next Generation Accelerators

International Institute for Accelerator Applications

University of Huddersfield

A thesis submitted to the University of Huddersfield
in partial fulfilment of the requirements for the degree of

Doctor of Philosophy

September 2018

Copyright

i. The author of this thesis (including any appendices and/or schedules to this thesis) owns any copyright in it (the “Copyright”) and he/she has given The University of Huddersfield the right to use such Copyright for any administrative, promotional, educational and/or teaching purposes.

ii. Copies of this thesis, either in full or in extracts, may be made only in accordance with the regulations of the University Library. Details of these regulations may be obtained from the Librarian. This page must form part of any such copies made.

iii. The ownership of any patents, designs, trade marks and any and all other intellectual property rights except for the Copyright (the “Intellectual Property Rights”) and any reproductions of copyright works, for example graphs and tables (“Reproduction”), which may be described in this thesis, may not be owned by the author and may be owned by third parties. Such Intellectual Property Rights and Reproductions cannot and must not be made available for use without the prior written permission of the owner(s) of the relevant Intellectual Property Rights and/or Reproductions.

Abstract

Currently protons and carbon ions are the only heavy charged particles used for radiotherapy. There is particular interest in the use of helium ions for therapy, as they present physical dose and clinical advantages over carbon ions and protons. In this thesis, a Fixed Field Alternating Gradient (FFAG) approach has been developed for helium ion therapy, which has never been explored before. Two non scaling FFAG accelerators are designed, accelerating He^{2+} ions to 900 MeV, the necessary energy to reach 30cm depth in tissue.

Initial steps have characterised the beam optics in order to achieve isochronous stable equilibrium orbits over the design energy range described above, whilst maintaining the working point with few resonance crossings. The desired energy range of the machine is split across two stages, of which both were successfully optimised to have a time of flight to within 1% of each other. A common operating RF frequency has been identified, and the RF parameters that are currently achievable were assessed and suitability for this design investigated. Having successfully chosen realistic RF parameters, a beam has been accelerated and it has been demonstrated that there is a sufficient dynamic aperture and extraction is possible.

The feasibility of a nsFFAG accelerator for the purposes of helium therapy has been successfully investigated, and a helium ion beam was successfully accelerated through simulation from 1 MeV to 900 MeV across two stages, using fixed frequency acceleration. The design is compact, though splitting the design into two machines has increased the footprint. However, the first stage has the potential to be used as a standalone facility for research and shallow tumours, and the accelerator could likely fit in a current radiotherapy bunker. Further work will need in depth design studies to model the magnetic field and RF cavity designs, to verify the design.

Acknowledgements

First and foremost I have to thank my supervisor Rob Edgecock for all of his support, time and patience throughout the project, for which I am truly grateful. Thank you. I also have to say thank you to Carol Johnstone, for the support over the years, conversations about lattice design, and providing access to FACT in order to develop them. further. I also extend my thanks to all of the staff at the IIAA, past and present, for all of the active discussions, support and ideas throughout my time at Huddersfield.

I would say that I will miss my office the most, but really it is the people within it. Norman, one pill makes you larger, and one pill makes you small. You may be a city fan, but you are alright really. Sam, I have missed your baking for a while, but more so your sarcasm. Thank you all for the support and fond memories.

Haroon. Many happy returns. Phrasing. This is all that is necessary here. Dave. Thanks for translating for me for all of these years, and I guess for all the years to come. You have helped me so much over the years, mentally and emotionally. Thank you.

I would not be in this position if it was not for my Dad, who continually has driven me up and down the country for my educational endeavours. You have never pushed me to do anything and have always supported every decision. Thanks Dad. Special thanks go out to the most wonderful woman in the world, Nan. You have raised me to be the person I am and taught me to always keep smiling.

Finally, my rock, Erika. Thank you for everything, especially for keeping me sane. I could not have achieved this without you.

Per Lei

Contents

List of Figures	10
List of Tables	13
1 Introduction	15
1.1 External beam radiotherapy: A history	15
1.1.1 Proton therapy	16
1.1.2 Proton therapy in the UK	16
1.2 Ion therapy	17
1.2.1 The limitations of ion beam therapy	18
1.3 Thesis layout	19
2 Radiation in cancer therapy	21
2.1 Biological rationale for radiotherapy	21
2.1.1 Linear energy transfer (LET)	22
2.1.2 Relative biological effectiveness (RBE)	22
2.1.3 Absorbed dose, equivalent dose and effective dose	23
2.2 Conventional radiotherapy	24
2.2.1 Photon interactions with matter	24
2.2.1.1 The photoelectric effect	24
2.2.1.2 Compton Scattering	25
2.2.1.3 Pair production	26
2.2.2 Current status of radiotherapy	26
2.3 Proton therapy	27
2.3.1 Charged particle interactions with matter	28
2.3.2 Charged particle collisional losses	29

2.3.2.1	Nuclear interactions	30
2.3.3	Multi-Coulomb scattering	30
2.3.4	Electron interactions with matter	31
2.3.5	Current status of proton therapy	32
2.3.5.1	Current proton therapy solutions	34
2.4	Ion therapy	34
2.4.1	Carbon ion facilities	35
2.4.1.1	Fragmentation	36
2.4.2	Alternative ions	37
2.5	Helium ion therapy	38
2.6	Chapter summary	38
3	Accelerator theoretical background	39
3.1	Electrostatic acceleration	39
3.1.1	Cockcroft Walton generator	39
3.1.2	Van de Graaff accelerator	40
3.1.3	Tandem accelerator	41
3.1.4	Limitations of electrostatic acceleration	42
3.2	RF acceleration	42
3.3	Classic cyclotron	43
3.3.1	Weak focusing	45
3.4	Isochronous or AVF cyclotrons	46
3.5	Betatron motion and tunes	48
3.5.1	Resonances	49
3.6	Synchrocyclotron	49
3.7	Synchrotron	50
3.8	Accelerators used for particle therapy	51
3.9	Fixed Field Alternating Gradient (FFAG) accelerators	51
3.9.1	Scaling FFAG	53
3.9.2	Non-scaling (ns) FFAG	53
3.9.3	Current scaling FFAGs	54
3.9.4	Current nsFFAGs	55
3.9.5	FFAG designs for charged particle therapy	55

CONTENTS

4	Methods	57
4.1	COSY infinity	57
4.1.1	FACT	57
4.2	OPAL	59
5	Initial characterisation of beam optics for nsFFAG designs	61
5.1	Design parameters	62
5.2	Field map optimisation	62
5.2.1	Initial map generation	62
5.2.2	Optimisation using FACT	63
5.3	FFAG design 1	64
5.4	Stage 1 design	67
5.4.1	Stage 1 further development	69
5.5	HEATHER Stage 1 final design	71
5.6	HEATHER stage 2 design	74
5.6.1	Differences between stage 1 and stage 2	79
5.7	Stage 2 final design	79
5.8	Chapter summary	80
6	Acceleration studies and RF Characterisation	83
6.1	RF in Cyclotrons	83
6.2	Kilpatrick limit	85
6.2.1	Harmonics	86
6.2.2	Transit time factor	87
6.2.3	Current separate sector machines and their RF	89
6.3	HEATHER RF Studies	91
6.3.1	HEATHER RF operating frequency selection	91
6.3.2	Optimisation of the acceleration orbit	94
6.4	Realistic RF acceleration	100
6.5	Stage 2 RF	103
6.6	Chapter Summary	104
7	Beam Acceleration and Extraction Studies	105
7.1	Pre-acceleration	105

7.2	Emittance	106
7.3	Stage 1 Beam Acceleration	107
7.4	Cyclotron Extraction	111
7.5	Stage 1 Extraction	112
7.6	Stage 2 Beam Acceleration	114
7.7	Magnetic Field Error	118
	7.7.1 Stage $\pm 1\%$ error field map	118
	7.7.2 Stage 1 fixed error field map	120
8	Conclusions	121
8.1	Future work	122
	8.1.1 Particle source and pre acceleration	122
	8.1.2 Transfer lines	122
	8.1.3 Magnet design	123
	8.1.4 RF design	123
	8.1.5 Variable Energy	124
	8.1.6 Extraction	125
	8.1.7 Beyond the current design	125
8.2	Summary	125
A	Appendix	127
A.1	Enge Edge	127
A.2	Kilpatrick equation	128
	References	129

Total word count: 29516

List of Figures

2.1	A depiction of the dominant photon interaction for a given photon energy for varying absorber atomic number [30]	25
2.2	The percentage depth dose curve for 6 MeV photons [33]	27
2.3	A depiction of protons, photons and electrons relative dose deposition in terms of entrance dose as a function of depth in tissue [39]	28
2.4	Taken from [42]. Quantities used to describe multiple Coulomb scattering. The particle is incident in the plane of the figure	31
2.5	The bending radius necessary to bend the beam against kinetic energy for fully stripped ions up to carbon. The energy necessary to reach 30cm depth in water was calculated using SRIM [43]	33
2.6	The Heidelberg Ion-beam Therapy Center rotating gantry [63]	36
2.7	A depiction of the relative dose as a function of depth for different ions. As the mass of the ion increases, the fragmentation dose tail increases distally to the tumour [64]	37
3.1	The Cockcroft Walton generator	40
3.2	The Van de Graaff Generator	41
3.3	An example tandem accelerator [78]	42
3.4	Ernest Lawrence's cyclotron in 1932 [14]	44
3.5	A figure taken depicting the concept of weak focusing for different field index, n <i>K. Strijckmans(2001)</i>	45
3.6	a) shows the visible hills and valleys in an isochronous cyclotron, and b) shows the magnetic field amplitude as a function of azimuthal angle [82]	47
3.7	A depiction of the FODO lattice [85]	50
3.8	The first FFAG at MURA in 1956 [88]	52
3.9	The first two Japanese FFAG accelerators designed and built in KEK .	55
3.10	An image of the EMMA accelerator [100]	56
5.1	nsFFAG accelerator layout provided by C. Johnstone	65

LIST OF FIGURES

5.2	A nsFFAG accelerator layout provided by C. Johnstone. On both Figures, red represents the values before optimisation and black afterwards	66
5.3	Different accelerator layouts provided by C. Johnstone that were optimised	67
5.4	Initial ToF results from extending the design radius of the Proton Isotope Producer (PIP), a different FFAG design within the collaboration [108]	68
5.5	Isochronicity profile for Stage 1 (extended PIP) for various iterations detailing the progression made	69
5.6	Final optimised iteration of stage 1 (Extended PIP) tune map detailing the movement of the working point of the machine	70
5.7	Final optimised geometry of stage 1	72
5.8	The azimuthal magnetic field gradient for stage 1	73
5.9	Stage 1 isochronicity profile from 1 MeV to 400 MeV comparing results from FACT and OPAL	74
5.10	Comparison of the working point for stage 1 in FACT and OPAL	75
5.11	A depiction of the concept of putting the straight into stage 1	76
5.12	A depiction of the concept of putting the straight into stage 1 for different iterations of the design	77
5.13	ToF profile for iterations for the energy range 200 MeV to 900 MeV.	78
5.14	Stage 2 version 1 with an energy range from 400 MeV to 900 MeV	78
5.15	Stage 2 finalised physical parameters	80
5.16	The isochronicity profile across the acceleration regime for stage 2 comparing COSY and OPAL	81
5.17	The tune diagram showing the working point for stage 2, comparing results from COSY and OPAL.	82
6.1	Frequency as a function of energy based on the empirical data by W D Kilpatrick [25]	86
6.2	Maximum surface voltage achievable before breakdown occurs for different harmonics and accelerating gap sizes	88
6.3	Separate sector cyclotrons at the Paul Sherrer Institut, Switzerland	89
6.4	The RIKEN facility	90
6.5	Highlighted magnet and cavity dimensions for stage 1 and stage 2 of HEATHER	92
6.6	The largest phase slip measured across the acceleration regime for different RF frequencies for stage 1 and stage 2	93
6.7	A depiction of a quadrant of stage 1, The injection angle is highlighted.	95

LIST OF FIGURES

6.8	The beam acceleration path before and after optimisation of the injection parameters	96
6.9	The difference in mm between successive orbits before and after optimisation of the injection parameters	97
6.10	the phase of the particle relative to the RF phase before and after optimisation	98
6.11	A comparison separation between orbits for a given point at 45° degrees before and after optimisation	98
6.12	HEATHER RF phase space plots showing the phase acceptance	99
6.13	The configuration of the delta type double gap $\lambda/2$ resonator simulated in OPAL	101
6.14	The configuration of the delta type double gap $\lambda/2$ resonator simulated in OPAL	102
6.15	HEATHER stage 1 RF phase space plots for delta type double gap resonators with different accelerating gap voltages	103
6.16	HEATHER stage 2 RF phase space plots for single type double gap resonators with different accelerating gap voltages	104
7.1	Depiction of emittance, adapted from [127]	106
7.2	The maximum emittance observed in each plane as a function of beam with using the same initial injected emittance of 1π mmmmrad simulated in OPAL	108
7.3	The optimised emittance as a function of energy for each plane from an initial injected emittance of 1π mmmmrad in each plane simulated in OPAL	109
7.4	Stage 1 emittance profile for different initial injected emittances	110
7.5	A depiction of cyclotron extraction by use of a septum, taken from [128]	111
7.6	Radial successive orbit separation per turn for different injected beam sizes	113
7.7	The radial profile of a He^{2+} beam for the last 5 turns for different initial beam sizes	114
7.8	The radial profile of a He^{2+} beam for the last 5 turns for an He^{2+} beam with an initial emittance of 5π mmmmrad	115
7.9	Stage 2 emittance growth across the acceleration regime	116
7.10	The radial profile of a He^{2+} beam from stage 1 with initial emittance of 2π mmmmrad optimised to make the peaks equidistant	117
7.11	The radial profile of a He^{2+} beam from stage 1 with initial emittance of 2π mmmmrad optimised to maximise the extraction peak separation orbit	117

7.12	Stable orbit properties introducing 1% error on the magnetic field . . .	119
7.13	The RF phase space with an introduced percentage error. The accelerated is unstable, and the design energy is not reached when changing the initial phase of the particle	119
7.14	Depiction of the RF phase space with different fixed additional magnetic field error	120
8.1	Magnet design work for PIP, a different FFAG design within the collaboration [108] [137].	123
8.2	MCNPX simulations on the Front End Test Stand (FETS) beam dump for shielding purposes	124

List of Tables

6.1	Efficiency factor for varying harmonics for the delta type resonator angle of 40°	100
-----	---	-----

LIST OF TABLES

1

Introduction

In this thesis the design of a novel compact accelerator, a non-scaling (ns) Fixed Field Alternating Gradient accelerator (FFAG), is developed for therapy using light ion beams; with a particular focus on helium ions. By using an ion lighter than carbon, the size of the accelerator can be reduced, increasing the likelihood the machine will fit in currently established hospitals.

In 2015 cancer was the cause of death for more than one in four people, and in England and Wales only 50% of people diagnosed with cancer survive for ten years or more [1]. Radiotherapy is the 2nd most effective method of treating cancer after surgery in the UK with 40% of patients receiving radiotherapy as part of their treatment plan [2]; however globally this is 50% [3] [4].

1.1 External beam radiotherapy: A history

Ionising radiation has been used medically for just over a century since its discovery, beginning with Wilhelm Röntgen in 1885 where he used x-rays to image the hand of his wife [5]. Just over a decade later Victor Despeignes irradiated a patient to treat a stomach tumour [6], becoming the first recorded case of ionising radiation used to treat cancer [7] [8]. Particle accelerators have played a part in radiotherapy since Cockcroft and Walton's 1932 high voltage generator [9], where less than a decade later in 1937 they were used to generate mega electronvolt (MeV) X-rays to investigate the biological effects of higher energy X-rays [10] [11]. Greater energies beyond 1 MeV were surpassed with the help of particle accelerators again, by accelerating electrons using linear accelerators or linacs. The first radiotherapy treatment facility was built in the Hammersmith hospital, London, UK delivering 8 MV x-rays in 1953 [11] [12]. 65 years

1. INTRODUCTION

later, linacs have advanced with technology and are the work horses of radiotherapy globally.

1.1.1 Proton therapy

Proton therapy is becoming an increasingly popular radiotherapy modality, offering more conformality than conventional treatment. In 1946 Robert Wilson stated that high energy protons could reach useful depths in tissue and be used therapeutically, and the way protons interact with matter could be taken advantage of [13]. The difference in the mechanisms that cause energy loss between protons and x-rays make protons more suitable to irradiate tumours proximal to critical structures, as they can be controlled to deliver a peak dose at a desired depth. The principles stated by Wilson 60 years ago are still true to this day and are discussed in detail in Chapter 3.

The Cockcroft Walton generator was designed to accelerate protons for nuclear physics experiments. However, at the several hundred kV_p generated the penetrative distance of protons in tissue was negligible in comparison to x-rays and were overlooked as a treatment modality. The development of particle accelerators, in particular the cyclotron created by Earnest Lawrence [14], led to larger cyclotrons, and with them protons in excess of 100 MeV being produced. It was at this point that Wilson identified the potential protons have as a treatment modality. Less than a decade later, the first patient was treated with external beam proton therapy at Lawrence Berkeley National Laboratory (LBNL) in 1954 [15]; a year after the first medical linac was built. Patients were continually treated in excess of 30 years at nuclear laboratories across the world, before it was approved as a method to treat cancer in 1988 by U.S. Food and Drug Administration (FDA) in the US, and dedicated proton therapy facilities started to appear. The first medical proton therapy facility was again built in the UK, at the Clatterbridge centre for ocular tumours [16]. In the last 30 years another 69 proton therapy facilities globally have become operational, and since the first patient approximately 150,000 patients have received proton therapy up to the end of 2016 [17].

1.1.2 Proton therapy in the UK

The first medical proton therapy facility in the UK, was built at the Clatterbridge Centre for ocular tumours [16]. Due to the size of the eye, only a small penetrative depth is necessary. The facility provides a 60MeV proton beam, which reaches a depth of up to 3.1mm in water. It has taken the UK nearly 30 years since Clatterbridge to

construct a full energy proton beam facility, the first being a privately constructed in 2018 by Proton Partners International (PPI) in Newport, Wales [18].

As a treatment modality, full proton beam therapy was not available for patients until April 2008, where the NHS introduced an overseas funded scheme for patients that met specific clinical criteria. The scheme would send patients and families abroad for up to 10 weeks to receive treatment in a facility abroad and has successfully treated over 1000 patients [19] [20]. In 2015 the UK approved the construction of two NHS proton therapy facilities, the Christie in Manchester, and University College London Hospitals (UCLH). The Christie is hoping to treat their first patient this year, while UCLH are planning the treatment of their first patient in 2020. Each centre hopes to deliver treatment to 750 patients per year, greatly increasing the option of the treatment modality for patients in the UK.

PPI are a private company also offering proton therapy and as mentioned delivered the first full proton beam therapy in the UK. PPI have two more sites planned within the UK, one in located in Borsmund, and the other located in the Thames Valley. It is understood that these centres will be accepting NHS patients.

1.2 Ion therapy

The term ion therapy refers to ions heavier than protons used for external beam radiotherapy, but at the time of writing is specific to carbon ions; as no other ions are used clinically for the treatment of cancer [21]. The physical effects of protons identified by Wilson in 1946 are mass dependent and can be amplified when heavier ions are used. The use of heavier ions provides an even more localised dose and have a greater biological effect.

The first use of ions as a treatment modality came in 1975 with the construction of the BEVALAC at LBNL in 1975 [22]. Around 3000 patients were treated with different ion species: carbon, neon, silicon, argon and helium between 1975 and 1993. The results indicated the potential of carbon and neon beams, which led to the development of the first dedicated carbon ion medical facility at the National Institute of Radiological Sciences (NIRS) in Japan in 1984 [23]. The heavy ion medical accelerator (HIMAC) treated its first patient in 1994. Since then, another 10 carbon ion medical facilities are in operation, totalling 11 globally. Over 20000 patients have been treated with carbon ions since the construction of HIMAC up to the end of 2016 [17].

1. INTRODUCTION

1.2.1 The limitations of ion beam therapy

The limitation in using particles for therapy lies with the accelerators necessary to achieve the energies for therapeutic beams; the different types of accelerator will be discussed in more detail in Chapter 3. As the mass of the particle species increases, they require more energy to achieve the same penetrative depth in tissue. The difficulty of delivering these energies can be interpreted by the number of patients treated since the method has been available. Approximately 170,000 patients have been treated globally with protons and carbon ions since up to the end of 2016, whereas in the UK alone, 134,000 patients were treated with conventional radiotherapy in 2015-2016 [24].

Proton therapy accelerators are decreasing in size and the number of facilities being installed in current hospitals is increasing. UCLH demonstrate this by installing a proton beam facility in central London. Typically, cyclotrons are used, and MEVION offer a one room cyclotron solution with a gantry that can fit in a current radiotherapy bunker, the size of which is approximately 50m². Ion therapy accelerators however require much larger facilities, typically a new site is needed as they are too large to fit in current hospitals. All of the ion therapy accelerators globally are large synchrotrons and the accelerator alone requires approximately 6.5 times the space of a current conventional radiotherapy bunker. Ions lighter than carbon are easier to accelerate, the reduced particle mass requires less force to bend the particle. This allows for a smaller accelerator and hence reduced cost.

When using carbon ions therapeutically, a large number of low Z secondaries are produced and travel beyond the range of primary ion. The secondary particles are produced by fragmentation, the breakup of a primary ion via an inelastic nuclear interaction with tissue. These secondary particles may travel beyond the range of the primary ion and create a dose tail. This is undesirable for tumours situated proximal to a radiosensitive structure, as it will be damaged by the dose tail. The number of secondaries produced can be reduced by using a lower Z ion instead of carbon.

A potential solution to reduce the size of an ion therapy facility would be to use a lighter ion species. A lighter ion species would also reduce the fragmentation dose tail. Helium is the easiest ion to accelerate after protons, and is a compromise between carbon and protons, yet still obtaining advantages of ion therapy.

This thesis represents a feasibility study of the acceleration of helium He²⁺ ions using a nsFFAG accelerator. Ultimately size is cost, and using a nsFFAG accelerator will potentially allow for smaller accelerator and an overall reduced footprint, and hence a reduced cost. Ideally the accelerator will need to have a comparable footprint and

cost to conventional radiotherapy suite and be able to fit comfortably inside a hospital.

The questions to be answered are whether it is possible to accelerate an isochronous helium beam, are FFAGs a technically feasible option for therapy with helium and how would their performance and cost compare with other possible options.

1.3 Thesis layout

Chapter 2 addresses the core principles of the interaction of radiation with matter, detailing the advantages of charged particles over x-rays for the treatment of cancer. The chapter then discusses some of the current shortfalls of ion therapy, and how helium may be a potential solution for some of the issues. Chapter 3 concentrates on the fundamentals of accelerator physics and the types of accelerators currently used to accelerate particles for therapy. Fixed Field Alternating Gradient (FFAG) accelerators are introduced and how they are suitable for accelerating ions for therapy. Chapter 4 begins looking at different design iterations for a helium ion accelerator, specifically focusing on the time of flight (ToF) and resonant instabilities of the accelerator to achieve isochronous acceleration to relevant clinical depths. Chapter 5 builds on the designs developed in Chapter 4, simulating the addition of RF cavities, and identifying the stable acceleration orbit. Considerations are made to identify realistic RF parameters using the Kilpatrick limit [25] and by assessing the RF in similar operating machines. Chapter 6 then looks at accelerating a typical beam from similar machines through the accelerator and extracting the beam when it has reached its design energy. To assess the extraction of the beam the orbit separation is discussed, and the injection parameters are optimised to maximise orbit separation between the last two orbits.

1. INTRODUCTION

2

Radiation in cancer therapy

Radiotherapy describes the use of controlled ionising radiation to purposely damage unwanted cells in an attempt to kill them. In this chapter, the biological rationale for radiotherapy will be discussed, and some terminology relating the physics to the biology will be addressed. The interaction of radiation types with matter will be discussed, to explain the science behind the choice of different radiation types for the treatment of cancer. The limitations will be explored, and the current status of proton and ion beam therapy will be discussed in detail, before highlighting why helium may be the compromise necessary to increase the availability of ion therapy.

2.1 Biological rationale for radiotherapy

Many radiation types interact with matter and deposit energy via ionisation. Ionisation within a cell can trigger chemical reactions, which in turn damage critical structures within the cell, namely the DNA.

DNA consists of two polynucleotide strands joined in a helical structure by a covalent bond. If it becomes damaged, breaks appear in either or both strands of the DNA, identified as single strand or double strand breaks. Eventually when the cell replicates, it will be unable to do so as the DNA of a cell is damaged. The cell will try to repair the DNA through different repair mechanisms, which may be successful, partially successful or fail. A successful repair will present the DNA as if there was no interaction with radiation, a partial repair introduces a mutation that does not impair cell function, and failure to repair results in cell death. Both single and double strand breaks can be repaired, but it is more difficult to repair a double strand break and the likely result from an incorrect double strand break repair is cell death.

2. RADIATION IN CANCER THERAPY

Radiation can damage the DNA structure of a cell by either direct or indirect damage. Direct damage is when the radiation type directly interacts with the DNA in the cell. Indirect ionisation refers to the ionisation of water, which is the majority of the structure of cells. Ionising water creates free radicals in the cells which eventually damage the DNA and produce single strand breaks. As direct ionisation is more likely to result in double strand breaks and hence cell death, it is the desired outcome of radiotherapy.

To increase the chance of direct ionisation, a larger amount of ionisation is needed on a cellular level, or by using more densely ionising radiation. The amount of ionisation per unit distance for a specific radiation type is described by the LET; the linear Energy Transfer.

2.1.1 Linear energy transfer (LET)

Linear energy transfer (LET) is equivalent to the stopping power (dE/dx) in physics and quantifies the amount of energy deposition per unit distance. At therapeutic energies, deposition for radiation comes in the form of ionisation, so densely ionising radiation has an increased LET. LET can be used as a tool to create treatment plans, but it is complex due to the variation of LET as a function of energy [26].

A detailed discussion of LET is beyond the scope of this thesis, but it is important to note that the evidence suggests a strong correlation between cell death and high LET. [27] [28].

2.1.2 Relative biological effectiveness (RBE)

The term relative biological effectiveness (RBE) is used to relate the effects of one ionising radiation type to another. For a given amount of biological damage to a particular type of tissue, the RBE is the ratio of the absorbed dose, D_T for one radiation relative to another radiation type, as demonstrated by Equation 2.1.

$$RBE = \frac{D_{T1}}{D_{T2}} \quad (2.1)$$

RBE is set to 1 for photons and 1.1 for protons for therapeutic energies. The LET for particles is dependent on its energy and as a result the RBE for protons arguably changes with respect to its LET and how densely ionising it is. However, it should be noted the literature agrees there is a positive correlation between RBE and LET i.e. particles with an increased ionisation density deliver more biological damage compared

to x-rays for the same absorbed dose. Like LET a detailed discussion of RBE is beyond the scope of this thesis [29].

2.1.3 Absorbed dose, equivalent dose and effective dose

Radiation dose describes the energy deposited from radiation into tissue. Equation 2.2 describes the absorbed dose; the energy deposition per unit volume. The SI unit for dose is Gray (Gy), where 1 Gray is 1 joule of energy is deposited in 1 kilogram of mass [30].

$$D_T = \frac{1J}{1kg} \quad (2.2)$$

Absorbed dose, however, does not account for the radiation type causing the dose, which may result in different effects quantified by weighting or quality factors. The quality factors are based on experimental RBE values for cancer induction at low doses and rates [31] [32]. To quantify the biological difference in dose by different radiation types the term equivalent dose is used. Equivalent dose it calculated by multiplying the absorbed dose by the radiation weighting factor for the radiation type, as shown in Equation 2.3.

$$H_T = D_T \times W_R \quad (2.3)$$

Where H_T is the Equivalent dose which is measured in Sieverts (Sv), D_T is the absorbed dose and W_R is the radiation weighting factor.

Certain organs or areas of the body are more sensitive to radiation than others, and different quantities of equivalent dose translate to a different biological effect. The Effective dose, E_T , is calculated by multiplying the equivalent dose by the tissue weighting factor W_T as demonstrated by Equation 2.4. Effective dose is also measured in Sieverts.

$$E_T = W_T \times H_T \quad (2.4)$$

The damage from radiation to healthy cells is split down two pathways, deterministic and stochastic. Deterministic effects are seen when a certain amount of radiation has been absorbed by tissue and there is sufficient cell death to impair function. Examples of deterministic effects would be epilation or radiation sickness. Stochastic effects are probabilistic effects that increase in probability linearly with the amount of dose absorbed. Deterministic effects in therapy are normally acute. Stochastic effects relate to the chance of secondary malignancies via the generation of mutations in DNA repair.

2. RADIATION IN CANCER THERAPY

When constructing treatment plans both types of damage are considered to spare as much damage to healthy tissue as possible [31].

2.2 Conventional radiotherapy

When radiation traverses a material, it will lose energy on its path, which mostly comes from ionisation. The ionisation mechanism is the process of gaining or losing an electron from an atom, creating an ion.

Ionisation can occur directly when a charged particle passes through a medium. It is also possible to ionise indirectly where ionisation occurs from the production of secondary charged particles. Indirect ionisation is generally associated with neutral particles, like neutrons or photons, as they are unable to ionise directly. Particles that are indirectly ionising may not interact with the medium and its presence would never be known, whereas for a charged particle this is not the case. The most common type of radiotherapy, conventional radiotherapy, uses x-rays to damage cells. Conventional radiotherapy has been successfully used for many years, but the desire to look at other directly ionising radiation types for radiotherapy is rapidly increasing; especially for external beam treatments. The rationale for looking at other radiation types can be explained by looking at the way photons interact with matter.

2.2.1 Photon interactions with matter

Photons (x-rays) ionise indirectly because they are chargeless, massless packets of energy and produce secondary charged particles to ionise a material. The intensity of a beam of photons attenuates as they travel through a medium and this gradual energy loss is through three different energy dependent interactions; the photoelectric effect, Compton scattering and pair production. Depending on the energy of the incident photon and the Z value of the material traversed, one type of interaction will dominate as depicted in Figure 2.1.

2.2.1.1 The photoelectric effect

At low energy the Photoelectric effect dominates, and it describes the liberation of electrons from a material, called photoelectrons. In this process a photon interacts with an electron in the medium and its energy is wholly absorbed by the electron. Providing the energy of the photon is at least equal to the binding energy of the electron, a photoelectron will be emitted. If the absorbed photon has an energy greater than that of the

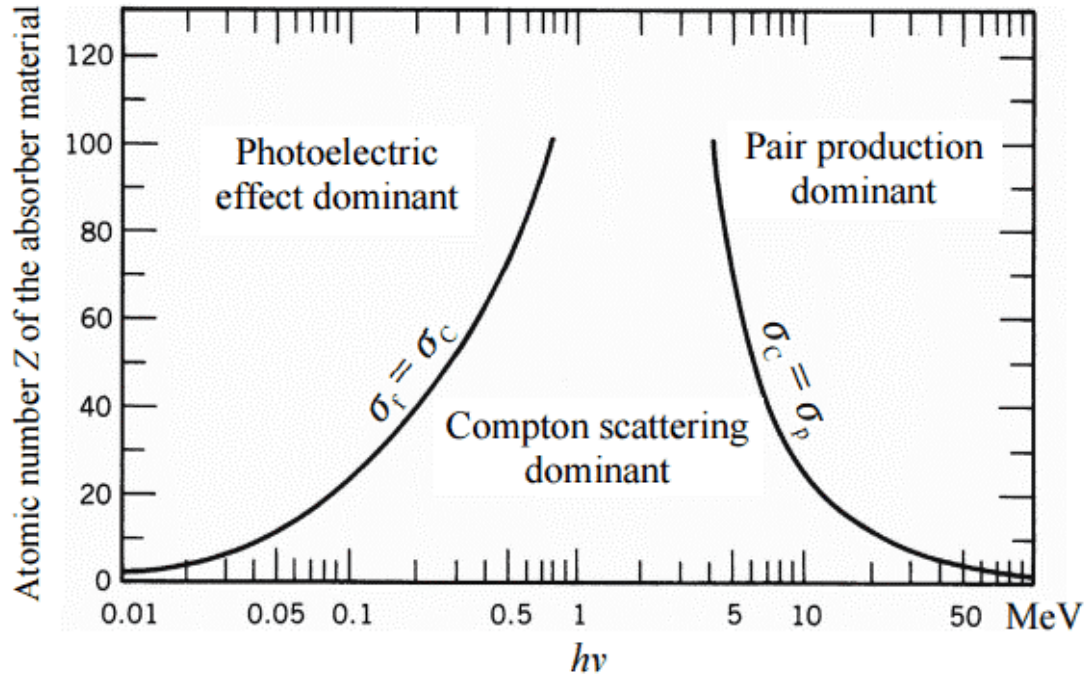


Figure 2.1: A depiction of the dominant photon interaction for a given photon energy for varying absorber atomic number [30]

binding energy, the remaining energy will become kinetic energy for the electron. If the energy of the photon is less than the binding energy of the electron the energy will still be absorbed and the electron will likely move to an excited state and return to a lower state, releasing the energy via spontaneous emission. The photoelectric effect requires a threshold Energy of light to create photoelectrons and is independent of the intensity of the light source below the threshold Energy. For all intents and purposes this is true, because the energy that is absorbed is held for a very short period. However, if the intensity was high enough so that two or more photons could be absorbed by the same electron before spontaneous emission or kinetic energy loss occurred, photo emission can be observed.

2.2.1.2 Compton Scattering

As the energy increases Compton scattering becomes the dominating process between photons and electrons. Like the photoelectric effect the photon imparts energy to the electron, but instead of the photon being absorbed, it gets scattered by an angle θ . The electron is always ejected in this interaction, at a different angle to the photon, ensuring

2. RADIATION IN CANCER THERAPY

energy and momentum is conserved. The angle in which the photon is scattered relates to the energy lost. This relationship is expressed in Equation 2.5

$$E_{\gamma'} = \frac{E_{\gamma}}{1 + \frac{E_{\gamma}}{m_e c^2}(1 - \cos\theta)} \quad (2.5)$$

Where E_{γ} is the energy of the incident photon, $E_{\gamma'}$ is the Energy of the scattered photon, m_e is the electron rest mass, c is the speed of light and θ is the scattering angle.

2.2.1.3 Pair production

As the energy of the incident photon increases beyond 1.02 MeV the pair production process begins to dominate. The pair production process occurs when the incident photon converts to an electron and positron pair; hence the photon energy must be greater than or equal to the rest mass of both particles. Energy and momentum must be conserved in this process, so the interaction needs to happen near a nucleus to conserve momentum as it is forbidden in free space. The created positron will eventually lose all its kinetic energy via moderation and annihilate with an electron. Annihilation is the name given to collision between a particle and its anti-particle to produce new particles; momentum, energy and charge must be conserved. In this case the electron and positron will annihilate at rest, and the resulting particles will be two back to back photons each with the energy equivalent to 511 keV to conserve energy and momentum.

The electrons produced from the above processes further ionise the material, and deposit energy. The Energy deposition of electrons is accountable for all of the ionisation from photons and will be discussed later in this chapter in Section 2.3.4.

The three energy loss processes create the depth dose profile depicted in Figure 2.2. Typically, up to 10 MeV photons are used currently in radiotherapy. Photons do not stop unless all of their energy has been lost as described in the processes above. Depending on the depth of the tumour, the dose received from photons will change, and there will always be unwanted dose delivered to healthy tissue.

2.2.2 Current status of radiotherapy

The irradiation of healthy tissue is generally the limiting factor of a treatment plan, and the balance between delivered tumour dose and healthy tissue complications caused by dose are considered [34] [35]. This is undesirable, and can cause side effects depending on where the radiation is being delivered for treatment [34] [36]. The advances of

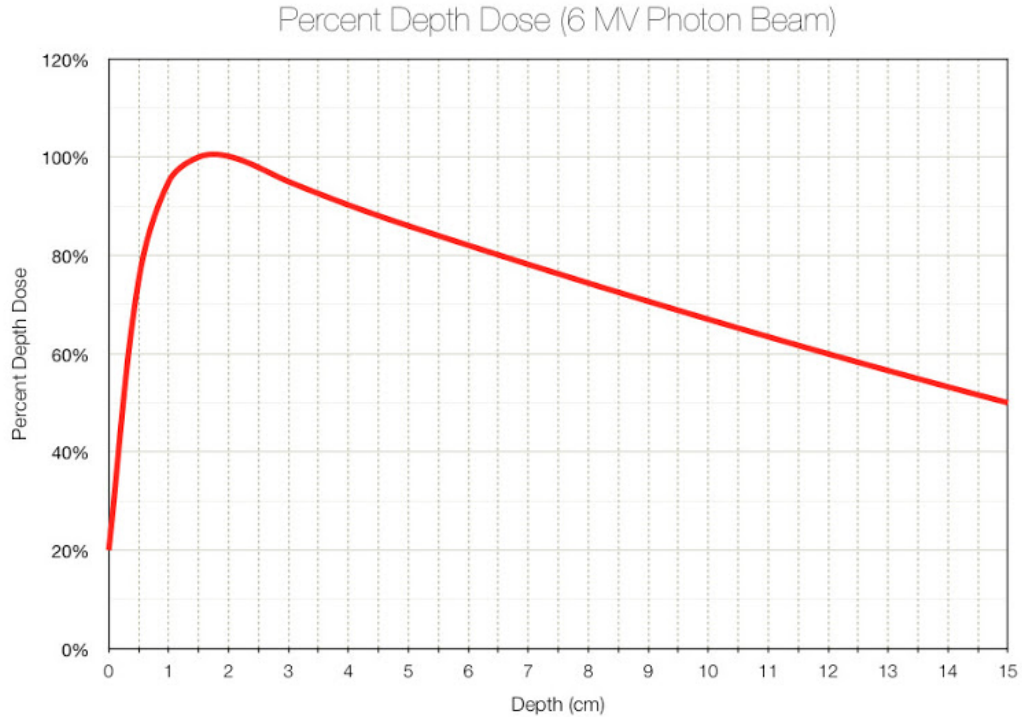


Figure 2.2: The percentage depth dose curve for 6 MeV photons [33]

radiotherapy have reduced the irradiation of healthy tissue by introducing multileaf collimators or conformal radiotherapy, image guided radiotherapy (IGRT) [37], and intensity modulated radiotherapy (IMRT). IMRT utilizes multiple beams of different profiles and intensities to reduce the dose to healthy tissue and deliver a more conformal dose to the tumour [38]. Current IMRT modulates the beam as the linac rotates around the patient, known as volumetric arc therapy (VMAT) or RapidArc®. This increases conformality as many more angles are utilised and reduces treatment time as the linac is not stopping and starting to set up for different angles. However due to the dose profile shown in 2.2, further changes are required increase conformality.

2.3 Proton therapy

Figure 2.3 compares the relative dose as a function of depth for protons (red) and photons (purple) for a single beam. A protons range is dictated by its energy and can be controlled to stop at a given point, known as the Bragg peak. The Bragg peak

2. RADIATION IN CANCER THERAPY

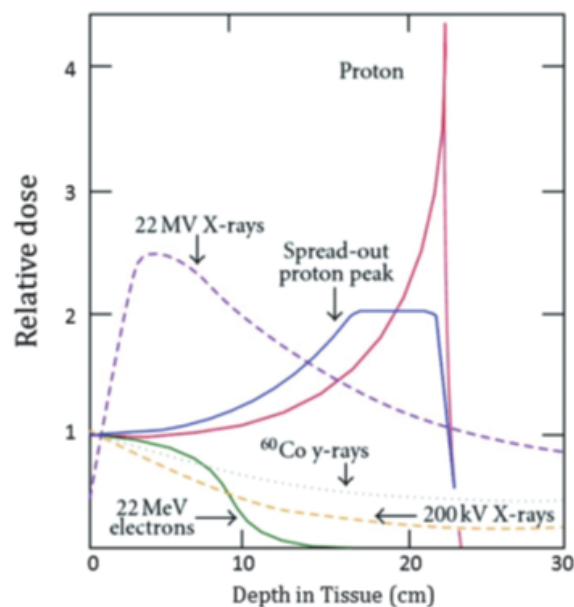


Figure 2.3: A depiction of protons, photons and electrons relative dose deposition in terms of entrance dose as a function of depth in tissue [39]

is also the highest region of dose deposition for protons, contrary to photons where peak radiation dose for photons is delivered near the surface of the medium. The fact that protons stop as opposed to continually ionising a material is a huge advantage over photons. This is especially crucial when irradiating a tumour proximal to radiosensitive organs, identified as organs at risk (OAR), where a photon beam would continue to ionise the material until sufficiently attenuated. The blue line on Figure 2.3 shows the depth dose curve for the spread out Bragg peak (SOBP). By using a single proton beam, the resultant peak is narrow and may partially irradiate the tumour. To ensure full tumour coverage, it is possible to use several energy modulated proton beams to create a flat wide dose plateau, identified as the SOBP. Protons are directly ionising, and have a higher LET compared to photons, hence increased chance of causing cell death. The depth dose curve for protons can be explained by the way charged particles interact with matter.

2.3.1 Charged particle interactions with matter

Charged particles interact with matter elastically and inelastically, where in both cases the momentum is always conserved. Elastic collisions can occur with either the nucleus

or other electrons within the material, conserving the total kinetic energy. Inelastic collisions occur when kinetic energy is not conserved as the particles lose kinetic energy. Charged particles lose kinetic energy from two main processes; collisional and radiative processes. These are energy dependent processes and relative to the incident particles mass. Radiative energy loss requires particles to be highly relativistic, which is not within the scope for heavy charged particles used for therapy. Electrons specifically may exhibit radiative losses depending on their energy, which will be discussed later in this chapter.

Collisional and radiative interactions will happen until the incident particle has lost all its kinetic energy to the medium. This process is generally simplified to represent the amount of energy lost per unit distance for a given medium, known as stopping power, which is the sum of the energy lost from collisional and radiative processes combined.

2.3.2 Charged particle collisional losses

The incident charged particle has a Coulomb field, and when it traverses a material it affects the surrounding charged particles by repulsion or attraction. The generated Coulomb forces between the incident and surrounding particles transfer kinetic energy, which scatters the particle inelastically. Inelastic scattering with the orbital electrons, known as electronic collisions, may transfer enough energy to excite or ionise the atom. Like the outcome of the photoelectric effect, the energy received by orbital electrons allow them to rise to an excited state, and then potentially de-excite releasing photons. If an outer electron receives enough energy it may be ejected from the atom, creating an ion. The process of energy loss through electronic collisions is well understood and described by the Bethe Bloche equation

$$-\frac{dE}{dx} = Kz^2 \frac{Z}{A} \left[\frac{1}{\beta^2} \frac{1}{2} \ln \frac{2m_e c^2 \beta^2 \gamma^2 T_{max}}{I^2} - \frac{\delta(\beta\gamma)}{2} \right] \quad (2.6)$$

where x is the distance traveled by the particle, $K = 4\pi N_A r_e^2 m_e c^2$, N_A is Avogadro's number, r_e is the electron radius, A is the atomic mass of the absorber in gmol^{-1} , z is the charge of the incident particle, Z is the Atomic number of the absorber, $\beta = v/c$, the ratio of the incident particle to the speed of light, γ is the Lorentz factor, I is the mean excitation energy of the medium, $\delta(\beta\gamma)/2$ is the density correction and T_{max} is the maximum kinetic energy that can be lost in a head on collision with a particle, as detailed in Equation 2.7.

The Bethe Bloch Equation is only suitable for ions with a mass much greater than electrons. This is because electronic losses are more significant for electrons. Electronic

2. RADIATION IN CANCER THERAPY

collisions are the main source of energy loss for charged particles traversing a medium in the range of therapy. The energy lost by a proton is stochastic, but the maximum energy it can lose would be in a head on collision with an electron. The energy dependent maximum kinetic energy loss for an electronic collision is written in Equation 2.7. It can be noted that for a given material the rate of energy loss essentially is a function of β , and when the particle slows down, the rate of energy loss increases; hence the Bragg Peak.

$$T_{max} = \frac{2m_e c^2 z \gamma^2 \beta^2}{1 + \frac{2m_e \gamma}{m} + \left(\frac{m_e}{m}\right)^2} \quad (2.7)$$

where m is the mass of the incident particle, everything else is as described.

Because collisions are random, maximum energy loss is not guaranteed, and the range of the particle may vary due to the number of collisions it encounters. This is known as range straggling, and needs to be accounted for in proton therapy, especially through different tissue types and thicknesses. The range of a ion is identified at the depth where 50% of all ions in the pulse have stopped [26].

2.3.2.1 Nuclear interactions

There is also the possibility that the incident charged particle will undergo nuclear reactions with nuclei; an irreversible non elastic interaction. This gives rise to unwanted secondary particles being produced that have the potential to travel beyond the Bragg peak. The produced unwanted secondaries will contribute to the overall dose and effect the RBE [40]. A summary of nuclear reaction data relevant to proton therapy can be found in ICRU report no.63 [41].

2.3.3 Multi-Coulomb scattering

As discussed, elastic scattering occurs when the incident particle is scattered by the electrons or nuclei present in the traversing material, conserving kinetic energy. In the case of particle therapy, the traveling medium will be large, and the likelihood is many scattering incidences will occur. The total scattering angle can be approximated to follow a Gaussian distribution and is described by Equation 2.8 [42] and depicted in Figure 2.4

$$\theta_0 = \frac{13.6}{\beta c p} z \sqrt{\frac{x}{X_0}} [1 + 0.038 \ln(x/X_0)] \quad (2.8)$$

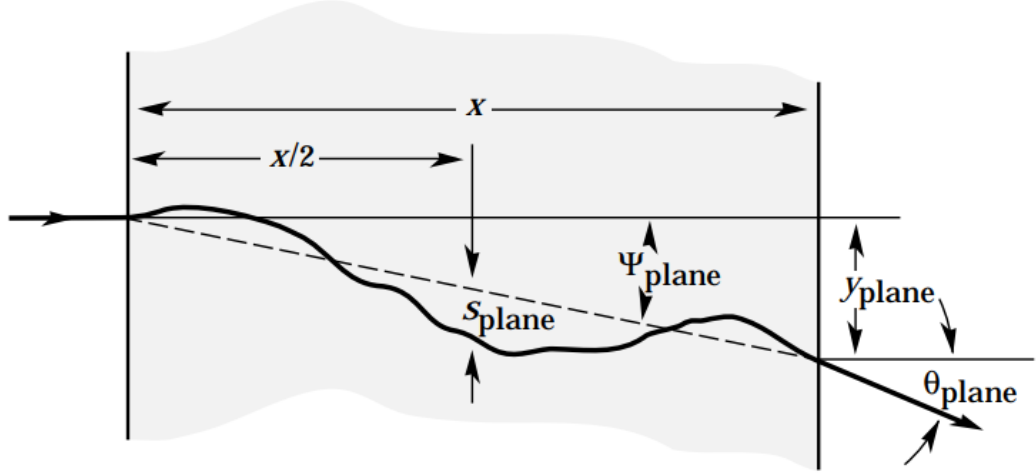


Figure 2.4: Taken from [42]. Quantities used to describe multiple Coulomb scattering. The particle is incident in the plane of the figure

where $\theta_0 = \frac{\theta}{\sqrt{2}}$ the projection of the angle on a plane, βc is the velocity m/s , p is the momentum in MeV/c , the charge of the incident particle is z , x is the thickness of the material and X_0 is the radiation length measured in g/cm^2 . The radiation length is characteristic of a material and describes the mean free path length for a radiation type when its energy has been reduced by $1/e$. The radiation length for a given material can be calculated using Equation 2.9 [42]

$$X_0 = \frac{716.4A}{Z(Z+1)\ln(287/\sqrt{Z})} \quad (2.9)$$

where Z is the atomic number of the medium and A is the atomic mass of the medium.

2.3.4 Electron interactions with matter

It has been identified that electrons are the cause of ionisation for photons and are produced from heavier charged particle ionisation, so they have an important role in radiotherapy.

Electron lose energy through collisional losses with orbital electrons like heavier charged particles which have the same effect; causing excitation and deexcitation within the atom or ejecting an electron directly creating ions.

Electrons are light in comparison to protons, hence they interact differently with

2. RADIATION IN CANCER THERAPY

matter as they will typically interact with other electrons. By substituting the mass of the electron into Equation 2.7 it can be seen that an electron may lose all of its energy in an electronic collision. This also translates into large scattering angles for electrons when considered in Equation 2.8.

Radiative losses also occur for electrons when at relativistic energies, known as Bremsstrahlung radiation. Bremsstrahlung radiation or braking radiation is the emission of a photon to conserve energy, when an electron is deflected and slowed down by a positively charged nucleus. The produced photons will then undergo the interactions discussed in 2.2.1 to deposit energy in the material.

2.3.5 Current status of proton therapy

The concept of using protons therapeutically is more than 70 years old [13], the first specific clinical implementation came 30 years ago, where before this accelerators designed for the purpose of nuclear experiments were used to treat with protons. Although proton therapy physically demonstrates advantages in conformality and the sparing of healthy tissue [35], the delivery of proton therapy is more difficult; facilities are limited because of their cost, size and lack of medical validation.

A medical linear accelerator (linac) is used to generate the x-rays used for conventional radiotherapy. To generate the x-rays, electrons are thermionically emitted and accelerated and focused on to a tungsten target. The energy of photons needed for treatment is typically between 5 and 10 MeV, and hence represent the typical voltages required to accelerate the electrons to the x-rays needed. Electrons are also $\sim 1/1800$ the mass of a proton, making the magnet field required to bend the electrons much weaker in comparison to protons. For Protons to reach 30cm depth in tissue, 225 MeV is needed, requiring bigger accelerators. Protons are heavier than electrons, and hence have a larger beam rigidity, which is a quantity that describes the difficulty in bending the beam at a given moment. A larger beam rigidity would require larger bending fields, a larger bending radius or a combination of both field and radius. The beam rigidity and total energy required to reach 30cm depth in water are highlighted in Figure 2.5 for all fully stripped ions up to carbon. Each colour in Figure 2.5 refers to a different ion, and for a given particle energy the magnet strength in Tesla per metre needed to bend the beam 90 degrees is plotted. For heavier ions it can be seen that high magnet strengths are needed to bend the beam, so to counteract this the bending radius is increased. Increasing the magnet length allows for weaker magnets, but at the compromise of space.

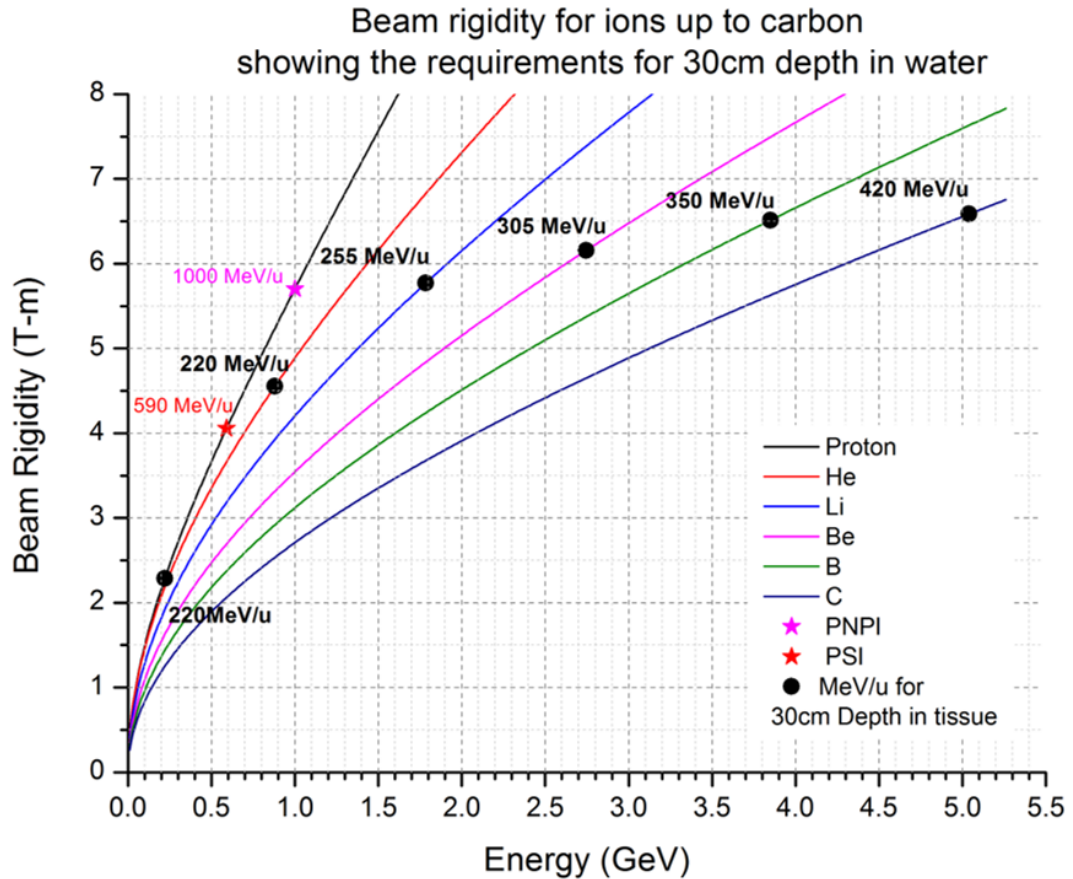


Figure 2.5: The bending radius necessary to bend the beam against kinetic energy for fully stripped ions up to carbon. The energy necessary to reach 30cm depth in water was calculated using SRIM [43]

Because of the much larger energies and magnets required, larger facilities are required, which has been a limiting factor in installing proton therapy in current medical facilities. Typically, it requires new infrastructure which is costly. Where implemented, circular accelerators are typically used to accelerate the particles. This is because using a linac would require a much larger facility. With the advancement in accelerator technology, single room solutions are now available for proton therapy, improving the accessibility of the technique.

2. RADIATION IN CANCER THERAPY

2.3.5.1 Current proton therapy solutions

The cyclotron is the most common accelerator used for proton therapy and can be bought off the shelf. Cyclotrons are reliable machines that use large fixed field magnets to create high current continuous beams and can be operated simply.

The recent trend has been to reduce the size of proton facilities, for example, Varian offer a single room solution with a 360° gantry treatment room that will fit in a tennis court [44]. With a current conventional facility, the size of 50m², the Varian machine is 4 times as large [45] [46]. MEVION however offer a single room solution that fits into an existing vault using a superconducting mounted synchrocyclotron on the gantry; note the gantry can only rotate 190° around the patient [47].

Synchrotrons are also used for proton therapy but are less common. Synchrotrons are pulsed beam accelerators where the orbit of the accelerator remains constant. Acceleration occurs by varying the magnetic field and RF frequency with time to keep the particles on orbit. Unlike cyclotrons, synchrotrons allow for variable energy extraction, and can reach higher energies. A consequence to this is that acceleration is not rapid, and changing energy takes time. They are generally larger than cyclotrons, as they require pre-acceleration. Hitachi sell an off the shelf synchrotron for proton beam therapy, which has a diameter of roughly 7m. This is comparable to the medical cyclotrons; however this does not include pre injection.

Further medical validation needs to be demonstrated by clinical work and studies. Aside from the many discussions about the RBE and LET of particle therapy [48] [49], there are an insignificant number of cases of proton therapy relative to conventional radiotherapy. To put this into context, by the end of 2016 approximately 150,000 patients have been treated with protons [17]. In 2015-2016 in the UK alone 134,000 patients were treated with radiotherapy [24]. In the 30 years since they were first used in hospitals, there are now 70 operational proton facilities, which are exponentially growing in number. The increased number in facilities now allows the necessary randomised trials to justify clinical treatment selection and provide quality clinical based evidence [50] [51] [52].

2.4 Ion therapy

Having discussed the benefits of protons over conventional radiotherapy, it is becoming increasingly popular as a solution to achieve more conformal dose. The development of using charged particles like protons, has naturally led to the development of using

heavier ions for therapeutic use. Currently ion therapy solely relates to carbon ions, which is the only ion being used therapeutically for radiotherapy. The physical benefits achieved by protons are amplified as the mass of the primary ion increases. Comparing carbon ions to protons the rms scattering angle, the standard deviation of the lateral spread and longitudinal straggling are reduced by roughly by 75%; delivering a sharper narrower Bragg peak [53] [54]. Carbon ions have a high LET, and an RBE two to 3 times that of photons [23], making them significantly more effective at killing cells compared to photons and protons. Carbon ions have also proven beneficial to tumours that have shown resistance to low LET radiation [29].

2.4.1 Carbon ion facilities

There are currently 11 ion therapy centres worldwide, 7 centres are in Asia while the rest are in Europe. Compared to the number of operational proton therapy sites, there are 6 proton therapy sites for every carbon ion therapy facility. [21]. In addition to this, there are 5 carbon ion treatment facilities under construction [55]. Irrespective of the biological rationale, the infrastructure necessary to build a carbon facility restrict its location typically to new build hospitals, which can be indicated by the ratio of carbon to proton facilities. All of these carbon facilities are dedicated synchtrons and are capable of accelerating all ions up to carbon with the same accelerator. There are currently no off the shelf commercial solutions available for carbon ion therapy, however Toshiba are prepared to offer a custom turnkey solution [56].

Out of the European centres, two facilities are in Germany, Heidelberger Ionenstrahl-Therapiezentrum (HIT) in Heidelberg and Marburger Ionenstrahl-Therapiezentrum (MIT) in Marburg, provide carbon ions up to 430 MeV/u with an approximate circumference of 65m [57] [58]. The 3rd facility, Centro Nazionale di Adroterapia Oncologica (CNAO) in Italy, accelerates carbon ions to 400 MeV/u with an approximate circumference of 78m [59]. The final facility in Europe is MedAustron in Austria is based on the CNAO model [60]. A gantry for ion therapy will require a footprint similar to that of the accelerator. There are only two gantries present in the world for ion therapy; a normal conducting gantry at the Heidelberg facility and a superconducting gantry at HIMAC (Heavy Ion Medical Accelerator in Chiba), one of the facilities in Japan. The Heidelberg gantry is depicted in Figure 2.6, it uses normal conducting magnets and is approximately 600 tonnes, 25m in length and 13m in diameter [61]. The HIMAC gantry uses some superconducting magnets and is 300 tonnes, 13m long and has a diameter of 11m [62]. The benefits of a having a gantry for treatment are

2. RADIATION IN CANCER THERAPY

obvious, however for ion therapy the footprint is as large as the accelerator significantly increasing the financial and infrastructure cost. For the facilities that do not have a gantry, static beam lines are successfully used at different angles. This is sufficient, however this is at the expense of treatment time due to patient positioning



Figure 2.6: The Heidelberg Ion-beam Therapy Center rotating gantry [63]

2.4.1.1 Fragmentation

When a particle collides with tissue it may undergo an inelastic nuclear interaction. For heavier ions this interaction may result in the ion breaking up into smaller daughter fragments in a process known as fragmentation. The smaller fragments are lower z secondaries relative to the incident particle and are produced with a similar velocity to

that of the primary. The daughter fragments contribute to the total energy deposition along the path of the primary, and because of their reduced mass have an increased range, and will have an increased scattering angle. The target nucleus may itself also break up, but this will be at a low energy and will not travel with the other secondary particles. As discussed above, when the particle slows down, the ionisation density increases due to the number of collisions. For heavier ions this increases the number of nuclear interactions and hence the production of low z secondaries. The produced secondaries in the Bragg peak then have the potential to travel beyond the Bragg peak and create a dose tail. The dose tail is an unwanted side effect of heavier ion therapy, and is counter intuitive to the initial concept of charged particle therapy being more conformal and avoiding dose deposition proximal to the desired location; where radio sensitive structures may be located. The amount of fragmentation from an ion increases with mass, as depicted in Figure 2.7 [64] [52] [65]

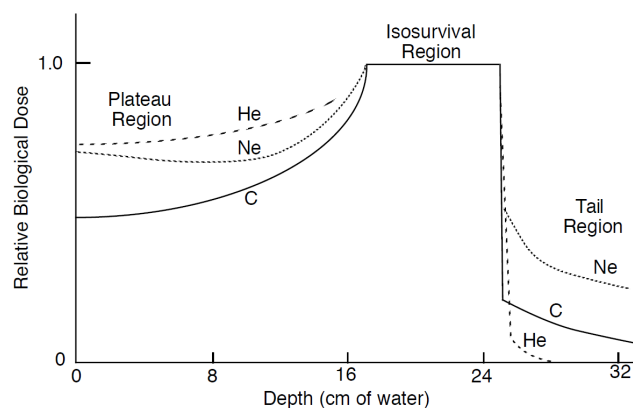


Figure 2.7: A depiction of the relative dose as a function of depth for different ions. As the mass of the ion increases, the fragmentation dose tail increases distally to the tumour [64]

2.4.2 Alternative ions

The advantages of carbon ion therapy over proton therapy are evident, however the produced dose tail is undesirable, and size and cost of the facility restricts the implementation of carbon ion therapy in currently established facilities and hospitals [54]. If the HIT synchrotron is taken as an example, a 65m circumference translates to 336m² just for the accelerator, which is roughly 6.5 current radiotherapy bunkers worth of space. A compromise to increase the availability of ion therapy could be to use an

2. RADIATION IN CANCER THERAPY

ion lighter than carbon yet heavier than protons. Such light ions consist of helium, lithium, beryllium and boron. The size of the facility can be reduced by using light ions for therapy, as reducing the mass reduces the beam rigidity (Figure 2.5) and allows for a smaller accelerator and hence reduced cost. Despite the benefits of carbon ion therapy over proton therapy the cost and size of proton facilities are more reasonable, demonstrated by recent installations in established hospitals

2.5 Helium ion therapy

Helium ions have been used as a therapeutic tool in the past. LBNL treated more than 2000 patients with helium ions between 1977 and 1992 [66] [67]. Patients were treated with an array of different dose schemes making it difficult to compare results and analyse further [68], yet the work completed showed clinical benefits [69]. There is a rising clinical interest in reviving the use of helium ion for therapy and a revival is not unrealistic. Currently, the only facilities that can accelerate helium ions to relevant therapeutic depths are carbon facilities, and research is currently ongoing to use helium ions as a treatment modality in addition to carbon ions [70] [71].

Helium is the easiest light ion to accelerate after protons, and in terms of rigidity is a compromise between carbon and protons. Having a mass four times greater than that of protons, the rms scattering angle, the standard deviation of the lateral spread and longitudinal straggling are roughly halved [53]. This is comparatively worse than carbon, however the dose tail generated by low z secondaries is considerably less. Having both physical advantages over carbon and protons, helium has the potential to be the compromise to allow ion therapy to become more available.

2.6 Chapter summary

In this chapter the effect ionising radiation has on tissue was examined. The way different radiation types interact with matter has been discussed, explaining the evolutionary physical rationale for using charged particles for radiotherapy to improve conformity from conventional radiotherapy. The increased mass of carbon ions used for ion therapy delivers a more conformal dose, but the cost and size of the facility limit the availability. Different potential ions that could be used instead of carbon were suggested, based on their potential clinical benefit and reduced size and cost. Helium ions were highlighted as the ion with the most potential to be used therapeutically. Research has started in preparation to treat patients with helium ions at current carbon ion facilities.

3

Accelerator theoretical background

In this chapter the theory of particle acceleration will be discussed, covering the different types of accelerators used medically. The medical requirements for a therapeutic beam will be identified and how each accelerator type meets these demands.

3.1 Electrostatic acceleration

DC or electrostatic acceleration accelerates particles across a constant potential difference. The energy gained by a charged particle with charge q will gain kinetic energy KE as shown in Equation 3.1

$$KE = q\Delta V \tag{3.1}$$

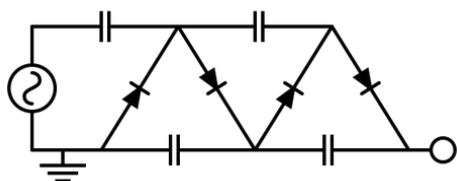
where ΔV is the potential difference across the accelerating gap. Naturally from Equation 3.1 the larger the potential difference, the greater the kinetic energy transferred to the particle. There are two well established electrostatic accelerator designs that achieve high voltages used for accelerating particles; the Cockcroft Walton generator and the Van de Graff accelerator.

3.1.1 Cockcroft Walton generator

The Cockcroft Walton generator was designed by John Cockcroft and Ernest Walton in 1932, where they accelerated protons to 700 keV [9]. The accelerator design uses a low AC voltage to produce a larger DC voltage, allowing the creation of a high potential

3. ACCELERATOR THEORETICAL BACKGROUND

difference to accelerate particles. The generation of the high voltage is created by a voltage multiplier or, Greinacher multiplier, named after the inventor of the circuit with the same name; Heinrich Greinacher [72]. The circuit consists of an arrangement of diodes and capacitors, as depicted in Figure 3.1a. As the current flows through the circuit, the first diode allows current to pass charging the first capacitor, whilst the second capacitor is not charged because the second diode does not allow current to pass and complete the circuit. Once the polarity switches on the voltage, the current flows in the opposite direction, the first capacitor cannot now be charged as diode one prevents the flow of current, charging capacitor 2 instead, with the additional charge of capacitor 1; twice that of the original AC voltage. Combining many circuits allows the voltage to be continually doubled up to a peak voltage in air before breakdown begins to occur [73].



(a) A depiction of the standard voltage multiplier diagram



(b) John Cockcroft and Ernest Walton working on their self titled generator [74]

Figure 3.1: The Cockcroft Walton generator

3.1.2 Van de Graaff accelerator

A Van de Graaff accelerator or generator utilizes a dielectric material on a belt on a pulley to create a high voltage potential. The generator uses the triboelectric force to purposely charge the rollers, turning the belt, generating electric fields. The generated electric field ionises the air and charges the spherical surface at the top of the generator. Invented by the physicist of the same name in 1933 [75], a Van de Graaff generator is depicted in Figure 3.2a.

A motor controls the rollers at the top and bottom of the dielectric belt, causing the belt to turn continuously. At the bottom and top of the belt there are two metallic

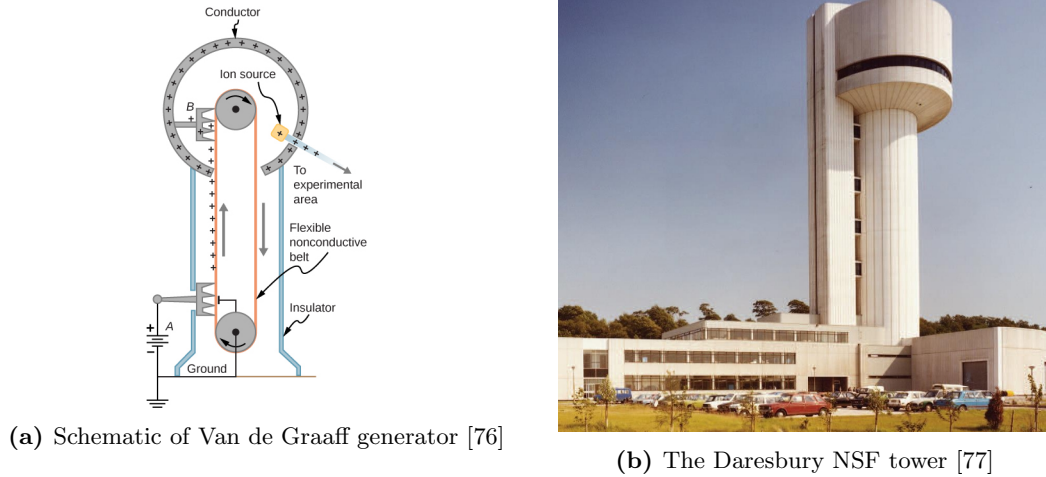


Figure 3.2: The Van de Graaff Generator

combs positioned very close to the belt, where the top comb is connected to a large metallic sphere surrounding the structure. The motion of the belt against the lower roller stimulates the triboelectric force generating a positive charge on the belt, and a negative charge on the roller. The negative charge on the roller then repels the electrons present in the lower comb, making the comb positively charged, and generating an electric field between them. Air molecules interact with the electric field, electrons get attracted to the positive comb, leaving positive ions behind which get attracted to the negative roller. The air ions do not reach the roller, as the dielectric material is in the way, and the charges get carried by the belt. Once they reach the top of the generator, the positively charged belt attracts electrons from the roller, making the top roller positively charged. This in turn creates an electric field between itself and the comb like the bottom roller, however it is the positive charge that gets repelled and pushed out onto the connected outer spherical structure. The electric field generated as below interacts with the air, and the positive ions continually charge the outer dome. The limitation of the generator is determined by when corona breakdown occurs at the sphere surface.

3.1.3 Tandem accelerator

Tandem acceleration utilised the charge of the particles accelerated in combination with the Van de Graff generator. By changing the charge on the accelerated particle, the repulsion and attraction of the charge can be taken advantage of to accelerate the particle twice. The alternation of charge is usually undertaken by passing the

3. ACCELERATOR THEORETICAL BACKGROUND

charged particles typically through argon or nitrogen gas or a carbon foil. Typically, a negative ion will be accelerated towards the generator, stripped of its electrons, and then repulsed away to double its energy.

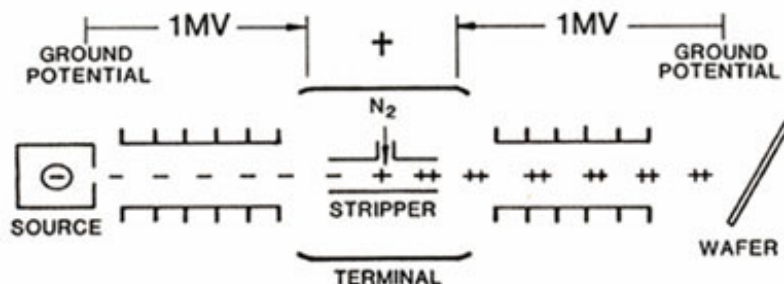


Figure 3.3: An example tandem accelerator [78]

3.1.4 Limitations of electrostatic acceleration

As briefly mentioned both the Cockcroft Walton generator and Van de Graaff accelerator are both limited by corona breakdown, where air surrounding the electrode breaks down and discharges the electrode and arcs are generated. This limits the maximum voltage that can be generated which is approximately 1.5 MV in air. Highly charged surfaces also have limitations due to the amount of charge that can be stored in a material. To maximise the potential on the surface of the material its composition and finish are extremely important, which is why the Van de Graaf generator is a sphere; as charge will collect at sharp points [73]. Increasing the size of the sphere allows the collection of more charge on the surface. Changing the pressure of the environment where the generator is used can improve and increase the voltages achievable. Combining these properties have generated potential differences up to 40 MV [79] [80].

3.2 RF acceleration

The development to achieve greater particle energies beyond electrostatic acceleration came from radio frequency acceleration, where an electric field is coupled to a sinusoidal RF source. Each half wavelength, the polarity of the voltage changes, and Wideroe developed an accelerator which increases the energy at each crossing of the field. Known as a linear accelerator (or linac), the design shielded particles from the electric field

inside electrodes exposing the particle to the electric field in the gaps between. The voltage experienced by the particle when traversing the gap is shown in Equation 3.2

$$V = V_0 \cos(\phi) \quad (3.2)$$

Where V is the voltage experienced by the particle, V_0 is the peak voltage and ϕ is the RF phase. The energy by the particle is dependent on its charge and the voltage experienced when crossing the gap, is shown in Equation 3.3

$$E = qV \quad (3.3)$$

Where E is the energy gained by the particle, q is the charge of the particle, and everything else is as previously described.

When accelerated, the particle gains energy and travels faster. If the electrodes were equidistant, as the particle energy increases, it would arrive before the voltage has switched polarity; out of phase. To counteract the time difference, Wideroe increased the length of the electrodes so the particle arrived at the centre of the gap at exactly each half wavelength. The development of the linac allowed acceleration to high energies using small voltages, as long as the drift lengths remained half a wavelength apart. This however becomes a disadvantage as the space needed to accelerate for a given energy scales by a factor of 2 each time. Another disadvantage with linacs is that each RF section can only be used once, so the design is somewhat inefficient.

3.3 Classic cyclotron

The classical cyclotron was designed by Ernest Lawrence in 1932 and accelerated protons to 80 keV, Figure 3.4 [14] [81]. The concept of the cyclotron uses RF acceleration with an RF frequency that matches that of the machine known as the cyclotron or fundamental frequency. By placing two accelerating gaps 180° apart from one another, as the particle reaches the centre of the gap, the polarity of the voltage is switched accelerating the particle across each gap. Particles are accelerated in the centre of two semi-circle electrodes, identified as dees because of their shape resembling the letter D. Above and below the dees are the two magnetic field poles, which create the uniform magnetic field in the centre of the electrodes. When a charged particle moves through a magnetic field, it experiences a force,

$$\vec{F} = q(\vec{E} + \vec{v} \times \vec{B}) \quad (3.4)$$

3. ACCELERATOR THEORETICAL BACKGROUND

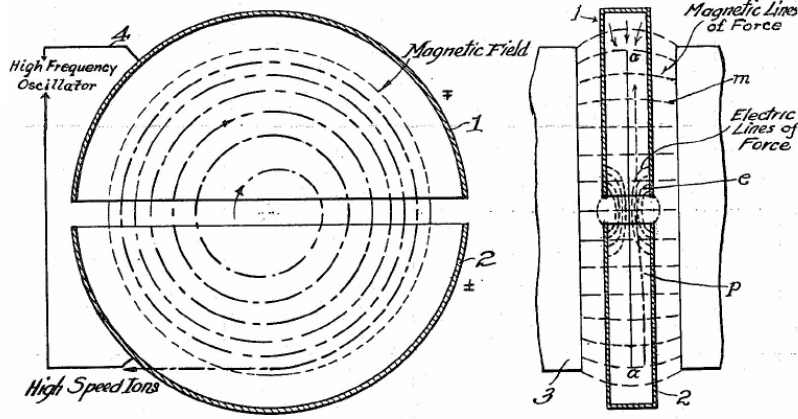


Figure 3.4: Earnest Lawrence's cyclotron in 1932 [14]

where F is the force in Newtons, q is the charge of the particle, \bar{B} is the magnetic field in tesla and \bar{v} is the velocity of the particle. This shows that for a charged particle moving through a magnetic field will experience a force orthogonal to the magnetic field and velocity, hence placing a particle with mass m and charge q in a uniform magnetic field the particle will follow a circular path. Similarly, the force of particle traversing a circular path experiences a centrifugal force which is identified in Equation 3.5

$$F = \frac{mv^2}{r} = qvB \quad (3.5)$$

Where r is the particle radius and v is the magnitude of the velocity. Rearranging Equation 3.5 describes the particle motion by the radial distance and the strength of the magnetic field, known as the beam rigidity:

$$Br = \frac{mv}{q} = \frac{p}{q} \quad (3.6)$$

where p is the momentum of the particle. This gives a measure of how difficult it is to bend a beam at a given moment.

In a circular motion one can also describe the revolution frequency or Lamor frequency shown by Equation 3.7.

$$\omega = \frac{v}{r} \quad (3.7)$$

Equation 3.7 can be combined with Equation 3.5 showing that the revolution

3.3 Classic cyclotron

frequency for a particle in a uniform magnetic field is completely dependent on the charge to mass ratio. Equation 3.8 is a fundamental property relevant for all circular accelerating machines, however this is only correct for non-relativistic particles, where relativistic considerations to these equations will be addressed later in this chapter.

$$\omega = \frac{qB}{m} \quad (3.8)$$

There is also a relationship for the kinetic energy of the particle from its radius and the magnetic field, as shown in Equation 3.9 by combining equations 3.5 and 3.7

$$KE = \frac{mv^2}{2} = \frac{mq^2B^2r^2}{2m^2} = \frac{m\omega^2r^2}{2} \quad (3.9)$$

3.3.1 Weak focusing

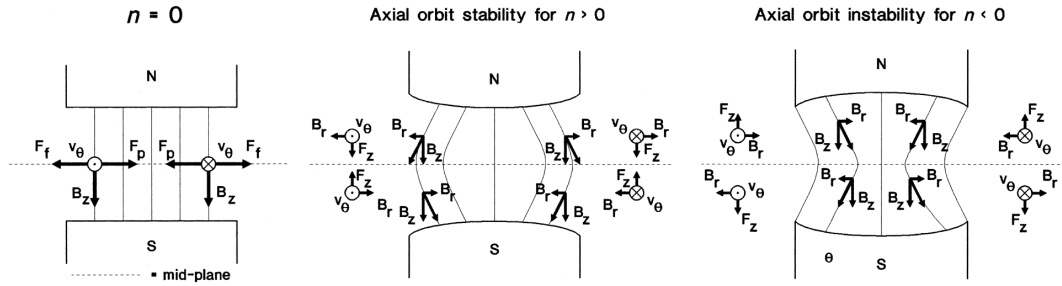


Figure 3.5: A figure taken depicting the concept of weak focusing for different field index, n K. Strijckmans(2001)

Theoretically the particle will travel around the cyclotron exactly on the midplane of the desired magnetic field. However, small imperfections or misalignment errors will cause deviations in both the horizontal and vertical directions. Without restoring forces to keep the particle on the equilibrium orbit, collisional losses with the electrodes will occur. These restoring forces come from a radial variation of the magnetic field, by adjusting the opening of the magnets, known as the field index, described in Equation 3.10

$$n = -\frac{dB}{B} \bigg/ \frac{dr}{r} \quad (3.10)$$

With no magnetic field gradient, the field index is equal to 0, and in the perfect cyclotron, particles will not collide with the boundaries of the accelerator providing

3. ACCELERATOR THEORETICAL BACKGROUND

they remain on the equilibrium orbit; as described in Figure 3.5.

If the field index is greater than 0, the magnetic field weakens as a function of radius, and the poles are bent outwards. This changes the field lines of the magnet, and restoring forces are introduced towards the midplane of the accelerator, correcting any axial particle movement in the accelerator. Alternatively, if the field index is less than 0, the axial forces move the particle away from the equilibrium orbit of the accelerator achieving the opposite desired effect. From this it is therefore necessary to have a field index greater than 0.

As the energy of the particle increases it will start to approach speeds comparable to the speed of light, and relativistic effects will need to be considered. As a particle becomes relativistic its mass increases by a factor of gamma, known as the Lorentz factor; Equation 3.11

$$m = \gamma m_0, \quad \text{where } \gamma = \frac{1}{\sqrt{1 - \beta^2}} = \frac{1}{\sqrt{1 - \frac{v^2}{c^2}}} \quad (3.11)$$

where c is the speed of light, v is the particle velocity and β is the ratio of the particle speed to the speed of light.

Reducing the magnetic field keeps the orbit central axially, but radially the outcome is different. The magnetic field needs to be increased radially to keep the particle isochronous because of special relativity, hence negative field index is required. As the field index exceeds 1, radial stability will not be achievable. To achieve restoring forces in both planes it has been deduced that the field index n needs to be between 1 and 0 for a classic cyclotron.

Eventually special relativity will increase the mass of the particle and reduce the orbit time, making the particle lose synchronicity with the phase of the RF system, and eventually become nonsynchronous. The effects of relativity limit the classical cyclotron as the magnetic field and the voltage RF frequency are constant, changing either the frequency, the magnetic field or both must be used to counteract the relativistic effects and keep the particle isochronous.

3.4 Isochronous or AVF cyclotrons

To isochronously accelerate particles into the relativistic regime, a radially varying field needs to be introduced, $B(r)$. The additional magnetic field strength needs to match the increase in particle mass introduced by relativity necessary to maintain synchronism; as described by Equation 3.12. The additional magnetic field is achieved by multiplying

3.4 Isochronous or AVF cyclotrons

the magnetic field at $r = 0$, B_0 with the gamma factor γ , as described in Equation 3.11

$$B(r) = \gamma B_0(r) \quad (3.12)$$

As discussed in 3.3, this corresponds to a field index requirement to less than 0, which is beyond the constraints for vertical focusing. Isochronous cyclotrons, also identified as Thomas cyclotrons or azimuthally varying field (AVF) cyclotrons, introduce the extra axial forces necessary by creating alternating azimuthal variations in the magnetic field. The alternating magnetic field strength is achieved by shaping the magnetic poles and the different regions are referred to as hills and valleys; A hill describing a stronger magnetic field, and a valley a weaker magnetic field as described in Figure 3.6.

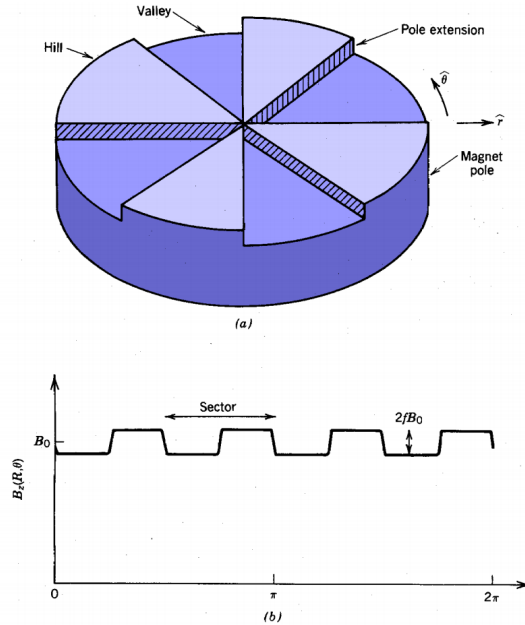


Figure 3.6: a) shows the visible hills and valleys in an isochronous cyclotron, and b) shows the magnetic field amplitude as a function of azimuthal angle [82]

The introduction of hills and valleys changes the trajectory of the particle, and is no longer circular. The trajectory of the particle becomes scalloped because of the reduced bending in the valley sections. The resultant orbit is no longer circular, and the shape represents the number of sectors in the machine, where a sector consists of a hill and a valley. The repetition of hills and valleys introduce Thomas focusing. Thomas focusing

3. ACCELERATOR THEORETICAL BACKGROUND

is described by the flutter, F , the quantification of the variation of the magnetic field between the hills and valleys.

$$F = \frac{\langle B_{hill} \rangle - \langle B_{valley} \rangle}{\langle B_0 \rangle} \quad (3.13)$$

Where B_{hill} is the magnitude of the magnetic field in the hill, and B_{valley} is the magnitude of the magnetic field in the valley. In order to maximise the field variation, the valley segments of the AVF cyclotron were reduced as much as possible before being removed completely, introducing separate sector cyclotrons.

3.5 Betatron motion and tunes

As previously discussed, the ideal particle will travel exactly around the midplane in the radial and vertical position; known as the stable equilibrium orbit. Realistic motion however dictates that the particle will oscillate around the stable equilibrium orbit, caused by the restoring forces in each plane.

The first accelerator to introduce restoring forces conceptually was the betatron, hence the oscillations around the stable equilibrium orbit are known as betatron oscillations, and the movement of the particle is known as the betatron motion. The betatron was developed by Max Steenbeck, but not built until 1940 by Donald Kerst [83]. Electrons are limited in a cyclotron because of relativity, so alternative methods were explored for high energy electron beams and x-ray generation. A betatron consists of a vacuum torus encased by an electromagnetic field. Like a cyclotron, the radial orbit is maintained by the magnetic field, and the electrons are accelerated by an external electric field. The electric field in a betatron is generated by induction, like a transformer, except in this case the electrons in the vacuum torus act as the secondary coil. As the electrons gain energy the magnetic field is increased to maintain the same orbit, and weak focusing introduced to restore particle deviation from the midplane. The number of particle oscillations per single turn is called the tune, Q [82]

The radial tune in a classic cyclotron is shown in Equation 3.14 [82], and the vertical tune in Equation 3.15 [82].

$$Q_r = \frac{\omega_r}{\omega_0} = \sqrt{1 - n} \quad (3.14)$$

$$Q_z = \frac{\omega_z}{\omega_0} = \sqrt{n} \quad (3.15)$$

where Q_r is the radial tune, ω_0 is the stable equilibrium orbit frequency, ω_r is the radial betatron oscillation frequency, n is the previously identified field index, Q_z is the vertical tune and ω_z is the vertical betatron oscillation frequency. With the additional focusing for the isochronous cyclotron, necessary to satisfy the field index constraints, the vertical tune gains an additional term.

$$Q_r = \frac{\omega_r}{\omega_0} = \sqrt{n + F} \quad (3.16)$$

3.5.1 Resonances

Resonances in betatron oscillations can occur when a coupling between the vertical and horizontal becomes apparent, identified by Equation 3.17

$$l = mQ_r + nQ_z \quad (3.17)$$

Where l , m and n are integer values. The order of the resonance is identified by the sum of $|m| + |n|$. Equation 3.17 can be interpreted visually by what is known as a tune map, and the resonances are represented by lines. The particles tune can also be represented on a tune map for a given energy, which is known as its working point. The working point can be plotted for different energies across the accelerating regime, which may vary with energy. If the working point moves across the accelerating regime, it can potentially cross resonance lines on the tune map, which may amplify particle oscillations and cause beam losses. Resonance crossings are more destructive at lower orders, typically 1st and 2nd, and are avoided when designing an accelerator. Higher order resonances are less destructive and crossing them can be tolerated, however crossings should be completed quickly and ideally perpendicular to the coupling to minimise beam deterioration, as this is the quickest way to cross a line. The way a particle moves on a tune map can be manipulated when designing an accelerator by changing its magnetic field profile.

3.6 Synchrocyclotron

The alternative to changing the magnetic field to counteract the relativistic mass increase is to decrease the operational RF frequency of the cyclotron during acceleration. This has both advantages and disadvantages in comparison to isochronous and classic cyclotrons. Because the frequency is changing, only one particle bunch can be accelerated at any given time, and the beam is not continuous. The RF system can use

3. ACCELERATOR THEORETICAL BACKGROUND

one dee, smaller voltages and the accelerating gaps can be much smaller, and higher energies can be achieved at the cost of many more turns in the accelerator [82]. Consequently, the beam current is much lower, and as other accelerators were developed and could achieve these energies with higher currents, the synchrocyclotron became less popular.

3.7 Synchrotron

The synchrotron was developed from the issues encountered with relativity in the cyclotron. Where in a cyclotron the variation in magnetic field is completed as a function of radius, spatially, the synchrotron changes the magnetic field as a function of time. The RF used is also time varying like the synchrocyclotron, hence the same orbit can be used to accelerate particles. Discovered by Vladamir Veksler in 1945 [84], at the time this was significant development, as magnet and vacuum size could be decreased making the accelerator more cost effective. The synchrotron introduced strong focusing, which uses magnetic deflection with quadrupoles in order to focus the beam. It is only possible to focus the beam in one plane at a time, which defocuses the beam in the other plane. The effect can be reversed by using another quadrupole that is rotated 90° and the focusing and defocusing planes are switched. It was however discovered by having a calculated drift between the two quadrupoles an overall focusing effect is achieved. This layout is depicted in Figure 3.7 known as a FODO arrangement - focusing drift defocusing drift. In Figure 3.7 the beam path is shown in red, the beam envelope is shown in blue and the focussing /defocussing magnets in black identified by QF and QD respectively.

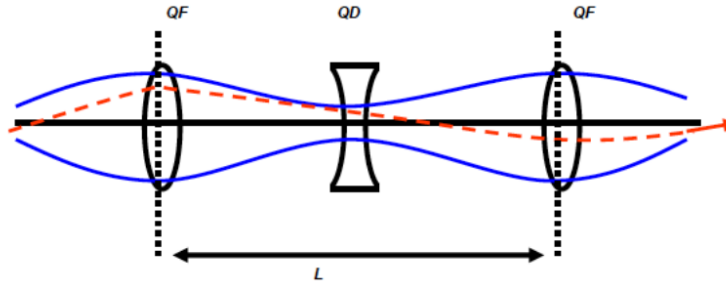


Figure 3.7: A depiction of the FODO lattice [85]

3.8 Accelerators used for particle therapy

As discussed in Chapter 2 cyclotrons are the work horses of proton therapy where approximately $\frac{2}{3}$ of proton beams are delivered by a cyclotron [21]. Because they are fixed field magnets, cyclotrons can be simply operated, making them easier to use in a facility. However, cyclotrons are limited in that they extract at a single energy, meaning to change energy the beam needs to be degraded. The consequence of beam degradation for particles are the low secondaries produced, and the increased shielding necessary because of it. Both Isochronous and synchrocyclotron exist as a method of delivering proton beam therapy. Isochronous cyclotrons have both fixed field and fixed frequency RF, making the operation much simpler, and a CW beam is delivered. Consequently, one has to worry about orbit separation at higher energies, as discussed earlier in this chapter. Synchrocyclotrons are more compact, but the change in RF Frequency generates pulsed acceleration and treatment times become longer. Pulsed acceleration does hold benefits over CW acceleration as extraction is easier and orbit separation is less of a concern.

Synchrotrons are used for particle therapy and overcome the need for degradation as they allow variable energy extraction. Consequently, like synchrocyclotrons they deliver pulsed beams, and longer treatment times limited by the time dependent magnetic field. The footprint for proton synchrotrons are also currently larger than cyclotrons, because normal conducting magnets must be used, as it is difficult to vary the magnetic field in superconducting magnets. With treatment time being longer, and the footprint being larger, cyclotrons are generally preferred clinically [86].

Currently for ion therapy, only synchrotrons are used. Synchrotrons are used because they can be increased in size to compensate the beam rigidity necessary for heavier particles, using smaller, weaker magnets. In a cyclotron this becomes difficult as the magnetic fields and magnet size required to keep the machine compact are large.

3.9 Fixed Field Alternating Gradient (FFAG) accelerators

A potential solution for ion therapy would be to use a Fixed Field Alternating Gradient (FFAG) accelerator. The FFAG implements the combination of the fixed field time independent magnetic fields from the cyclotron, and the alternating gradient from the synchrotron. This allows fast acceleration of particles associated with cyclotrons combined with the strong focusing and the potential for variable energy extraction from

3. ACCELERATOR THEORETICAL BACKGROUND

the synchrotron. [87]

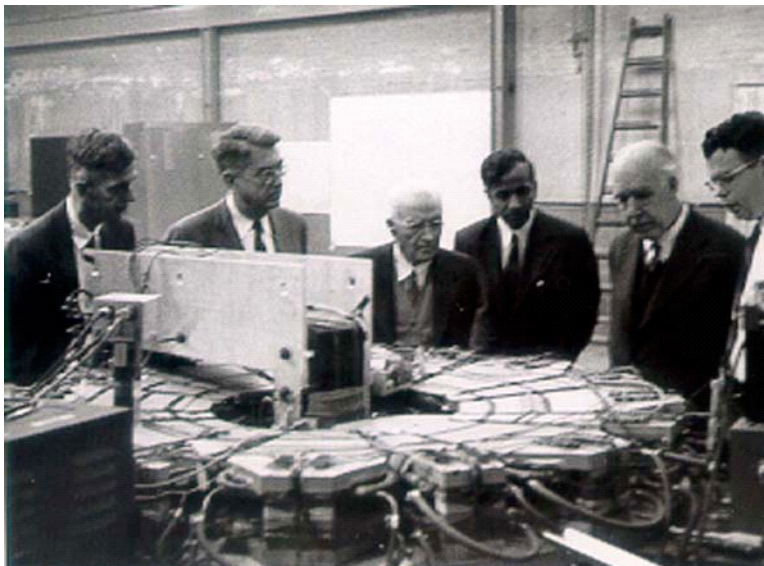


Figure 3.8: The first FFAG at MURA in 1956 [88]

FFAG accelerators were first discovered in the 1950s by Symon [89], Ohkawa [90] and Kolomensky [91] independently of each other. The first operational FFAG followed in 1956; an 8 sector electron FFAG [92]. The concept of the FFAG was developed throughout the 1960s by the Midwestern Universities research Association (MURA). Several electron FFAGs were designed, the first constructed FFAG is depicted in Figure 3.8; a 400 keV electron design. However, the FFAG was quickly overlooked as current research goals were driven towards high energy nuclear experiments, where the synchrotron excelled. In addition to this the complicated 3D field calculation necessary require high computational efforts, which at the time were not possible. The first electron FFAG magnets were completed on a mechanical calculator, the technical limitation at the time [93]. The MURA group ended in 1963, and with this the development and interest of FFAGs remained dormant until recently. With the advancement of technology, FFAG accelerators have been studied for uses in many applications where large particle energies are not necessary. For example, fast acceleration is necessary for muon acceleration due to their short lifetime, and the desire for a neutrino factory inspired people to think of the FFAG again[94]. With this and the computational development over time came a refreshed interest in the FFAG. There are two design types of FFAG, scaling and non-scaling (ns), and the initial focus was on scaling FFAGs.

3.9.1 Scaling FFAG

The scaling FFAG is designed so that as the momentum increases radially the focusing is the same, which means that each successive orbit of increased energy is a geometrical enlargement of the previous. This means that a scaling FFAG has the same orbit shape and optics at all energies but more importantly, the tune is constant for all orbits. To achieve this the radial magnetic field gradient follows the scaling law, identified in Equation 3.18.

$$B_y = B_0 \left(\frac{r}{r_0} \right)^n \quad (3.18)$$

Where B_y is the strength of the magnetic field, B_0 is the magnetic field strength at r_0 , the initial radial start point of the gradient, and r is the radius. The benefit of the scaling FFAG allows the design of a fixed working point of the machine, but consequently, this puts limitations on the size of the machine and acceleration. Obeying the scaling law will dictate the radius of the machine as shown by Equation 3.18. The acceleration is restricted in A scaling FFAG as it can only accelerate one bunch at a time as the scaling law will not satisfy isochronous acceleration, hence variable RF must be used. The use of variable RF will bear the same restrictions as a synchrocyclotron and a synchrotron, limited beam current. However, the scaling FFAG has advantages over its variable RF counterparts by having larger dynamic apertures, allowing larger beam emittances and currents to be accelerated. When being directly compared to the synchrotron the scaling FFAG accelerates particles because of their fixed magnetic fields.

3.9.2 Non-scaling (ns) FFAG

The nsFFAG relaxes the scaling law, which was first proposed by C. Johnstone in 1999 for the acceleration of muons [94]. The nsFFAG still has alternating gradient focusing fixed magnetic fields, but the radial magnetic field gradient does not adhere to the scaling law is completely customisable. The relaxed constraints on the radial magnetic field profile allows greater flexibility with the machine design, but at the sacrifice of a fixed working point. Without obeying the scaling law, the working point will change across the acceleration regime, and the possibility of crossing resonance lines is introduced which can be destructive to the beam. However due to the fast acceleration of the beam in FFAGs, it is possible to minimise the resonant effects on the beam by crossing the resonances quickly. Although one has to manage the working

3. ACCELERATOR THEORETICAL BACKGROUND

point of a nsFFAG during design, its size and magnetic field are no longer bound, and the radial magnetic field gradient can be manipulated to satisfy design requirements for isochronicity, as detailed in Section 3.4. Initial design work focused on achieving isochronicity using a linear magnetic field gradient, where only transverse forces are applied to the beam, i.e systems that only use dipoles and quadrupoles. When obeying the scaling law, the orbit circumference continually increases, however the relationship between the orbit circumference in a linear nsFFAG follows a quadratic relationship when the speed of the particle is approximately the speed of light. The parabolic path length leads to a parabolic time of flight, however the variation of time of flight at the vertex is sufficiently reduced the particles can be accelerated by fixed frequency RF [95].

Using a magnetic field beyond the 2nd order makes a system non-linear, where forces act on the transverse plane. Typically, in non-linear systems 3rd order magnets known as sextupoles are used, which correct for chromaticity, the effective tune spread caused when particles focused by a quadrupole experience different focusing based on their momentum. Using non-linear field components allows the magnetic field to match the time of flight more appropriately to γ . Improving the overall isochronicity of the machine will minimise the phase slip, and make the accelerator more accommodating to magnetic field errors and increasing RF harmonics, which will be discussed later in Chapter 6. If the isochronous condition is matched sufficiently fixed RF can be used to accelerate the beam, and CW acceleration becomes possible. nsFFAGs have the potential to deliver high energy and high current CW beams beyond the capabilities of current isochronous cyclotrons. Higher energy CW beams are desirable for particle therapy, higher currents are desired for more efficient isotope production and high energy, high current beams are well suited for the requirements of accelerator driven sub critical reactors (ADSRs).

3.9.3 Current scaling FFAGs

The first FFAG designs were all electron scaling FFAG type accelerators, but the revival brought the first proton FFAG in 2000, also of scaling design. The first FFAG was constructed in the High Energy Accelerator Research Organisation, KEK (Kō Enerugi Kasokuki Kenkyū Kikō). This design was a proof of principle machine, named POP based on its purpose, and was the first of many FFAGs to be built in Japan. The motivation for POP was rapid acceleration combined with a large acceptance making them suitable for Muon acceleration. POP successfully accelerated protons from 50

3.9 Fixed Field Alternating Gradient (FFAG) accelerators

keV to 500 keV and is a radial 8 sector FFAG, roughly 2m in diameter. POP is depicted in Figure 3.9a [96].



(a) The POP FFAG at KEK, Japan [88]



(b) the 150 MeV proton FFAG at KEK, Japan [97]

Figure 3.9: The first two Japanese FFAG accelerators designed and built in KEK

Due to the successful nature of POP, in 2003 another scaling FFAG was built at KEK, accelerating protons from 12 MeV to 150 MeV. To achieve the 12 MeV injection energy, a nested cyclotron inside the accelerator that feeds the FFAG. This design also uses a triplet configuration but was designed in such a way where a yoke was not necessary. This magnet design allowed more room for injection and extraction. The accelerator is depicted in Figure 3.9b and is roughly 10m in diameter.

3.9.4 Current nsFFAGs

There has only been one nsFFAG built, EMMA (electron machine for many applications) at Daresbury laboratory, UK [98]. EMMA was a proof of principle linear nsFFAG. The lattice was built using 42 straight sections, each containing a defocusing and a focusing quadrupole [99]. each successive quadrupole was slightly offset to provide the bending element, removing the need for dipoles. EMMA successfully accelerated electrons from 10 MeV to 20 MeV and demonstrated the concept of nsFFAG accelerators. EMMA also demonstrated the crossing a first order resonance fast can avoid the destructive betatron resonant growth and allow the beam to survive. EMMA was approximately 5m in diameter in size and is depicted in Figure 3.10.

3.9.5 FFAG designs for charged particle therapy

Currently there are no FFAGs built for ion beam therapy, however there are FFAGs that have been designed for this purpose but never implemented. One of the most com-

3. ACCELERATOR THEORETICAL BACKGROUND

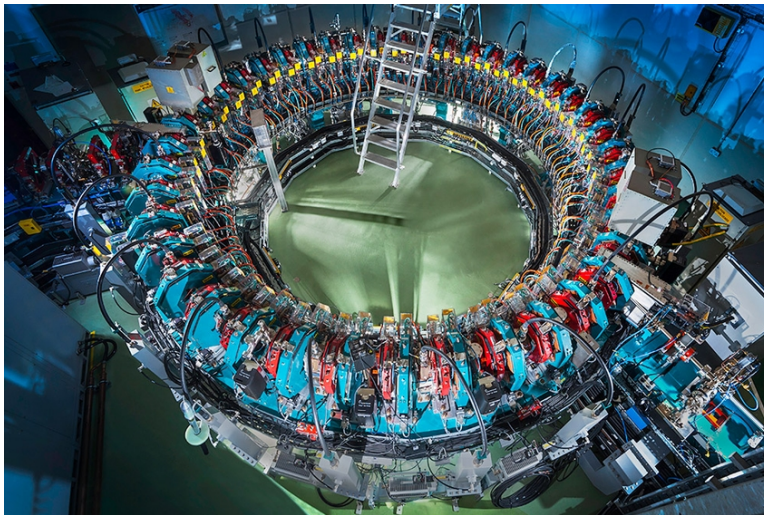


Figure 3.10: An image of the EMMA accelerator [100]

plete designs would be PAMELA, Particle Accelerator for MEDical Applications. The PAMELA design originated from a scaling FFAG, whilst slowly violating the scaling law, and is categorised as a non-linear nsFFAG, as up to decapole field elements are used. The design itself is 2 concentric ring accelerators, with 12 sections each. The inner ring of PAMELA accelerates Protons and for therapy up to 250 MeV/u and carbon ions up to 68 MeV/u. The outer ring further accelerates carbon ions up to 400 MeV/u, the necessary energy to reach 30cm tumour depth. The outer ring of PAMELA had a diameter of 18.4m, taking up approximately 250m² of space, which is approximately a third less space than the current synchrotron models. The design was taken up to engineering level but unfortunately not any further [101].

4

Methods

The work in this thesis is completed using two computational codes. This chapter will briefly discuss the two computational codes used and how they are used in this thesis.

4.1 COSY infinity

The first code used in this thesis is COSY Infinity [102]. COSY infinity is a scientific computing program developed at Michigan State university. COSY infinity combines transfer map with differential algebra to compute high order Taylor maps for a system. For closed repetitive systems this provides very efficient computational power, as only one map needs to be generated for the system which is then extrapolated using Taylor expansion. The efficiency of the code is also clear when comparing to other different types of computational solutions, for e.g ray tracing codes, which track an individual particle in steps around the system until it terminates. This makes COSY a versatile tool when simulating particle accelerators, being able to handle the higher order magnetic field and complex magnet design which in the past has stalled the development of FFAGs.

4.1.1 FACT

In this thesis access to COSY was via a purpose built graphical user interface (GUI) called FACT, developed by Carol Johnstone and Pavel Snopok. This utilities the object orientation of COSY and allows simple construction of multifunction magnets specifically for FFAG design. The capabilities of FACT however are limited, and it is not possible of accelerating particles, so the code is only used for computation of magnetic fields for lattice design.

4. METHODS

The input into FACT contains positional details for each magnet from a coordinate system and its corresponding radial magnitude of magnetic field. The radial magnitude of the magnetic field for each magnet is calculated from equation 4.1

$$f(r) = \sum_{n=0}^5 b_n \times r^n \quad (4.1)$$

$f(r)$ is the the magnitude of the magnetic field for a given radius r , n refers to the order of the magnetic field, and b_n is the magnetic field at $r = 0$ for each input magnet. The magnetic field changes radially, and its radial magnitude is the summation of the different orders of magnetic fields selected to create a custom radial gradient. Each order of magnetic field can be adjusted as a function of radius by choosing its starting value at $r = 0$ for each defined magnet in the design. Because of the hill and valley sections, naturally the field gradient also varies azimuthally.

FACT has the ability to extract a field map from the input design, which can then be used in other computational codes. The output field map is known as the median plane field map, where the magnetic field map is presented in terms of the vertical magnetic field B_z at $z=0$ for given x and y co-ordinates.

The lattice put through FACT then solves the equations of motion for an approximate energy, and is able to find stable equilibrium orbits for a given energy. From the transfer map created from the magnetic field profile the code iterates the radial starting position for a given energy, until it achieves a closed orbit, using the Runge Kutta iteration method. By increasing the particle energy in increments many stable equilibrium orbits can be calculated along the acceleration regime.

From each computed stable equilibrium orbit the path length travelled by the particle is calculated. Knowing the energy and the path length, the ToF can be calculated, and the isochronicity across the acceleration regime assessed.

To calculate the ToF the Lorentz factor γ is calculated for each energy using equation 4.2. The Lorentz factor can be rearranged and interpreted as a velocity using equation (3.11) , hence knowing the velocity and path length the ToF can be calculated.

$$\gamma = E/E_0 \quad (4.2)$$

Where E_0 is the rest Energy of the particle and E is the total energy of the particle.

4.2 OPAL

In order to accelerate particles, RF will need to be introduced, and second code will be required. This also allows the results from COSY to be compared and verified, and OPAL was selected to do this.

OPAL (Object Orientated Parallel Accelerator Library), developed and maintained at the Paul Scherrer Institute (PSI). Based on the MAD language, OPAL was Built from the ground up as a successor to MAD9P and designed to be a fully parallel particle in cell (PIC) code capable of full 3D space charge calculations. Being fully parallel allows OPAL to take advantage of parallel processing, and hence be utilised by high powered computing. There are two flavours of OPAL; OPAL-cycl and OPAL-t. OPAL-cycl focuses on cyclic machines, whereas OPAL-t is designed for the development of beamlines, linacs and x-ray free electron lasers.

OPAL was selected, as opposed to specialist FFAG codes like Zgoubi, as OPAL can read a varied amount field maps from different programs like COSY. A field map cannot be easily inserted into zgoubi and requires a large amount of pre-processing. Only the OPAL-cycl flavour will be used in this thesis, and due to the low currents necessary for particle therapy, space charge effects will be negligible and turned off to speed up computational time. The co-ordinate system in OPAL uses y as the longitudinal direction, x is the radial direction and z is the vertical direction.

The output field map from FACT can be directly fed in OPAL-cycl and converted into a cylindrical co-ordinate system (r, θ, z) within OPAL. In order for OPAL trajectories that extend beyond $z=0$ it requires a magnetic field across the z plane. OPAL achieves this by a 3rd order expansion of the field in the cylindrical co-ordinate system as shown in equation 4.3. As the field is expanded it has limitations as the accuracy of the field declines the further particles become displaced from $z=0$ [103].

$$\begin{pmatrix} z \frac{\delta B_z}{\delta r} - \frac{1}{6} z^3 C_r \\ \frac{z}{r} \frac{\delta B_z}{\delta \theta} - \frac{1}{6} \frac{z^3}{r} C_\theta \\ B_z - \frac{1}{2} z^2 C_z \end{pmatrix} \quad (4.3)$$

Where C_r , C_θ and C_z are the partial differential coefficients. OPAL solves the Lorentz equation 3.4 in the time domain using a collision less vlasov equation. The collision-less vlasov equation is a differential equation that describes the time evolution of the distribution function of a plasma consisting of M charged particles, where E and B are time and space dependent, comprising of internal and external applied fields.

4. METHODS

$$\frac{df}{dt} = \delta f + \sum_{j=1}^M \left[\frac{\delta f}{\delta x_j} \dot{x}_j + q (\mathbf{E} + c\boldsymbol{\beta} \times \mathbf{B})_j \frac{\delta f}{\delta \mathbf{P}_j} \right] \quad (4.4)$$

where $c\boldsymbol{\beta}$ is equivalent to the velocity of the particle. Vector notation is denoted by \mathbf{A} [103].

5

Initial characterisation of beam optics for nsFFAG designs

This chapter covers the design, optimisation and development of the field parameters for a helium non-scaling Fixed Field Alternating Gradient accelerator (nsFFAG). Optimisation will be completed using the two codes of choice, COSY infinity [102] and OPAL [104]. COSY infinity is operated through FACT, a specialised GUI for the COSY infinity code, developed by C. Johnstone and P. Snopok [105]. Initial field parameters provided by C. Johnstone [106] are inserted and optimised using FACT, to produce stable equilibrium orbits for a given particle energy. Once the stable equilibrium orbits are found, the time of flight (ToF) and working point or tune are identified for each orbit across the desired energy range, and the isochronicity profile assessed for suitability for fixed frequency acceleration. Once the ToF and tune results are acceptable, the results are then compared to OPAL.

The importance of fixed frequency RF acceleration has been discussed in Chapter 3, and its consideration is the centre point to the initial design of the machine. This means that the entire acceleration regime needs to be isochronous enough to allow fixed frequency acceleration. Using a fixed field is not an issue in the non-relativistic regime, as the mass of the particle is constant. Once one enters the relativistic regime and begins to approach the speed of light, the particle begins to increase in mass. The increase in particle mass makes it necessary for a bespoke magnetic field gradient to compensate the decrease in frequency, or to change the frequency as the particle accelerates. Ramping the frequency as the particle gains energy complicates the operation of the accelerator, making it more difficult to operate in a clinical environment, and is more expensive to implement.

5. INITIAL CHARACTERISATION OF BEAM OPTICS FOR NSFFAG DESIGNS

5.1 Design parameters

An FFAG accelerator will be designed for the purposes of particle therapy; notably a non-scaling design. A non-scaling design has been selected over a scaling design because of the possibility of achieving isochronous acceleration, and greater compactness, but at the cost of the stable working point, as detailed in Chapter 3. In Chapter 2 it was discussed how essential compactness is when introducing medical accelerators in current clinical environments, and not ignoring the current size of particle therapy facilities and the infrastructure challenges encountered. If the accelerator could fit in a current medical linac bunker, 50m² it would be more than sufficient. A non-scaling design does not come without challenge as the tune stability is sacrificed for the size reduction, and the azimuthal field gradient necessary will be challenging to optimise and maintain isochronicity whilst minimising resonance crossings.

The custom azimuthal field gradient is optimised to accelerate He²⁺, a particle with a charge to mass ratio of 1/2. This design, therefore, has the capability of accelerating any particle with charge to mass of 1/2. An ion of great interest would be fully stripped carbon ions (C⁶⁺) for an alternative ion treatment modality. Ionised molecular hydrogen (H₂⁺) could also be accelerated and used as a tool for imaging; allowing treatment and patient imaging from the same machine. The potential to treat and image using particles will reduce errors currently imposed by translating plans from CT [26]. However, it will only accelerate these other species to the same energy per nucleon. The design energy for helium ions is 900 MeV which translates to 225 MeV/u to achieve 30cm depth in tissue. For a single proton, 225 MeV/u is suitable for treatment, but 330 MeV/u is necessary to image a patient. The design energy of the machine will need to exceed the design energy for helium to be able to image with dihydrogen, to approximately 1300 MeV.

5.2 Field map optimisation

5.2.1 Initial map generation

The initial field and magnet parameters used are provided by Carol Johnstone, generated from a Mathematica script [106]. The script solves geometric and tune equations. Due to the nature of the movement of the working point of nsFFAGs, the primary objective of the Mathematica script is an attempt to stabilise the tunes. The output from the script is provided, and from here optimisation begins. The output of the file

is in the “Enge edge” format which identifies the accelerator by geometric layout and azimuthal radial field strength. An Enge edge file is described in appendix A.

5.2.2 Optimisation using FACT

The software used to optimise the provided field parameters is FACT; a specialised GUI for the COSY infinity code as discussed in Chapter 4. The provided accelerator field parameters as discussed in 5.2.1, are formatted for immediate entry into the FACT code. The input contains the information for a segment or cell of the accelerator and COSY mirrors the rest of the map based on this information, as demonstrated in Figure 5.1.

FACT is able to find stable equilibrium orbits for a given energy. For each magnet design, many stable orbits were identified using FACT across the acceleration regime. By studying the isochronicity profile of the stable equilibrium orbits it is possible to intuitively make changes to the different orders of magnetic field to optimise the acceleration regime within tolerances. Acceptable limits for isochronicity have been identified for fixed frequency acceleration for the orbits frequency to be within 0.1% of the operating frequency. To minimise losses and maintain beam quality, the total phase spread of the beam should be $\leq 40^\circ$ [107]. The phase spread of the beam can be identified as the total phase slip the particle experiences over the whole acceleration regime.

To satisfy the above criteria, a strict tolerance of $\pm 0.1\%$ of the mean ToF across the accelerating regime will be implemented. Whilst making changes to the magnetic field, the working point of the machine will move. It is important to consider the working point when optimising for isochronicity, as resonance lines may be destructive to the beam if crossed or the working point remains within proximity to resonance lines for many turns. As the working point moves, it is inevitable that some resonance lines may be crossed or approached. The working point and resonance crossings will be investigated using FACT and OPAL in this thesis. Resonance crossings are an issue in cyclotrons crossing the fixed resonance lines of different orders as described in Chapter 3. As the resonance order increases, typically after the 3rd order, the working point can cross them with minimal emittance growth. For lower orders, if a resonance crossing cannot be avoided growth can be minimised by crossing it perpendicularly and as quickly as possible. Cyclotron tune maps regularly cross higher order resonances without issue (typically 3rd order and above) but lower order resonances are avoided as they are rapidly destructive to the beam. EMMA [98], the worlds first nsFFAG, demonstrated that it is possible to cross a first order resonance if crossed fast, prohibiting the

5. INITIAL CHARACTERISATION OF BEAM OPTICS FOR NSFFAG DESIGNS

amplification of betatron oscillation growth.

5.3 FFAG design 1

The first FFAG design investigated here is a square FFAG design consisting of 4 cells, provided by C. Johnstone [106]. Each cell contains a large multipole bending magnet and a smaller defocusing wedge magnet, as depicted in Figure 5.1. The design has a starting energy of 250 MeV up to the design energy of 900 MeV. The magnets dimensions span from a radius of 2m to 7m, incorporating 2m straights between each quadrant of the design, which appears to have a magnet in between them. These green rectangular magnets observed at 0° , 90° , 180° and 270° are dummy magnets with no magnetic field. The dummy magnets are required by the code to create straights and satisfy the geometrical inputs of the code, and have no magnetic field. The purpose of the straights is to ensure there is enough space for sufficient injection, extraction and RF cavity insertion.

The isochronicity profile and the working point across the acceleration regime for different energies were identified, and are displayed as the red points on Figure 5.2. Based on the output data, the magnet parameters were optimised to flatten the ToF, and an attempt was made to maintain the current working point. The difference between the original provided parameters and the optimised parameters are portrayed in red and black, respectively. The tunes before optimisation are stable, but the ToF is an order of magnitude away from the acceptable tolerances for the isochronicity necessary for fixed frequency acceleration. The magnetic field profile for each order of magnitude was then optimised in an attempt to flatten the ToF profile, and maintain the tunes, but consequently the tune working point changes dramatically. In this optimised case the magnetic field profile was very different to the original design, in order to achieve a flatter isochronicity profile. Even after the iterations it can be observed that the ToF is not within the necessary tolerances and more so the tunes are now not acceptable. Before the tunes moved locally around 3rd and 4th resonance lines, whereas after optimisation, they cross a 1st order resonance once, a 2nd order twice and 3rd and 4th order resonances many times.

The optimised field design parameters were reinserted into the Mathematica script and many different field configurations were generated with different geometries, with acceptable tunes. Figure 5.3 demonstrates some of the alternative geometries that were optimised in the same way as discussed above. The exact details of these designs are spared from this thesis, but the outcomes are identical to the above discussed design.

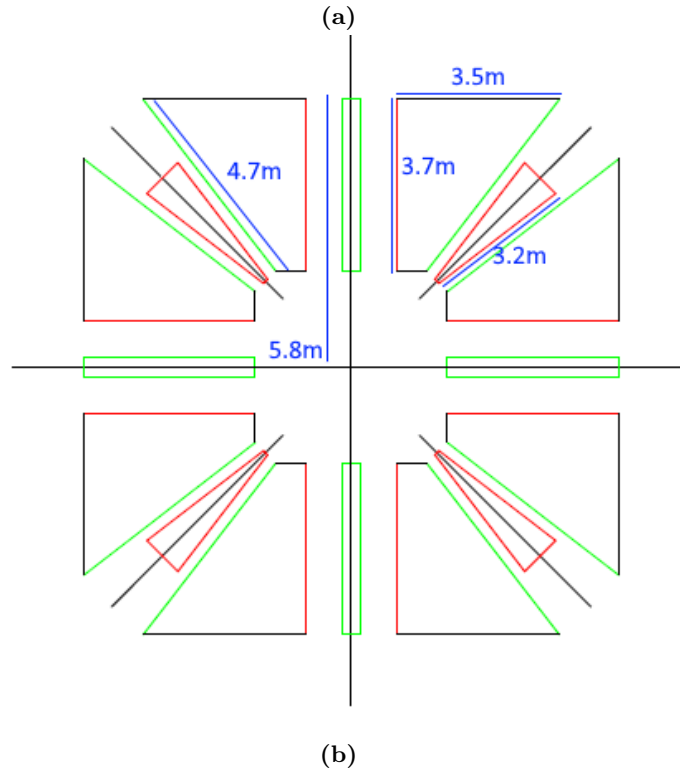
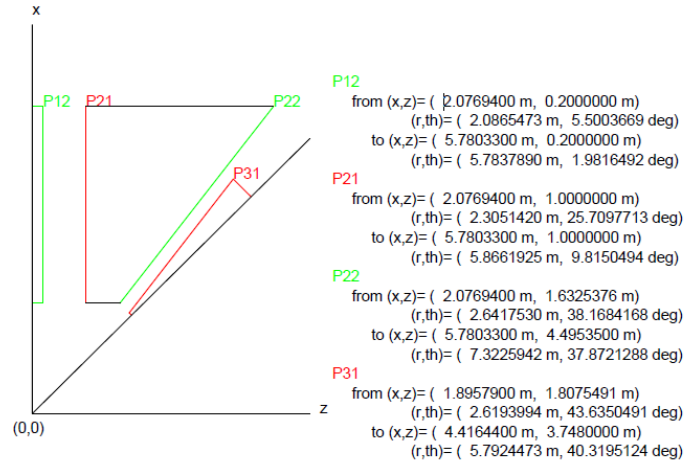
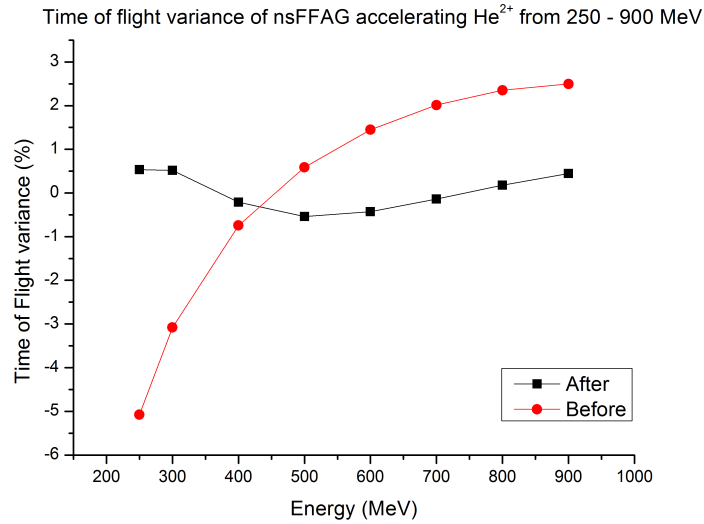


Figure 5.1: nsFFAG accelerator layout provided by C. Johnstone. (a) The initial quadrant to be mirrored to create the full accelerator. (b) The full accelerator geometry.

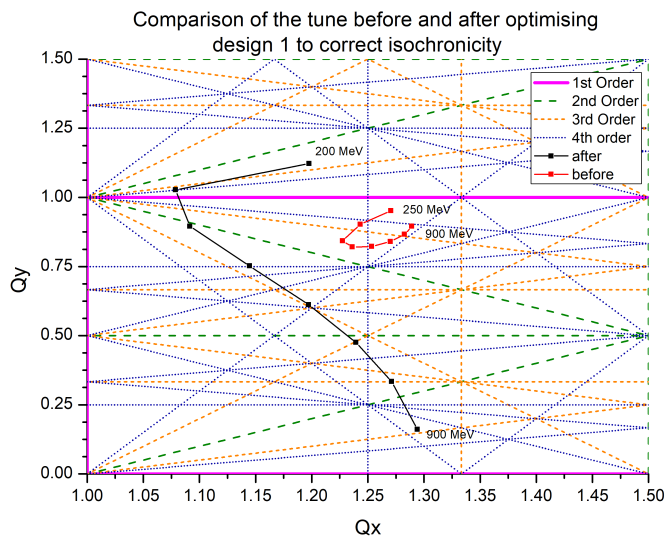
Major adjustments were necessary to the initial parameters which made the provided tunes unstable and the isochronicity profile was never within the necessary tolerances.

There is an additional problem that these maps also started at around 200 MeV and a pre-accelerator would be required at this point to reach these energies. Knowing

5. INITIAL CHARACTERISATION OF BEAM OPTICS FOR NSFFAG DESIGNS



(a) The Time of Flight for design 1



(b) The tune variation for design 1

Figure 5.2: A nsFFAG accelerator layout provided by C. Johnstone. On both Figures, red represents the values before optimisation and black afterwards

at this point multiple acceleration stages are needed, it was decided to step aside from this design and separate the study into two separate designs, which will be referred to as stage 1 and stage 2. Stage 1 will aim to accelerate ideally from as low as energy as possible, to as high as possible isochronously.

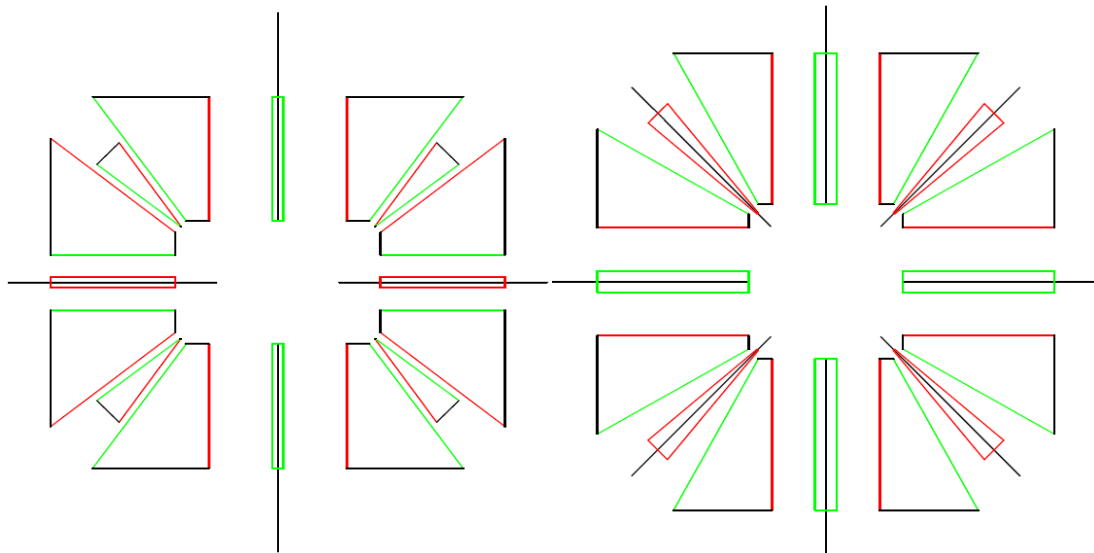


Figure 5.3: Different accelerator layouts provided by C. Johnstone that were optimised

5.4 Stage 1 design

Other work in our FFAG collaboration looked at proton acceleration at lower energy (design energy of 30 MeV) for isotope production, the accelerator was called the proton isotope producer (PIP). The original design for PIP also originated from C. Johnstone, which used a simpler design with no counter bending magnets or straights. The work on PIP led to the idea to adapt this model and see if it could be used as the pre-accelerator or first stage of acceleration for the helium accelerator. PIP accelerates protons from 75 keV to 28 MeV and can already accelerate He^{2+} because the design energy of the machine is in the very early stages of the relativistic regime. Up to this energy the beam rigidity of He^{2+} is nearly identical to that of protons [108]. This will not hold true when adapted, as the particles energy will reach the relativistic regime and changes will need to be made; however, it remains a good starting point.

Initial steps of adapting this design began with increasing the radial geometry of the bending magnets to extend the energy range of the machine; no other parameters were adjusted. Figure 5.4 shows the ToF variation, relative to the mean ToF, for the extended field map up to a radius of 3m. The stage one design holds the same issue as PIP, where at the inner radii the fringe fields overlaps. This field overlap suppresses the vertical tune, which can be observed in the tune map for both designs, and hence the change in the ToF. The initial start energy was increased from 75 keV to 500 keV.

5. INITIAL CHARACTERISATION OF BEAM OPTICS FOR NSFFAG DESIGNS

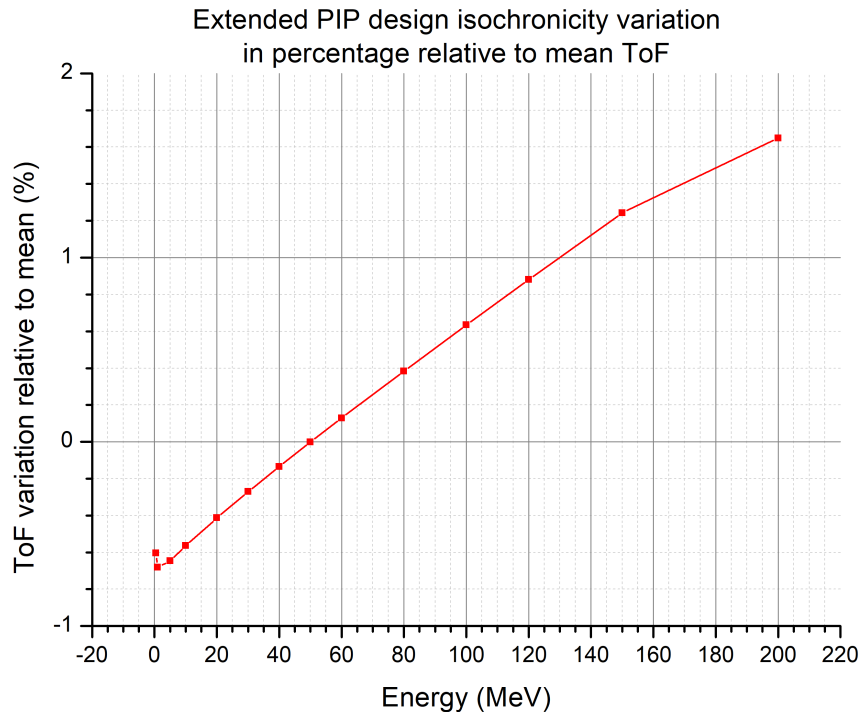


Figure 5.4: Initial ToF results from extending the design radius of the Proton Isotope Producer (PIP), a different FFAG design within the collaboration [108]

The increase in start energy was due to the adaptation of the magnetic field gradient causing the fringe field overlap to increase, and a stable orbit could not be achieved at such a low energy. After many iterations, the results are shown in Figure 5.5 with some iterations in-between demonstrating the progression made with changes.

The same methods to optimise the initial design field parameters to improve the ToF and tune were used to optimise this design. It can be seen overall the isochronicity across acceleration regime is reasonable and within the desired limits, bar the initial acceleration. The tune does cross an integer resonance because of this, but the crossing is at low energy, and nearly perpendicular to the resonance line. Providing the energy gain per turn is large enough, the slip will be overcome quickly, and significant emittance growth and beam loss can be avoided.

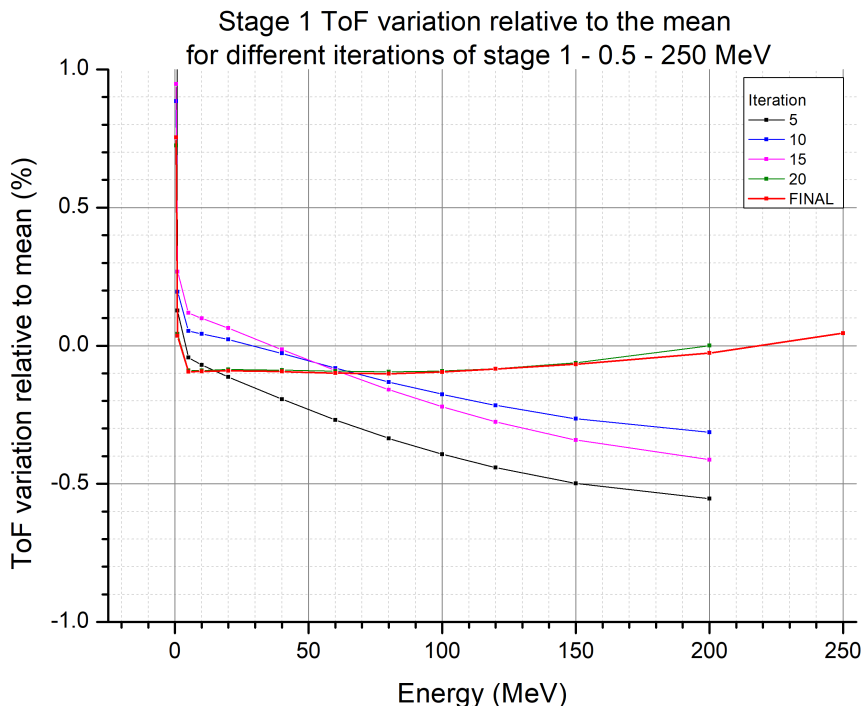


Figure 5.5: Isochronicity profile for Stage 1 (extended PIP) for various iterations detailing the progression made

5.4.1 Stage 1 further development

Using the information in Figure 5.5, it is seen that this design can accelerate He^{2+} isochronously from 2 MeV to 250 MeV. However there a few changes could be made to improve the isochronicity and extend the energy range of the machine further.

The mean ToF will be skewed by the large ToF variation caused by the inner radii. The inner radii are affected by the fringe field overlap which has a detrimental effect on the ToF and tunes, as demonstrated by the ToF at 0.5 MeV. Injection may still be possible at 0.5 MeV, as the rapid change in ToF will cause a phase slip, but it should be recoverable if the energy gain per turn is large enough. The initial phase slip may also affect beam quality by increasing the total phase slip across the acceleration regime. As a result, it may be more practical to increase the injection energy to 1 MeV. At this energy the fringe field overlap is considerably reduced, and hence the phase slip. The reduced initial phase slip will accommodate for a greater phase slip at higher energies, potentially extending the energy range of the machine, and should be

5. INITIAL CHARACTERISATION OF BEAM OPTICS FOR NSFFAG DESIGNS

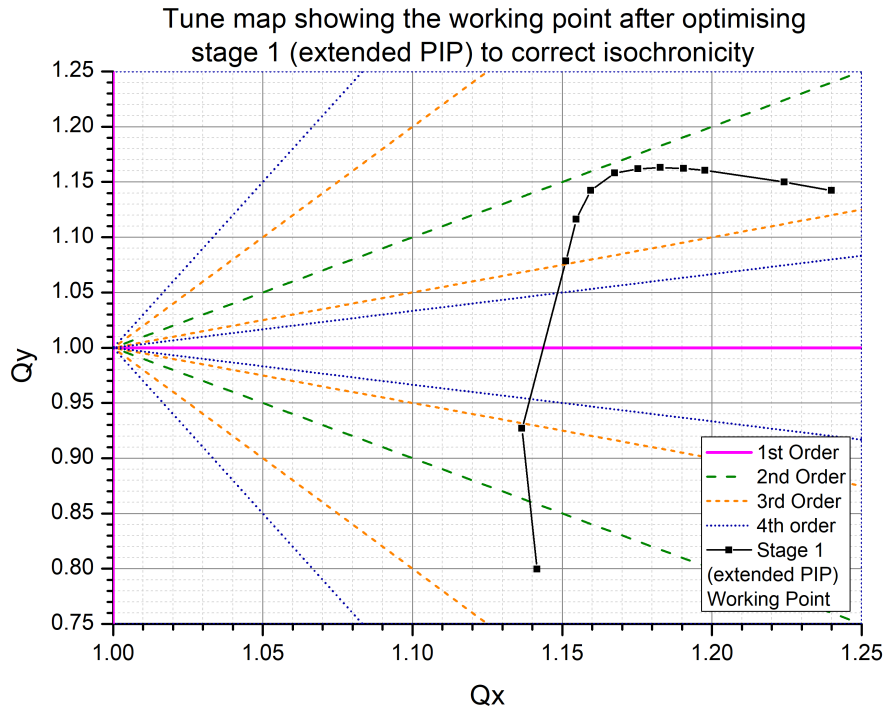


Figure 5.6: Final optimised iteration of stage 1 (Extended PIP) tune map detailing the movement of the working point of the machine

easier to overcome.

From the isochronicity profile the ToF changes gradually becomes slower as the energy of the particle increases and reaches the tolerance of 0.1% at 250 MeV. The reduction in ToF at higher energies could be counteracted by changing the physical magnet angle of the design. Changing the physical magnet angle will affect the time the particle will be influenced by the hill of the magnetic field in an orbit. A depiction of the magnet angle can be found in Figure 5.7 The adjustment of the magnet angle would complement the reduced ToF at larger radii and provide a larger bending radius for the beam, whilst having a reduced effect at the inner radii of the design.

When optimising, a design energy limit is necessary, and 250 MeV was selected based on the starting energy of the previously optimised racetrack designs. However, the design energy could be increased from 250 MeV; 400 MeV being an ideal energy. This energy was chosen based on the fact this would be 100 MeV/u, and this corresponds to a depth of approximately 10cm in water. A 10cm depth in water is clinically relevant

and has the potential for treating a range of shallow tumours, for example, paediatric head and neck tumours. The radius of a 5-year-old boy is approximately 8.2cm [109], accounting for the extra water equivalence for the thickness of the skull, a 10cm beam should be sufficient to treat paediatric tumours. This would mean that stage 1 has a potential to be used without stage 2.

The magnetic field gradient is now exceeding the limits of normal conducting magnets, 2 Tesla, and the magnets will need to be superconducting to handle the magnetic field. The use of superconducting magnets is not envisaged to be a problem, as 8 Tesla is achievable with superconducting magnets, and the magnetic field strength does not exceed 4 Tesla. With the increased magnetic field, the pole gap between the magnets is thought to be too small, at 2cm, because more space will be needed to cool the magnets. This would need to be increased to at least 4cm. Having achieved part of our goal after many design iterations, it was decided to give the project a name: HEATHER, HElium ion Accelerator for radioTHERapy.

5.5 HEATHER Stage 1 final design

Applying the modifications suggested in Section 5.4.1, the magnet wedge angle was increased by 2° and the pole gap between the magnets increased to 4cm. The starting energy was increased to 1 MeV and the design energy increased to 400 MeV. After introducing the magnet angle and pole gap changes, optimisation was successful, and a final design was reached. Figure 5.7 depicts the physical layout of the accelerator, with an outer radius of 3.5m. The field gradient as a function of radius is shown in Figure 5.8, with a peak field of around 4 Tesla.

OPAL, a charged particle code capable of 3D space charge, was used to verify the results from COSY.

To calculate a ToF in OPAL, the stable equilibrium orbit for a given energy needs to be identified. This is found by iterating the starting radius and angular momentum until the particle survives, for which a thousand turns with minimal azimuthal deviation was deemed sufficient. Once the stable equilibrium orbit has been found, a non-interfering probe is inserted into the machine cutting the orbit perpendicularly. It is found that each turn the particle passes the probe, the time is recorded. The average revolution time is then calculated for each turn and used as the ToF for that energy. The final design ToF is almost within the limits proposed earlier within this chapter. This means it should be possible to begin acceleration at 1 MeV, but consequently with a small phase slip. It is within the tolerances at 2 MeV, and this should be reached in less

5. INITIAL CHARACTERISATION OF BEAM OPTICS FOR NSFFAG DESIGNS

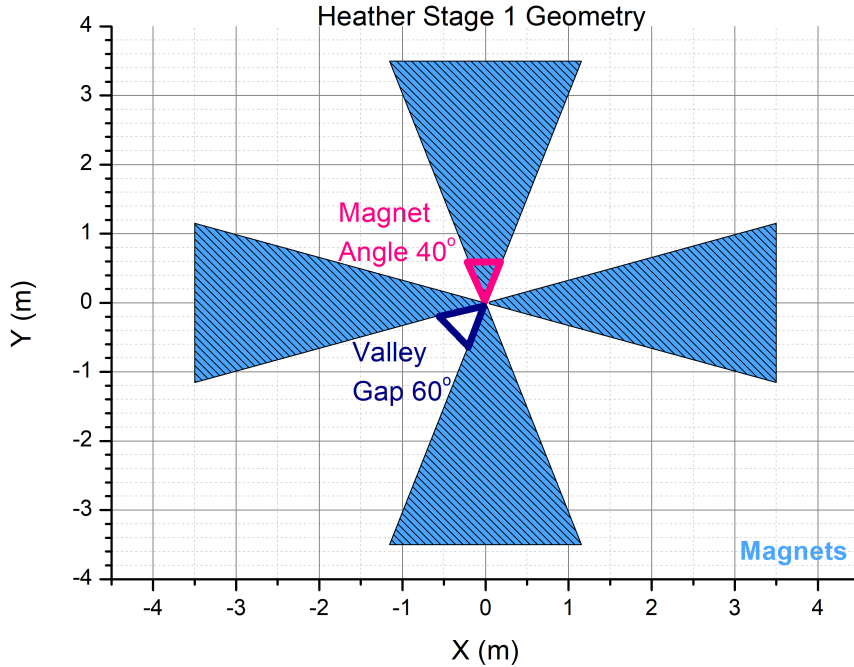


Figure 5.7: Final optimised geometry of stage 1

than 3 turns. The ToF for both COSY and OPAL are compared in Figure 5.9; they show excellent agreement. The mean ToF for stage 1 is 99.067ns which translates to a frequency of 10.0942 MHz.

OPAL is also capable of calculating the tunes, which it does by simulating 2 particles, the reference particle and a displaced particle. Fourier analysis is used to identify the orbit difference between the two particles. The tunes were also computed and compared to COSY, as illustrated in Figure 5.10. Vertical tune suppression is evident, which causes the rapid ToF variation observed at lower energies. This does cause a 1st order resonance crossing, however if this is traversed quickly it should not be detrimental to the beam. A greater concern may be the time spent near the 2nd order resonance line, as it will take a few turns to surpass, and it may be enough to cause emittance growth; this will be further investigated when a beam is accelerated in Chapter 6. There is good agreement between both codes, however there is a slight disagreement when the fringe fields become stronger. The disagreement could also be due to the radial granularity of the field map produced from FACT for OPAL at smaller radii.

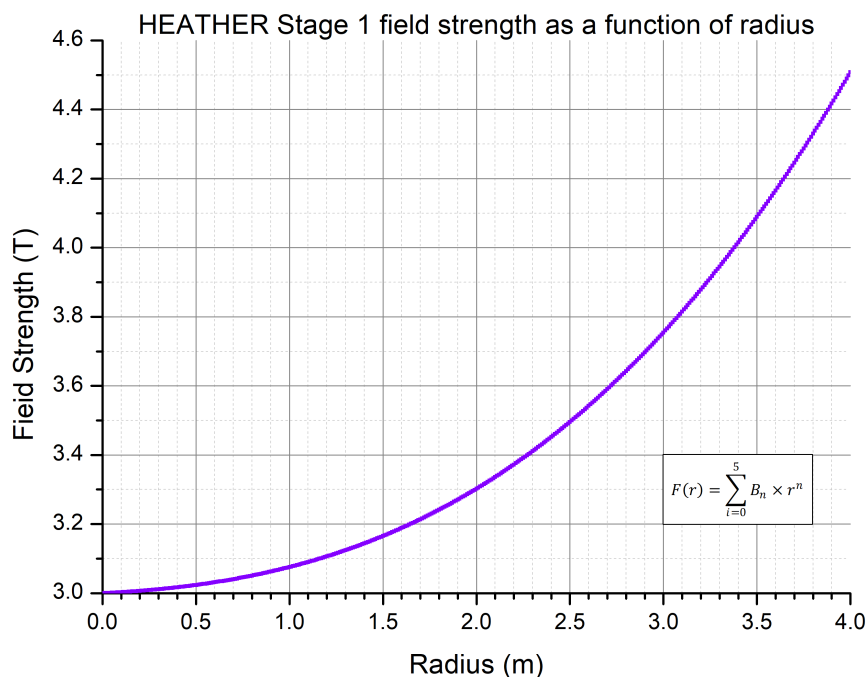


Figure 5.8: The azimuthal magnetic field gradient for stage 1

The change in starting energy is much higher than the original 75 keV, and a pre-accelerator will be necessary. Accelerating from source to 1 MeV is achievable and has been demonstrated with protons at PSI from source to 870 keV before entering the injector 2 cyclotron. The stage 1 design suggests that given enough energy gain per turn, it should be possible to isochronously accelerate He^{2+} from 1 MeV to 400 MeV; or any other particle with charge to mass ratio of 1/2. This is beyond the original foreseen scope of the 1st stage and may provide a standalone solution for helium therapy without stage 2. This also is a very versatile option going into stage 2 as the exit energy for stage 1 is higher. The increased exit energy allows for a lot more flexibility when designing the start energy for stage 2.

The dynamic apertures were investigated in OPAL across the acceleration regime, and the smallest acceptance was found to be approximately $20 \pi \text{mm mmrad}$ in the horizontal and vertical planes.

5. INITIAL CHARACTERISATION OF BEAM OPTICS FOR NSFFAG DESIGNS

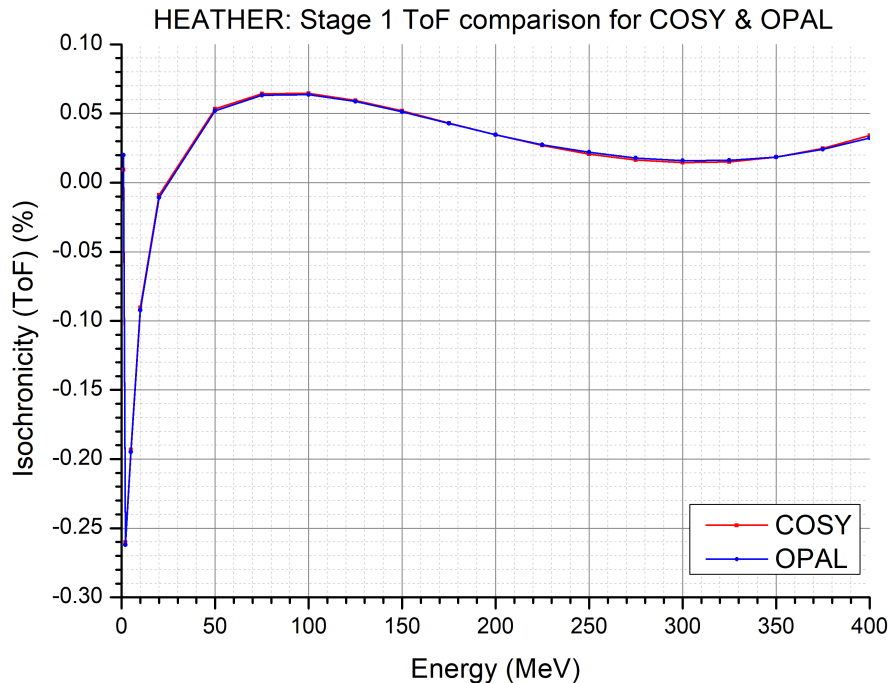


Figure 5.9: Stage 1 isochronicity profile from 1 MeV to 400 MeV comparing results from FACT and OPAL

5.6 HEATHER stage 2 design

Having reached 400 MeV total energy, the next step was to increase this to 900 MeV. To increase the energy the current stage needs to be modified or a new accelerator needs to be designed. Rather than revisiting the designs discussed in 5.3 or starting a design from scratch, a modification to Stage 1 was attempted to increase its energy range. The concept of having a racetrack design is desirable to increase the availability of space, stage 1 was redesigned with straight sections. Additional space created by a racetrack design could be used to insert cavities, or to inject / extract the beam. As opposed to increasing the existing gap between the magnets and rotating the design, it was pulled apart and the straight inserted along the vertical axis. The physical construction of the machine is still a thought when designing, and the idea is that all the magnets have an identical field gradient to try and aid that process. Figure 5.11 portrays the concept of putting the straight into stage 1. Note, as previously the green rectangles are not

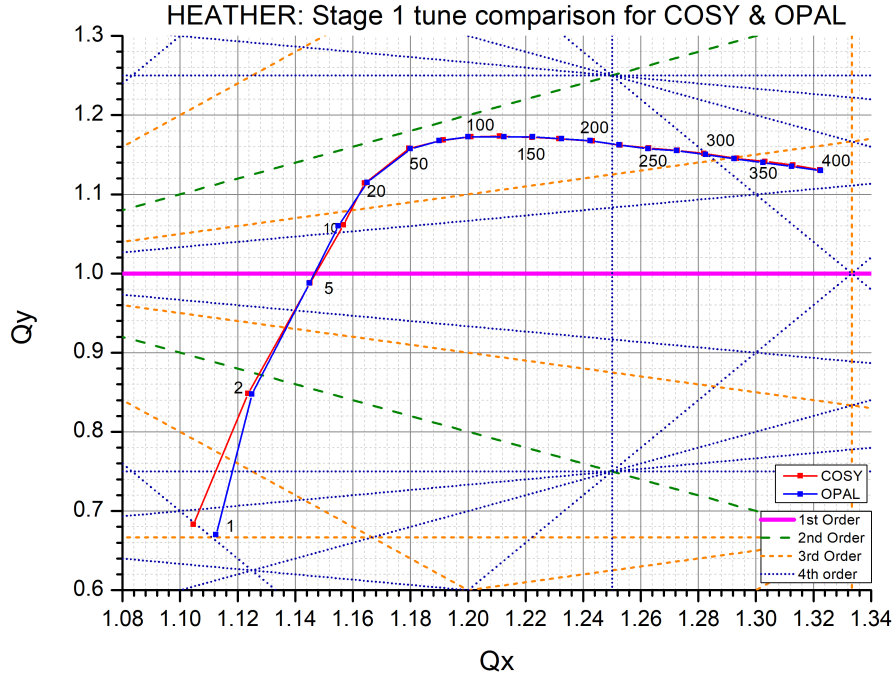


Figure 5.10: Comparison of the working point for stage 1 in FACT and OPAL

magnets, they are just necessary for the purposes of magnet geometry in the code.

One of the issues with the original design was the fringe field overlap, and the addition of a straight would pull these orbits away from the inner radii, providing more room for cavities, injection and extraction. Consequently, the footprint of this design would be larger with the straight section, but it is still a reasonable size comparatively and the accelerator should fit in current bunkers, as discussed in Chapter 2.

With the introduced straights the starting energy was expected to be higher because of the increased path length. The lowest stable orbit for was sought after around 10 MeV, but a stable orbit could not be achieved until 30 MeV with a significant ToF variation for this parameter configuration. Each iteration depicted in Figure 5.12 attempts to build on the issues of the previous iteration by adjusting the B_n values described earlier in Equation 4.1. The iterations in Figure 4.1 alter the quadrupole and sextupole component of the design, in an attempt to raise the ToF of the higher energies. As iterations of the design progressed the parabolic ToF could be improved, but not enough to satisfy isochronous conditions up to 400 MeV to match the original

5. INITIAL CHARACTERISATION OF BEAM OPTICS FOR NSFFAG DESIGNS

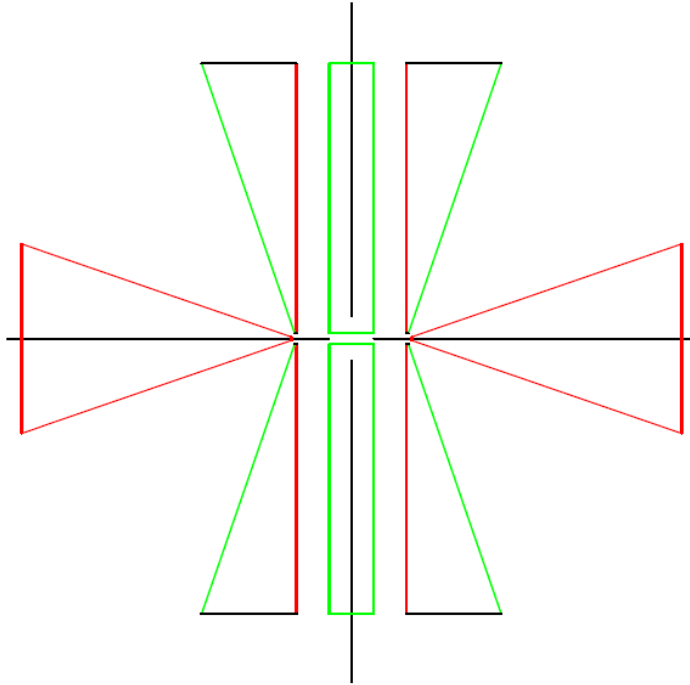


Figure 5.11: A depiction of the concept of putting the straight into stage 1

idea, as highlighted in Figure 5.12.

It can be observed that steadier isochronicity is present over a higher energy range from iteration d in Figure 5.12. From the first attempt at optimising this design, it suggests Stage 2 could be viable to accelerate from 400 MeV to 900 MeV through a second accelerator. From iteration d specifically the region from 250 MeV through to 400 MeV which would be a great starting point for a second stage; it is relatively isochronous and there are no issues with fringe field overlap. The focus then switched to adapt the design to satisfy the requirements for a 2nd stage based on its isochronicity profile; continuing the acceleration from 400 MeV to 900 MeV.

Based on iteration d in Figure 5.12, Initial iterations started at an energy of 200 MeV, as opposed to the 400 MeV achieved by stage 1. The decrease in starting energy for stage 2 was based on the isochronicity profiles originally optimised, however the design energy of 900 MeV has not changed. Figure 5.13 details further iterations carried on from iteration d of Figure 5.12, but over the energy range of 250 MeV to 900 MeV. As previously, Optimisation between successive iterations is achieved by changing the magnitude of the magnetic field for different magnetic field orders. The design demonstrates the potential to achieve the isochronicity profile within the

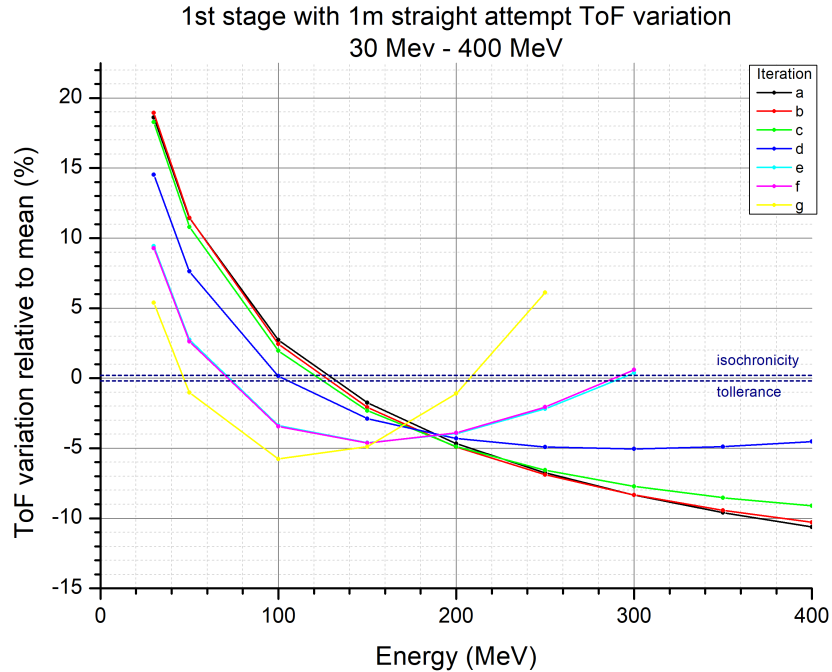


Figure 5.12: A depiction of the concept of putting the straight into stage 1 for different iterations of the design

necessary tolerances from 400 MeV to 900 MeV, but it was again difficult to contain the parabolic ToF beyond the core requirements of stage 2, reducing the flexibility of the design. This is unfortunate as a 200 or 300 MeV starting energy would reduce the energy of stage 1, reducing its footprint. Figure 5.13 demonstrates that the design is not sufficiently isochronous over the entire acceleration regime, where the green band highlights the 0.1% boundaries for all configurations. The additional red band was placed off zero demonstrating the isochronous potential that could be achieved by beginning acceleration at 400 MeV. Starting at 400 MeV is an option, but consequently would increase the footprint of the overall design, using the maximum footprint for stage 1.

Increasing the start energy to 400 MeV for the 2nd stage was found to be successful. After many iterations the ToF is comfortably inside the isochronicity boundaries, and the tunes are acceptable; no 1st or 2nd order resonances are crossed, only 3rd and 4th order. The results shown in Figure 5.14 are from FACT.

5. INITIAL CHARACTERISATION OF BEAM OPTICS FOR NSFFAG DESIGNS

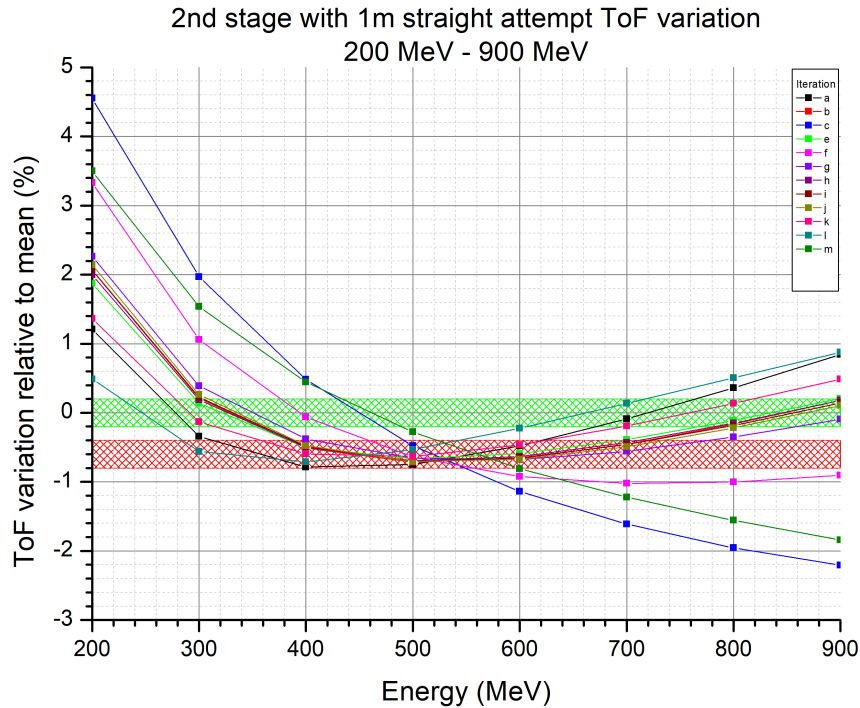
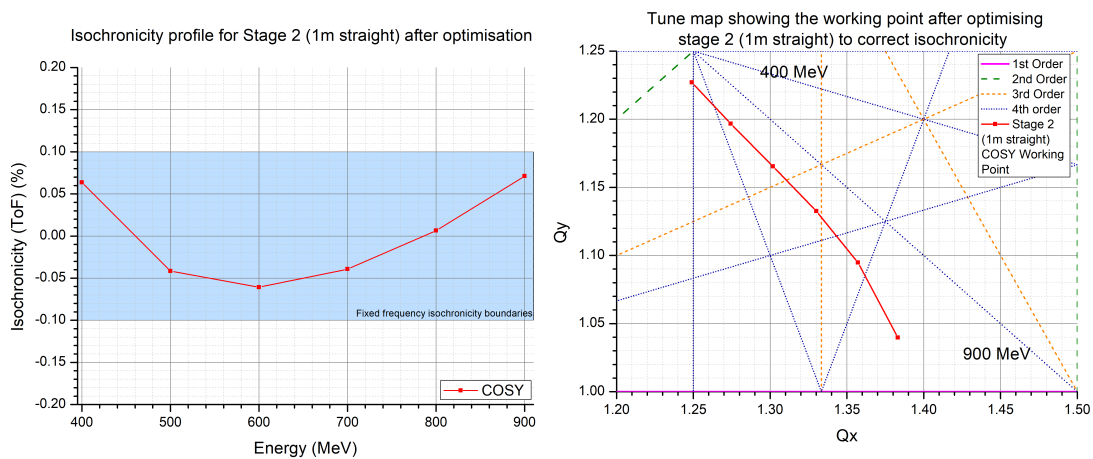


Figure 5.13: ToF profile for iterations for the energy range 200 MeV to 900 MeV.



(a) Isochronicity profile for Stage 2 v1

(b) Tune map showing the working point for Stage 2 v1

Figure 5.14: Stage 2 version 1 with an energy range from 400 MeV to 900 MeV

5.6.1 Differences between stage 1 and stage 2

Although the latest iteration satisfied the necessary isochronicity and tune conditions for stage 2, the overall goals of isochronous acceleration through to 900 MeV were not met. The average ToF of 92.35 ns and corresponding frequency of 10.8286 MHz does not match that of stage 1. The difference in frequency is too large and would prevent isochronous acceleration over both accelerating regimes with the same frequency; further optimisation is necessary to achieve this.

To attain isochronicity in both stages the revolution time for stage 1 needs to be decreased, or the revolution time for stage 2 needs to be increased. Decreasing the revolution time for stage 1 requires reducing the magnetic field, which would increase the footprint as it would push the orbits outward. The Stage 1 fringe fields also complicate the design at the inner radii which are currently manageable. Reducing the magnetic field will reduce the strength of the fringe field, however a smaller proportion will be affected by the fringe fields, and the ToF will have much more variation radially at the inner radii. Stage 2 has more flexibility spatially and does not have overlapping fringe fields complicating optimisation at the inner radii. To increase the orbit velocity for stage 2 would require increasing the magnetic field strength, which would reduce the footprint of the accelerator. It was identified changing stage 2 would be easier than adapting stage 1.

5.7 Stage 2 final design

Stage 2 was further optimised, to match stage 1, and the average ToF was decreased to 99.079 ns. The mean ToF values between stage 1 and stage 2 are now within 1% of each other; suggesting the possibility that a single frequency could accelerate He^{2+} through both stages successfully. The final magnet layout and field gradient are depicted in Figure 5.15.

The straights were inserted to aid injection and extraction however the gaps are larger on the bends. It would be preferred to put the cavities in the straights and complete injection and extraction in the gaps between the bending magnets. Having the cavities in the straights helps with the optics because the design will be symmetrical.

In addition to matching the operating frequency for each machine, the overall ToF variation relative to the mean for stage 2 was reduced by approximately 2/3 from 0.13% to 0.04%. The improved isochronicity is illustrated for both COSY and OPAL in Figure 5.16. Both COSY and OPAL are in good agreement, however there is some

5. INITIAL CHARACTERISATION OF BEAM OPTICS FOR NSFFAG DESIGNS

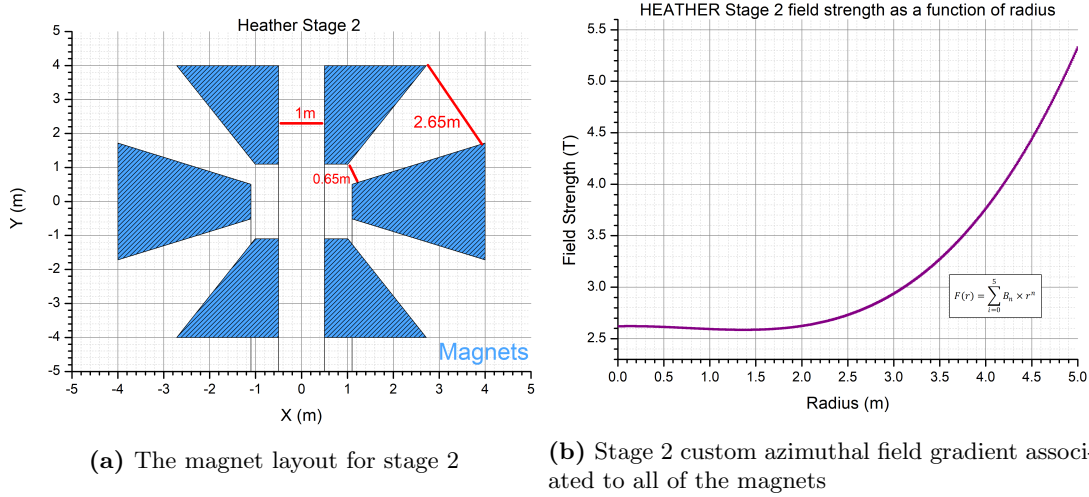


Figure 5.15: Stage 2 finalised physical parameters

slight variation between the two codes; this is negligible and believed to be down to the computation of the field map because of the straights and field map granularity.

The working point also has some discrepancies between OPAL and COSY as seen in Figure 5.17. The variance in working point between the two codes is also believed to be caused by the same issues as for the ToF. Notably the tunes cross a 2nd order resonance line initially but after this only 3rd and 4th order resonances are crossed. There is a concern that the resonance crossing may cause emittance growth, but this will not be fully discovered until the acceleration of particles are simulated, which will be investigated in Chapter 6.

5.8 Chapter summary

In this chapter I have achieved the first steps in isochronously accelerating He^{2+} , by creating and optimising a two-stage accelerator with acceptable tunes and ToF across both machines. The steps taken and progress made have been discussed, and the initial design parameters met. The next steps in the design phase is to accelerate a single particle through the machine, which is discussed in the next chapter.

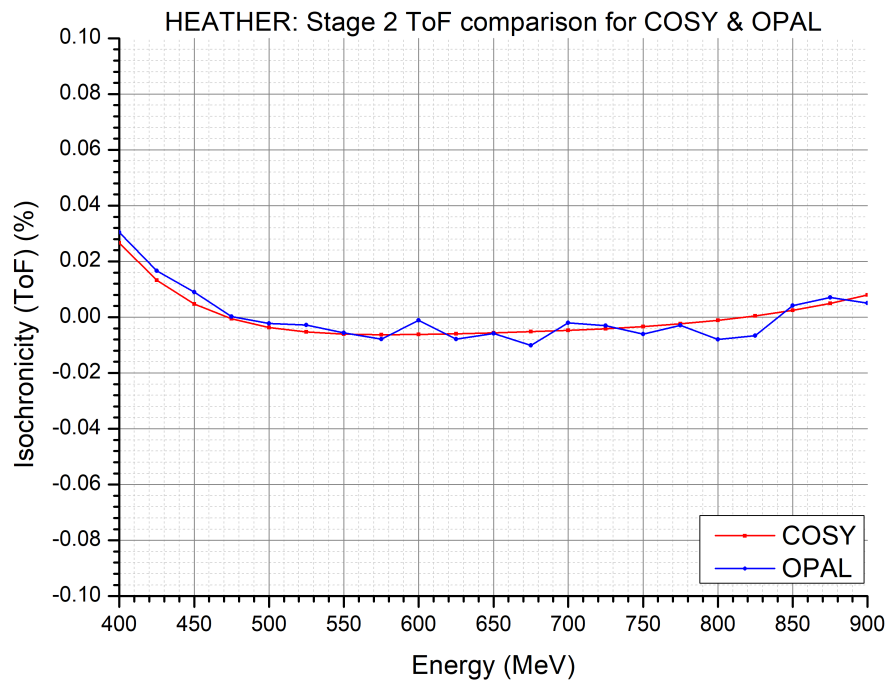


Figure 5.16: The isochronicity profile across the acceleration regime for stage 2 comparing COSY and OPAL

5. INITIAL CHARACTERISATION OF BEAM OPTICS FOR NSFFAG DESIGNS

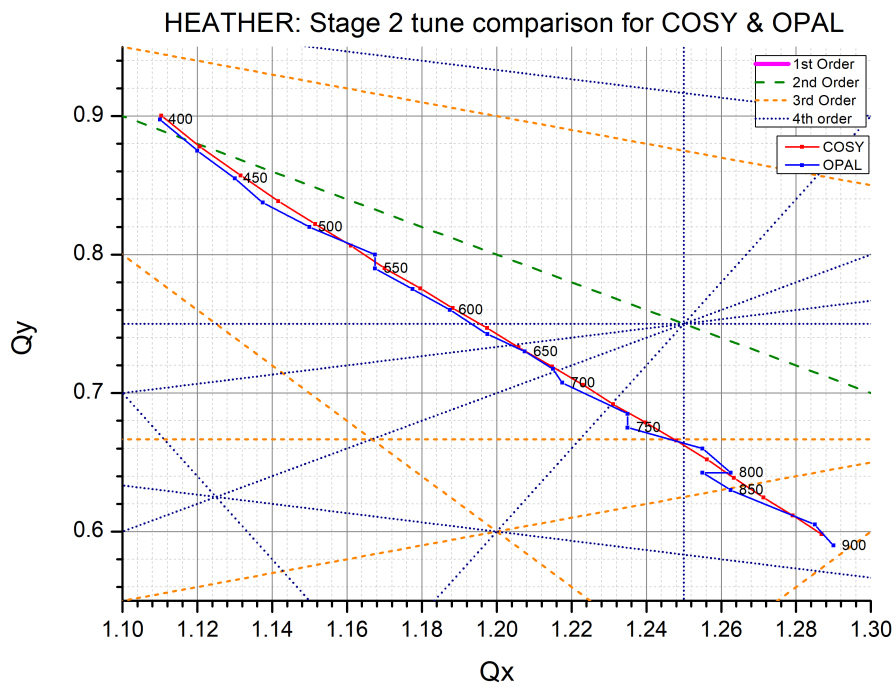


Figure 5.17: The tune diagram showing the working point for stage 2, comparing results from COSY and OPAL.

6

Acceleration studies and RF Characterisation

This chapter covers single particle acceleration through stage 1 and stage 2 for HEATHER. In the previous chapter, stable equilibrium orbits were calculated across the desired energy regime for both stages 1 and 2. From the stable equilibrium orbits, the time of flight (ToF) was calculated and the isochronicity compared and discussed in two particle tracking codes. Adjustments were made to ensure the ToF for each stage is as close as possible, in order to operate with fixed frequency acceleration across both stages. The difference in frequency between the stages was achieved to within 1%.

This chapter will place RF accelerating structures within the accelerator designs for both stages and identify the optimal operating frequency to be used across both stages. Once the operating frequency is identified, the injection parameters will be optimised to achieve ideal accelerating orbits. RF systems in current operation in separate sector machines, alongside the voltage thresholds proposed by the Kilpatrick limit, will be used to identify and suggest RF parameters achievable with current technology. These parameters will then be simulated using OPAL and conservative realistic parameters selected to be used when one begins to accelerate beams of particles. This will help to show that the design is feasible beyond a theoretical stage (or concept).

6.1 RF in Cyclotrons

Electrodes called dees were originally used to accelerate particles in cyclotrons, given their name by their semi-circular shape resembling the letter “D”. Two dees were situated in the pole gap between the two magnets and a sinusoidal electric field gener-

6. ACCELERATION STUDIES AND RF CHARACTERISATION

ated between them. This created two accelerating gaps, 180° apart, where traversing particles gained energy as given in Equation 6.1

$$E_t = 2qV_0 \cos(\phi) \quad (6.1)$$

Where E_t is the energy gained in MeV per turn, q is charge, V_0 is the RF voltage in MeV and ϕ is the phase of the particle at the centre of the accelerating gap. The factor of two appears because the particle crosses two accelerating potentials.

In a classical cyclotron, the ideal particle is perfectly isochronous; or synchronous. The particle will arrive at the centre of the gap in perfect time with the alternating voltage and experience no change in phase. If the particle phase is not ideal, it would arrive early or late in time at the accelerating gap with respect to the synchronous particle. A non-synchronous particle will become out of phase with the RF voltage, as described in Equation 6.2, this changes the maximum kinetic energy the particle receives from the RF system.

$$\phi = \omega_{\text{total}} \Delta\tau \quad (6.2)$$

Where ϕ is the phase of the particle, ω_{total} is the orbital frequency in MHz and $\Delta\tau$ is the difference in orbital time between the synchronous particle and the time of the particle accelerated by the operating RF.

The difference in phase between the synchronous particle and the accelerated particle is known as the phase slip, and has a direct effect on energy gain as shown in Equation 3.3. A phase slip will lead to a reduced energy gain per turn and increase the overall time of the acceleration regime. Providing the particle phase stays within $-\pi/2$ and $\pi/2$ whilst accelerating, it will receive energy from the RF system. Note that with a consistent phase slip, the particle phase may exceed these boundaries, decelerate and lose energy to the RF system. However, it is desired to keep the total phase slip within 40° , to avoid this and maintain beam quality. When the energy of the accelerated particle enters the relativistic regime, the particle's mass increases, hence $\Delta\tau$ increases. To maintain fixed frequency RF, the accelerator must have a customised azimuthal gradient to counteract the increased mass to maintain synchronism as discussed in Chapter 3. The FFAG design presented in this thesis will have a custom azimuthal field gradient, and from the stable orbit analysis in Chapter 5, the operational RF frequency does not exactly match the synchronous frequency. As the ideal particle will arrive early or late the resulting phase slip will need to be managed.

With the development of isochronous cyclotrons, hills and valley were introduced

and which naturally led to separate sector magnet designs to increase the axial focusing term. Separate sector designs allow more room for beam instrumentation and could cater for the insertion of RF cavities in the valleys of the machine. Separate sector designs allow for more efficient acceleration as classically injection, extraction and acceleration all had to occur at the dee gap. Separate sector designs have the space to accommodate resonant RF cavity designs. Using separate sector machine designs the number of RF structures could increase, providing more efficient and powerful RF [110] [111]. HEATHER is a two stage separate sector design, therefore it is possible and logical to use RF cavities as opposed to dees.

6.2 Kilpatrick limit

By using RF cavities in the design, multiple cavities can be inserted in to the accelerator. This in turn means the particle sees more accelerating voltage, which is crucial for increased turn separation. Turn separation describes the space in between successive orbits radially for cyclic machines that vary magnetic field as a function of radius. When extracting the beam, turn separation is an important parameter as typically instrumentation will need to be placed between successive orbits. The orbit separation or radial increment per turn for an isochronous cyclotron can be identified by the Equation 6.3 [112]

$$\frac{dR}{dn_t} = \frac{R}{\gamma(\gamma^2 - 1)} \frac{U_t}{m_0 c^2} \quad (6.3)$$

Where R is the orbit radius, $U_t/m_0 c^2$ is the energy gain per turn and γ is the Lorentz factor.

Cavity design is extremely complex, and a full detailed design is beyond the scope of this thesis, but simple considerations have been made to imitate an achievable RF structure. These considerations are the voltage used, the gap size and the harmonic used; which can all be considered when investigating the Kilpatrick limit and discussed below in detail. The Kilpatrick limit is based on empirical data taken by W.D. Kilpatrick in 1957 [25], used to calculate the maximum electric field achievable for a given frequency before RF breakdown occurs. RF breakdown occurs when breakdown voltage is reached for an insulating material and it begins to conduct electricity; potentially resulting in physical damage to the structure. The data was readdressed by T.J Boyd, 1982 [113] and represented by Equation 6.4.

6. ACCELERATION STUDIES AND RF CHARACTERISATION

$$f = 1.64 \cdot E_k \cdot \exp\left(\frac{-8.5}{E_k}\right) \quad (6.4)$$

Where f is the frequency of the cavity, E_k is the maximum electric field achievable on the material surface in MV/m . This can be solved for E_k for a given frequency, as shown in the appendix, and as depicted below in Figure 6.1.

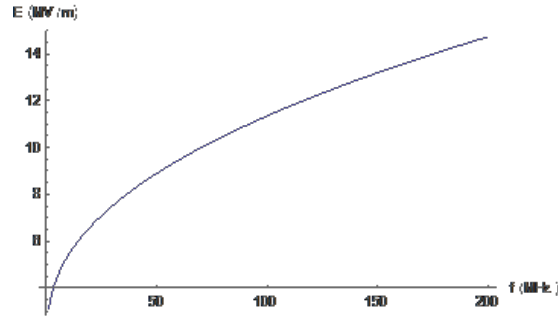


Figure 6.1: Frequency as a function of energy based on the empirical data by W D Kilpatrick [25]

It can be observed that the breakdown voltage threshold increases as a function of the square root of the frequency, hence higher frequencies yield greater acceleration potential. The orbital frequency of the machine is a physical property and cannot be changed, but the operating RF frequency can be operated at integer multiples of the orbital frequency, known as harmonics.

6.2.1 Harmonics

The principle of RF in a classic cyclotron is the alternating electric field switches exactly at the point when the particle crosses the accelerating gap. This is achieved by matching the RF system's operational frequency to the fundamental frequency of the machine. It is also possible to operate the RF at an integer multiple of the fundamental operating frequency, known as a harmonic, as expressed in Equation 6.5.

$$F_{\text{RF}} = nF_0 \quad (6.5)$$

Where F_{RF} is the RF frequency in MHz, n is the harmonic number, expressed as an integer, and F_0 is the operational frequency of the machine, or in this case the 1st harmonic.

Operating at higher harmonics has a detrimental effect to the beam. Because the

voltage is coupled with a sinusoidal frequency, as the harmonic increases, the amount of time the particle is accelerated reduces, as there are n acceleration segments across the accelerating gap. The reduced acceleration results in an increasing phase slip, resulting in the effects as previously described above.

6.2.2 Transit time factor

The coupling of the voltage to an RF field makes the voltage time dependent, and the particle speed will change as a function of position across the accelerating gap. The time dependent voltage will have an effect on the energy gain of the particle traversing the cavity and is taken into account by the transit time factor. The transit time factor can be expressed as an additional term T in Equation 6.1, as shown in equation 6.6

$$E_t = qV_0T \cos(\omega t + \phi) \quad (6.6)$$

Where $t = 0$ at the centre of the gap, and ϕ describes the phase of the RF field relative to the crest. If we assume the velocity change across the gap L is negligible, we can interpret ωt as [114].

$$\omega t = \omega \frac{L}{v} = \frac{2\pi c}{\gamma} \frac{L}{c\beta} = \frac{2\pi L}{\beta\gamma} \quad (6.7)$$

If we then substitute Equation 6.7 into 6.6 and integrate over the accelerating gap length of L from $-L/2$ to $L/2$, the transit time T can be found

$$T = \frac{\sin(\frac{\pi L}{\beta\lambda})}{(\frac{\pi L}{\beta\lambda})} \quad (6.8)$$

The transit time factor may be interpreted as a contributor to accelerator efficiency. Generally, the transit time factor decreases as a function of increasing gap size and could be a concern if the accelerating gap increases. However, assuming a 10cm gap and operating on 8th harmonic, both of which are unlikely for this work, the transit time factor reduces to .995; which is negligible.

Using the Empirical data from Kilpatrick represented in Equation 6.4, the maximum frequency can be presented as a function of gap size, g, and consider the effect of increasing frequency, shown by Equation 6.9

$$E_{kg}^3 \left[1 - \exp\left(\frac{835E_k}{gf^2}\right) \right] \exp\left(\frac{-17}{E_k}\right) = 180 \quad (6.9)$$

Using the solution for Equation 6.4 for E_k , the relationship for E_{kmax} the maximum

6. ACCELERATION STUDIES AND RF CHARACTERISATION

MV/m for a given frequency and gap size can be established. The frequency was interpreted as harmonics of the fundamental operating frequency and the gap size was iterated from 1cm to 8cm in increments of 1cm, calculating the maximum voltage that can be achieved before breakdown will occur. Figure 6.2 depicts the relationship between the maximum voltage per gap size achievable at different harmonics for the fundamental frequency of 10.0911MHz.

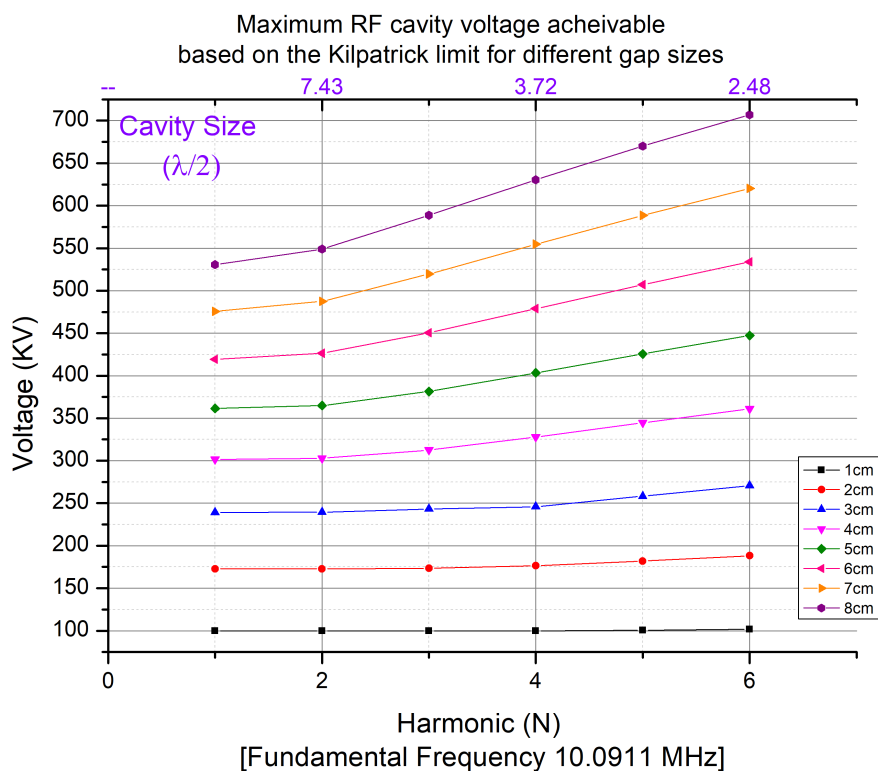


Figure 6.2: Maximum surface voltage achievable before breakdown occurs for different harmonics and accelerating gap sizes

It is important to note that the work of Kilpatrick was completed more than 50 years ago, and even then, it was noted that the Kilpatrick limit could be exceeded by a factor of 2 or 3 by carefully treating the surface of the material. This factor is now known as the bravery factor and will be ignored for the purposes of these simulations. Ignoring the bravery factor and being conservative is beneficial if the desired results can be achieved without these considerations. However, any increased voltage incurred by the bravery factor will improve energy gain per turn and orbit separation, which is only beneficial for the design.

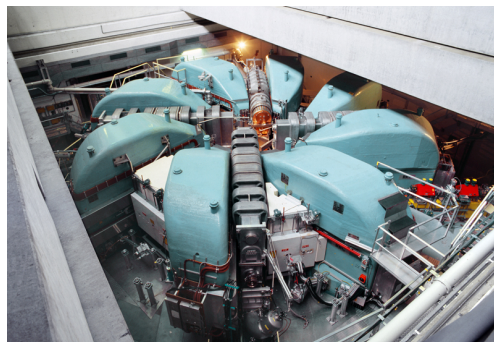
6.2.3 Current separate sector machines and their RF

Having discussed the theoretical limits proposed by the Kilpatrick limit, it is important to look at current working separate sector particle accelerators and identify what RF parameters have been achieved and whether they could be suitable for this design.

There are several renowned separate sector cyclotrons around the world at established facilities, the most recognised being at the Paul Scherrer Institut (PSI). As depicted in Figure 6.3 PSI houses two separate sector cyclotrons in one system; injector two and the ring cyclotron. The acceleration cycle begins from source to a Van der Graff electrostatic accelerator accelerating protons to 870 keV. The accelerated protons are then injected into injector 2, the first separate sector machine, and further accelerated to 72 MeV in 100 turns. The 72 MeV protons are then transferred to the ring cyclotron, the second separate sector machine, where the protons are further accelerated to 590 MeV before being extracted from the system [115] [116] [117].



(a) Injector 2 [118]



(b) The ring cyclotron [119]

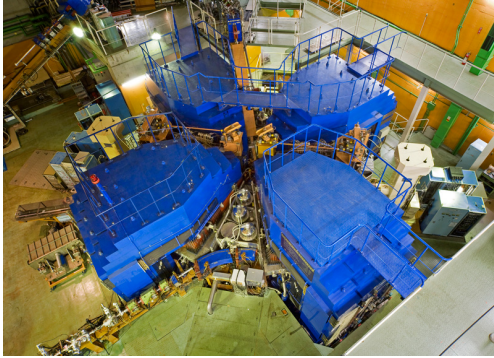
Figure 6.3: Separate sector cyclotrons at the Paul Scherrer Institut, Switzerland

Each separate sector stage in this system has its own RF system. Injector 2 accelerates protons using 2 delta type half wavelength double gap resonators with a gap width of 3.5cm and a gap voltage of 150 kV_p, operating at 10th Harmonic at 50 MHz. There have been recent upgrades to increase the beam current at PSI; which has resulted in additional cavities present in injector 2; the addition of 2 single gap half wavelength resonators. These additional cavities operate at identical parameters to the current resonators, but have an increased peak voltage of 400 kV_p. The RF system for the ring cyclotron operates at the same frequency, but single gap resonators are used instead of delta type cavities. The ring cyclotron cavities have recently been upgraded. Initially the RF voltage was set to 730 kV_p but the upgraded cavities achieve 1 MV. The gap

6. ACCELERATION STUDIES AND RF CHARACTERISATION

size cannot be found in the literature, but the cavity accelerating voltage is 8.8 MV/m and operates on 6th harmonic. Using the Kilpatrick limit, one could estimate the gap size to be around 10cm.

There are two established facilities in Japan that hold high energy ion separate sector accelerators, RIKEN and the Research Center for Nuclear Physics (RCNP). RIKEN is a large multidisciplinary research centre which holds 4 separate sector accelerators all connected to provide a multi stage accelerator for ions. The path of the particle through the machines depends on its mass, as there are different acceleration regimes for different ions. The four separate sector machines are identified as the RIKEN Ring Cyclotron (RRC) (depicted in Figure 6.4a), the fixed frequency ring cyclotron (FRC), the intermediate ring cyclotron (IRC) and the superconducting ring cyclotron (SRC) [120]. Irrespective of operating mode a summary of the RF for all the accelerators are taken from Sakamoto et. al [121] in Figure 6.4b.



(a) The RIKEN Ring Cyclotron (RRC), Japan [122]

item	RRC	FRC	IRC	SRC
freq. [MHz]	18~45	54.75	18~42	18~42
mode 1	$f_o^*(9^{**})$	-	$2f_o(7)$	$2f_o(6)$
mode 2	18.25(9)	54.75(12)	36.5(7)	36.5(6)
mode 3	$f_o(5)$	-	-	$f_o(5)$
# of cav.	2	2	2	4
# of gap	2	1	1	1
V_{gap} [kV]	300	500	650	650
$P_{\text{w.l.}}$ [kW]	150	100	150	150
FT cav.	none	1	1	1
Harmonics	-	3	3 or 4	3 or 4
$P_{\text{w.l.}}$ [kW]	-	20	20	60

*: f_o is a frequency of master oscillator.

** : (#) denotes a harmonic number $H=f_o t/f_{\text{beam revolution}}$

(b) A table detailing the RF systems for the different cyclotrons at RIKEN [121]

Figure 6.4: The RIKEN facility

There is a single separate sector accelerator at RCPN, the RCNP ring cyclotron. In this system, an AVF cyclotron injects particles into a ring cyclotron, reaching a final energy of 100 MeV/u . The separate sector design has 3 RF cavities, achieving a maximum acceleration voltage of 500 kV_p and operates at 6th and 10th harmonic.

All of the accelerators discussed thus far are specialist standalone accelerator facilities, however there are commercial proton therapy cyclotrons available. The most popular commercial cyclotrons available from Varian and IBA.

Varian provide the ProBeam, an isochronous separate spiral sector cyclotron. This machine accelerates protons to 250 MeV, using 4 half wavelength cavities [111]. These

cavities operate at 72.8 MHz running on the 2nd harmonic, with an accelerating voltage of 80 kV_p. The Varian Probeam cyclotron was chosen by both of the NHS facilities providing full energy proton beam therapy in the UK, as discussed in Chapter 1.

IBA currently provide proton therapy using their proteusOne solution, which accelerates particles using their superconducting synchrocyclotron (S2C2). Because it is a synchrocyclotron, it corrects for relativity by reducing the RF frequency, hence only pulse will be present within the cyclotron at any given time. As discussed in Chapter 3, the energy gain per turn is not a priority as the machine is not CW and the RF design is somewhat irrelevant to HEATHER. Nevertheless, for completion, the accelerating voltage is 3-12 kV_p operating at 1st harmonic.

It can be seen that the high energy separate sector accelerators use single gap cavities where the voltage across the gap typically ranges from 400-800 kV_p. Smaller machines used as a pre-accelerator in a chain typically use delta type half wavelength double gap resonator cavities, to achieve similar voltages, ranging from 100-300 kV_p.

6.3 HEATHER RF Studies

For Stage 1, two delta type half wavelength double gap resonators will be used, using a gap voltage of 300 kV_p. The feasibility of this design depends on using already existing technology, and a 300 kV_p has already been achieved using a delta type double gap resonator and single gap resonators. The RIKEN cyclotron uses delta type double gap resonator at a slightly lower frequency of 45MHz for the desired gap voltage and the single gap resonators used at PSI achieve 850 kV_p operating at 50MHz; 300 kV_p should be realistically achievable.

To achieve 300 kV_p, the gap size needs to be at least 4cm based on the Kilpatrick criterion. The Kilpatrick limit does not have any restrictions on frequency necessary to achieve 300 kV_p, but the cavity size is dependent on frequency. To achieve a realistic cavity size (in terms of civil engineering) the cavity needs to be less than 3m, hence the 5th harmonic should be the minimum used, if achievable by the machine.

For stage 2, single gap resonators will be used as in all high energy cyclotrons, such as PSI. The cavities used at PSI are a great example of what could be used, but to be conservative, 500 kV_p will be used as opposed to 850 kV_p.

6.3.1 HEATHER RF operating frequency selection

Before optimising the cavities for each stage, a single operating frequency needs to be established across both stages. For stage 1 two simple uniform single gap RF cavities

6. ACCELERATION STUDIES AND RF CHARACTERISATION

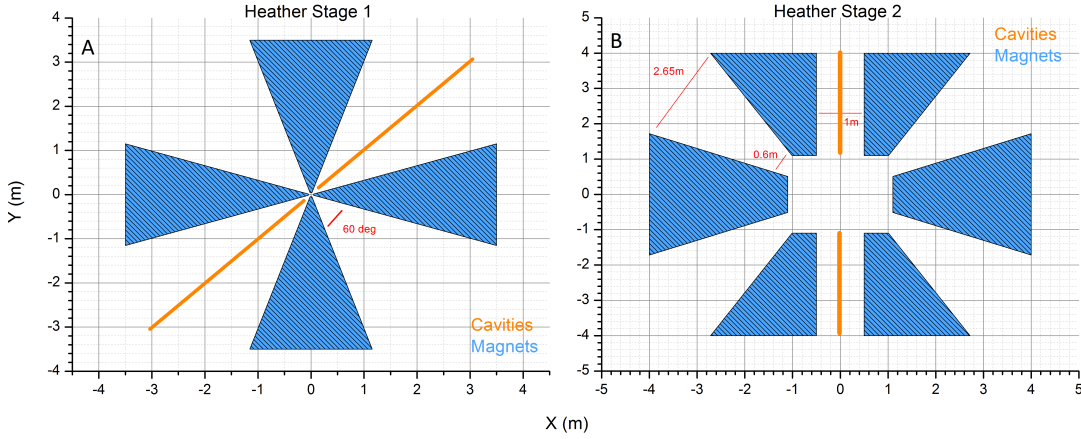


Figure 6.5: Highlighted magnet and cavity dimensions for stage 1 and stage 2 of HEATHER

with a width of 1cm were added 180° apart; at 45° and 225° in between the magnet gaps as depicted in Figure 6.5. The accelerating voltage across the gap is uniform radially with a voltage of 300 kV_p . For stage 2, identical RF accelerating gaps are inserted into the straight sections; but with an increased accelerating gap voltage of 500 kV_p . The positioning of the cavities for stage 2 is depicted in Figure 6.5 contradicting the initial purpose of the straights: to aid injection and extraction. This is because at the outer orbit the distance between the sector magnets is greater than the 1m straight allowing more room to extract, as depicted in Figure 6.5, and it makes the optics more symmetrical.

Using the mean synchronous frequency for each stage as a starting point, the operational fixed RF frequency was identified. A single fully stripped He^{2+} particle was accelerated from 1 MeV to 400 MeV for stage 1 and from 400 MeV to 900 MeV for stage 2. The total phase slip across the accelerating regime for different frequencies was calculated to identify the ideal operating frequency for each stage. Because neither stage is perfectly isochronous a phase slip will occur. Minimising the phase slip allows for maximum kinetic energy to be transferred across the whole acceleration regime; reducing the beam time in the machine and the risk of losses. Figure 6.12 shows the particle phase acceptance during acceleration for both stages, and Figure 6.6 shows the calculated phase slip from the shown frequencies and compared for both stages. The optimal fixed RF cavity frequency for stage 1 and stage 2 were found to be 10.0911 and 10.0919 MHz respectively. This is different to the mean synchronous

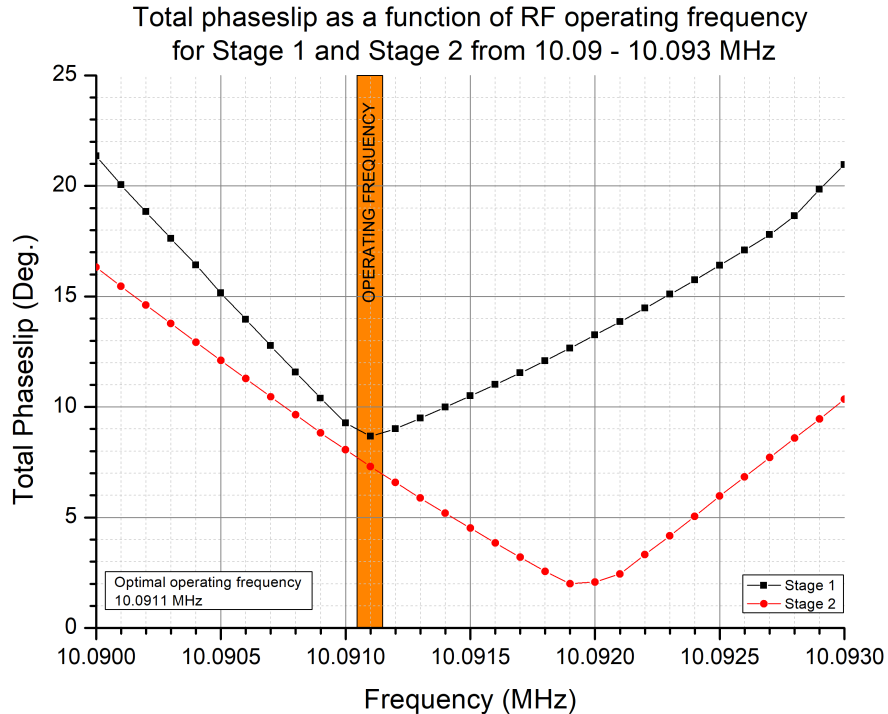


Figure 6.6: The largest phase slip measured across the acceleration regime for different RF frequencies for stage 1 and stage 2

frequency as predicted because the energy gain relative to the beam energy is much greater at lower energies, and the phase slip can be overcome at a faster rate. This is especially important for stage 1, where the fringe fields overlap and the vertical tune is suppressed at low energies, causing an integer resonance crossing. Using a 300 kV_p voltage per gap for stage 1 translates to a 2.4 MeV peak energy gain per turn. The vertical tune suppression is overcome at around 20 MeV , as depicted in Figure 5.10, where the energy gain at this point is greater than 10% per turn. As demonstrated with EMMA [98], crossing the integer fast enough is not detrimental to the beam, which is also demonstrated here. Stage 2 has two single gap resonant cavities and gains 2 MeV per turn. It crosses a 2nd order resonance initially, which may be an issue, due to the relative energy gain comparative to the initial crossings with stage 1.

To operate at the same fixed frequency across both stages, a compromise must be made between the two machines, as they both have different optimal RF frequencies. From the range of frequencies simulated the optimum operating frequency for both

6. ACCELERATION STUDIES AND RF CHARACTERISATION

machines was found to be that of stage 1, 10.0911MHz. When comparing the two stages, stage 2 is more isochronous, and less effected by a phase slip than stage 1. This can be observed in Figure 6.6. Because stage 2 is more isochronous it is possible to use an RF frequency optimal for stage 1, and in this case, achieve a smaller total phase slip for stage 2.

6.3.2 Optimisation of the acceleration orbit

The ideal acceleration orbit or beam centroid is a reference orbit which perturbations can be compared against. The ideal orbit chosen for these machines is where the orbit separation between two sequential orbits are as equidistant as possible, also known as centering. As well as frequency and phase slip as discussed, the orbit radius, angular momentum, injection angle, and starting phase are variables that effect the ideal acceleration orbit. The radius and angular momentum are important factors controlling the orbit direction, as adjusted and discussed in the previous Chapter. These parameters are iterated, and the orbit assessed to identify the ideal orbit. Because of the initial time of flight variation for stage 1, it is important to accelerate immediately after injection to pass this region rapidly and minimise beam growth and losses. Ideally injection would be a few cm from the cavity but this is not realistically feasible. Considering space may be necessary for injection, the particle injection angle is set to 30° , just before the cavity and halfway between the cavity and physical magnet edge. A visualisation of the injection angle is shown in Figure 6.7

Stage 2 has much more space, and for the purposes of optimisation the beam was injected directly 25cm away horizontally from the cavity. Because this design is a racetrack, trigonometry was then used to identify the radius and angle when simulating. In separate sector designs, the particle is not injected at the cavity; but in a valley. Its starting phase is therefore important so when it meets the cavity it arrives with the same phase as the cavity. Arriving early or late will induce a phase slip, as discussed already in this thesis.

The particle radius and angular momentum were iterated in OPAL to find the stable equilibrium orbit. Figures 6.8a, 6.9a, 6.10 and 6.11 details parameters from the initial unoptimised particle radius and angular momentum. The initial starting radius was identified from the stable equilibrium orbits for 1 MeV, 945mm, from Chapter 5, and the initial angular momentum was set to $0\beta\gamma$.

By iterating the starting phase, Equation 3.3 can be used to identify the starting phases that reach the design energy which is known as the phase acceptance. A closer

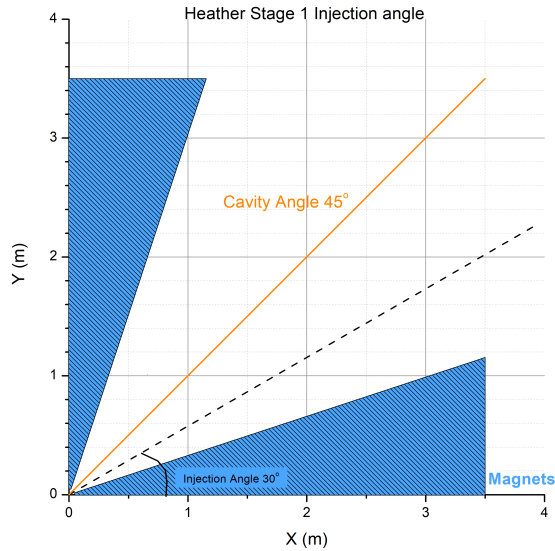
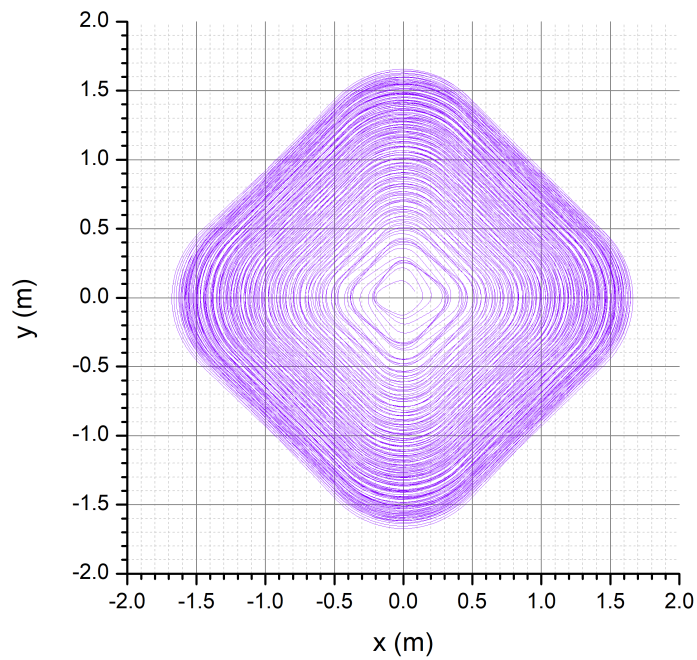


Figure 6.7: A depiction of a quadrant of stage 1, The injection angle is highlighted.

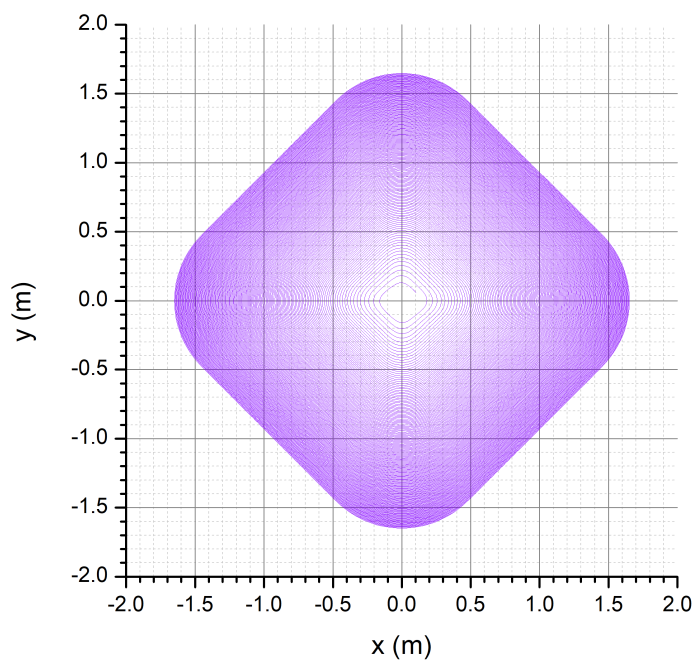
representation of phase acceptance can be attained by fitting an Equation to the ToF curve for each stage to get a more accurate representation of the particle phase as a function of energy. The improvement of the phase slip for stage 1 can be seen in Figure 6.10.

Post optimisation the orbit separation is much more uniform and the beam is well centered around the machine as observed in Figures 6.8b, 6.9b, 6.10 and 6.11. The orbit separation observed is 2.5mm, which will be important when discussing extraction later in this thesis. The phase acceptance for stage 1 and 2 are shown in Figure 6.12; for the parameters used to find the optimal frequency.

6. ACCELERATION STUDIES AND RF CHARACTERISATION

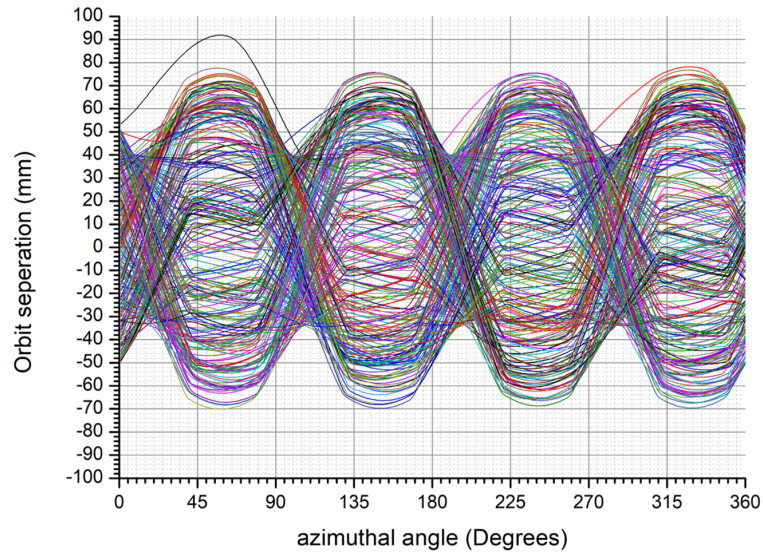


(a) Pre-optimisation

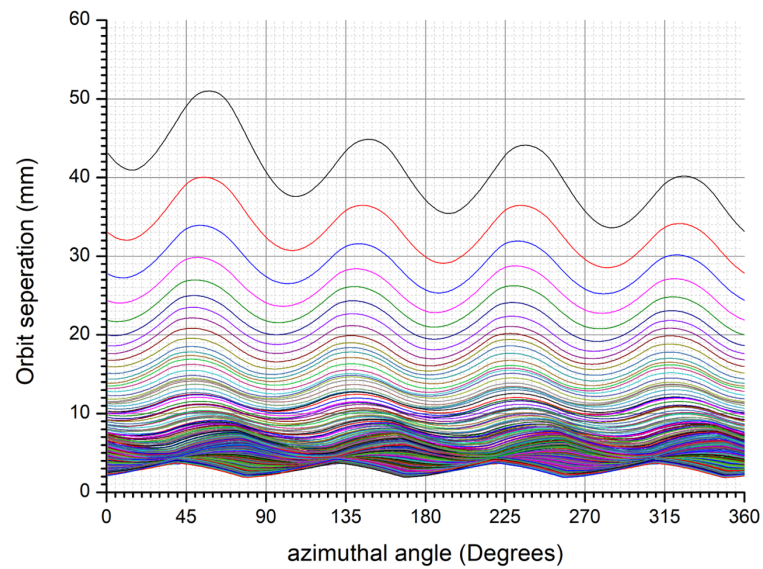


(b) optimised

Figure 6.8: The beam acceleration path before and after optimisation of the injection parameters



(a) Pre-optimisation



(b) optimised

Figure 6.9: The difference in mm between successive orbits before and after optimisation of the injection parameters

6. ACCELERATION STUDIES AND RF CHARACTERISATION

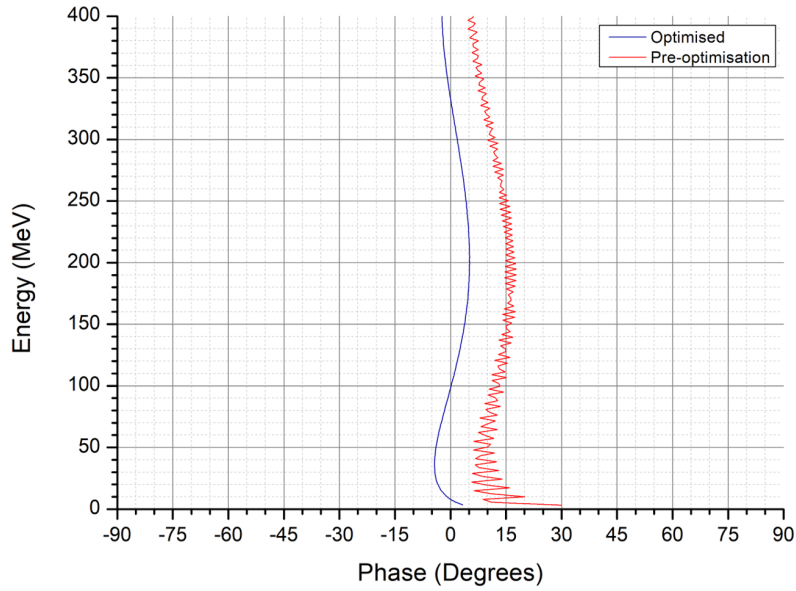


Figure 6.10: the phase of the particle relative to the RF phase before and after optimisation

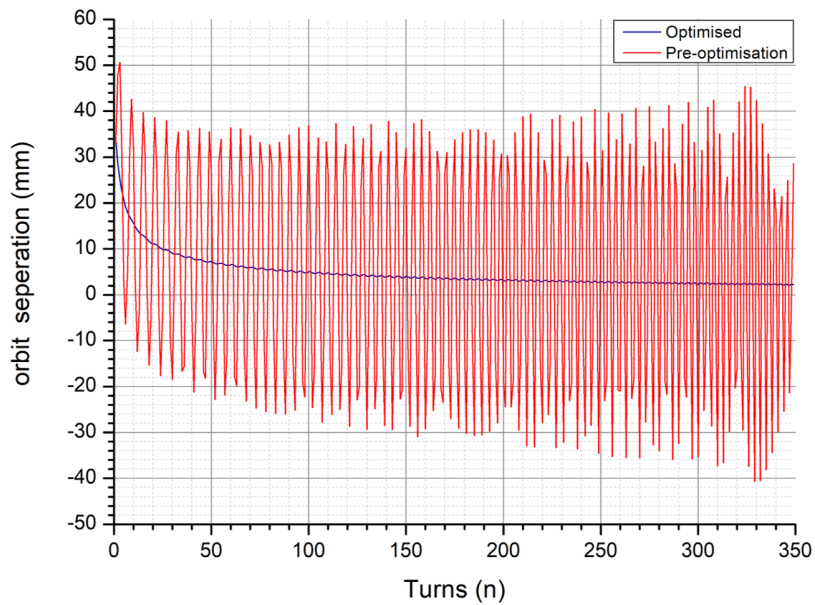
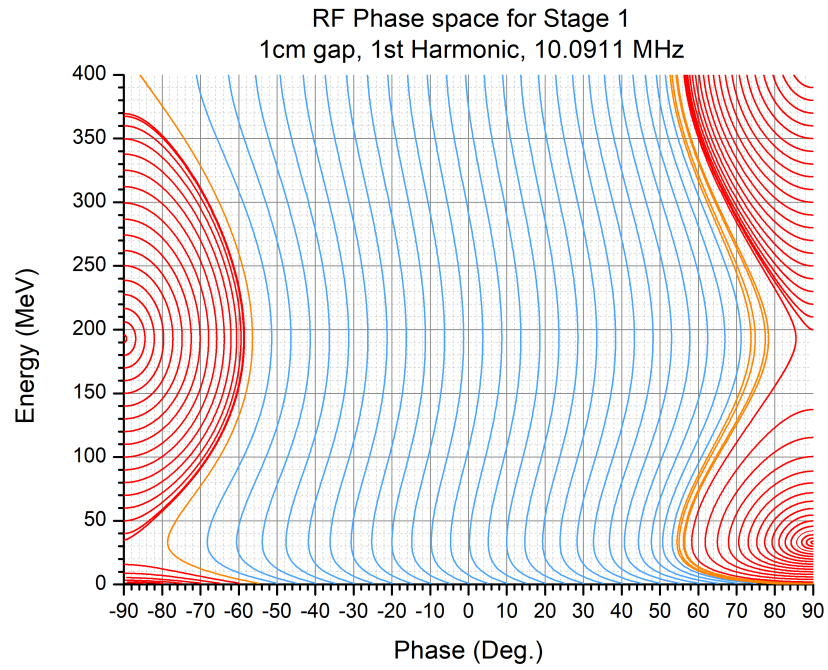
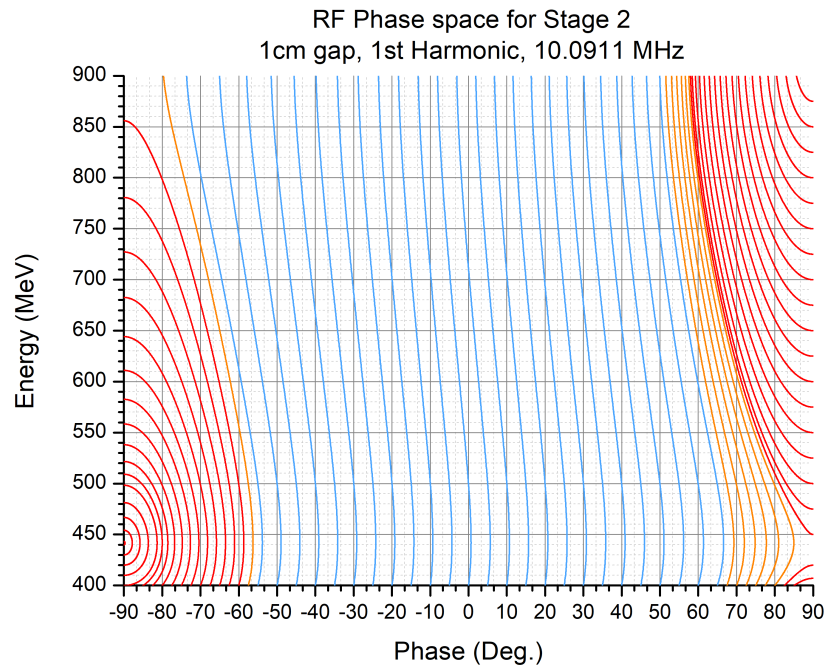


Figure 6.11: A comparison separation between orbits for a given point at 45° degrees before and after optimisation



(a) Stage 1



(b) Stage 2

Figure 6.12: HEATHER RF phase space plots showing the phase acceptance

6.4 Realistic RF acceleration

For stage 1, a single gap cavity could be used, and single gaps were used to find the optimal operating frequency. Delta type double gap resonators may be better suited as they are typically used in first stage accelerators, such as in the RIKEN cyclotrons discussed above. The delta type resonator configuration is depicted in Figure 6.13. The idea of this thesis is to investigate the feasibility of this accelerator, so for stage 1 both a $\lambda/2$ delta type double gap resonator and a single gap resonator will be simulated. The single gap cavities will be situated at 45° in the middle of a valley as shown in Figure 6.5. In OPAL there is no configuration for delta type resonator, so two single gap cavities were inserted 40 degrees apart. To achieve the 300 kV_p, following the Kilpatrick criterion, 4cm gaps will be used.

Using delta type double gap resonators, the energy gained per turn increases by a factor of 2 because the number of accelerating gaps has doubled. Consequently, there is an additional efficiency factor that is not considered in OPAL for delta type resonator and two adjacent single gap cavities are used. This factor depends on the angle between the cavities and harmonic used and is a further addition to Equation 6.1. Equation 6.10 gives the energy gained per turn using delta type double gap resonators

$$E_t = 4qV_0 \sin\left(\frac{h\theta}{2}\right) \cos(\phi) \quad (6.10)$$

Where h is the harmonic and θ is equal to the angle between the cavities. The $\sin(\frac{h\theta}{2})$ term can be interpreted as an efficiency factor and this is shown Table 6.1 for varying harmonics. As discussed earlier in Section 6.3, the 5th harmonic is the preferred option, but this still needs to be verified. Operating at 5th harmonic correlates an efficiency factor of 0.98, which is a voltage loss of 24 keV per turn, which is negligible.

Harmonic	1	2	3	4	5	6	7	8
$\sin\left(\frac{h\theta}{2}\right)$	0.34	0.64	0.87	0.98	0.98	0.87	0.64	0.64

Table 6.1: Efficiency factor for varying harmonics for the delta type resonator angle of 40°

Using OPAL, single gap and double gap cavities were simulated for both 200 and 300 kV_p per accelerating gap. Lower voltages and single cap cavities are also simulated to identify more probable alternatives if the desired RF design option cannot be achieved when designed. A uniform voltage across the gap radially was used so the voltage gain

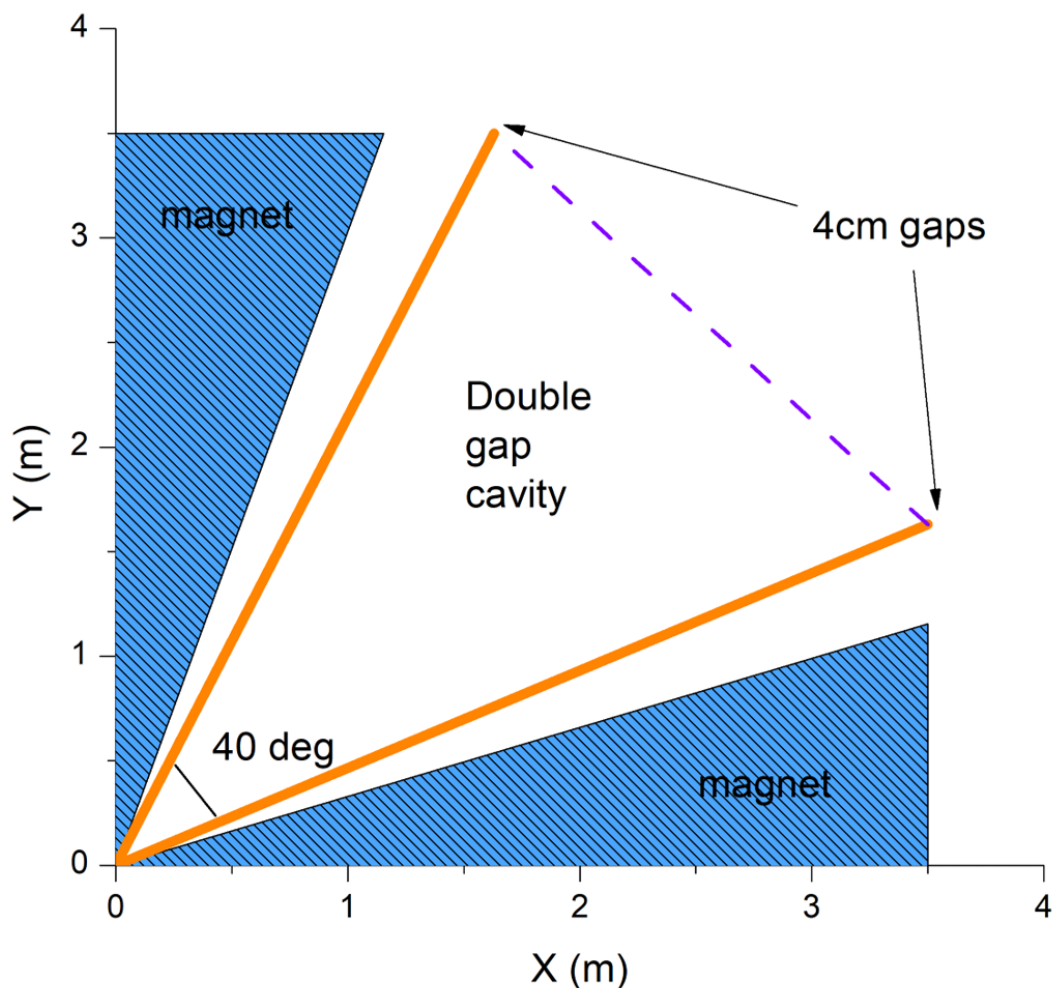


Figure 6.13: The configuration of the delta type double gap $\lambda/2$ resonator simulated in OPAL

per turn is the same for the purposes of this study. As delta type resonators are not present in the OPAL code, the harmonics 1 and 2 for delta type resonator are ignored. OPAL does account for the transit time factor, and this is done in all the simulations. As discussed previously in 5.2.2, a 40° phase slip is the total phase slip tolerance before beam quality begins to deteriorate. Figure 6.14 shows the total phase slip of a single particle following the ideal acceleration equilibrium orbit for the different cavity configurations.

The single gap cavities are not as effective as the double gap cavities and neither single gap design can operate at 5th harmonic within the phase slip constraint. How-

6. ACCELERATION STUDIES AND RF CHARACTERISATION

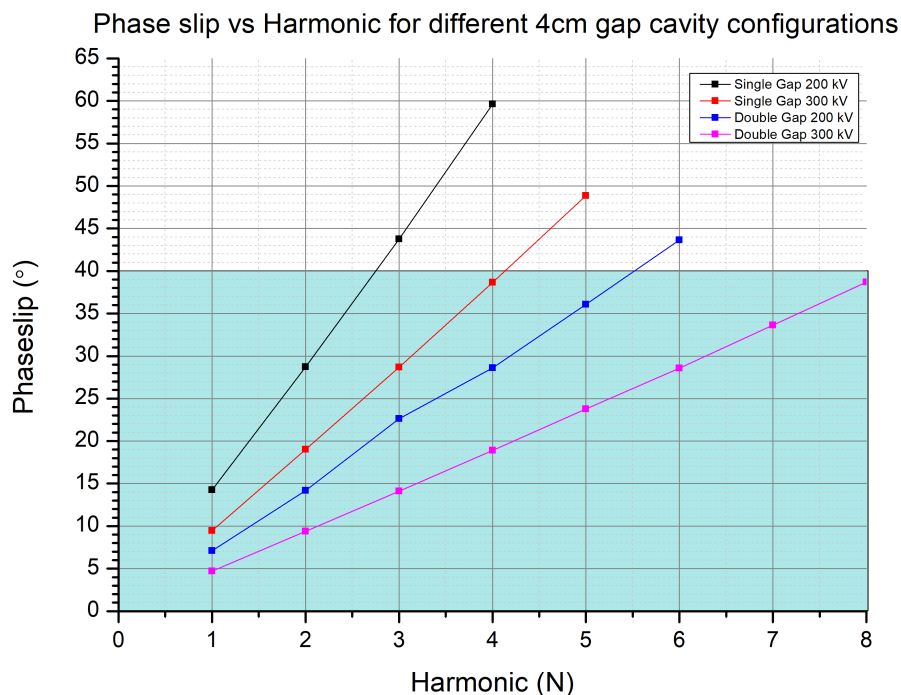


Figure 6.14: The configuration of the delta type double gap $\lambda/2$ resonator simulated in OPAL

ever, it is identified that a single gap resonant cavity operating with an accelerating voltage of 200 kV_p would be the only option completely unsuitable for this design, as the largest harmonic achievable within the phase slip constraint is the 2nd harmonic, translating to an unrealistic cavity size of approximately 7.5m. A 300 kV_p accelerating voltage single gap resonator could be achievable and allow operation at 4th harmonic, significantly reducing the cavity size to an achievable 3.75m. A cavity height of 3.57m is large and slightly out of scope, but cavities of this magnitude have been constructed before, and may be a compromise to be considered if the preferred designs are not achievable from a full detailed RF design.

The desired double gap cavity design of 300 kV_p fits within the design criteria, and a cavity of similar design has already physically been constructed and will have the RF parameters used for stage 1. If the preferred RF system is not achievable, the more conservative delta type resonator design with a 200 kV_p gap voltage is still an acceptable alternative, with a compromise of a larger phase slip. Figure 6.15 shows the

particle phase as a function of energy across the accelerating regime. Each line on the graph shows a particle with a different starting phase, which was iterated from -90° to 90° in 5° increments. For all of the phase space plots the blue lines represent successful acceleration to the design energy, the red lines show unsuccessful acceleration to the design energy and the orange lines suggest the boundaries of starting phase likely to reach the design energy. The range of starting phases that accelerate the particle to the desired energy is known as the phase acceptance. The phase acceptance for these designs have been investigated and found to be 85 and 70 degrees for 300 kV_p and 200 kV_p accelerating voltage respectively,

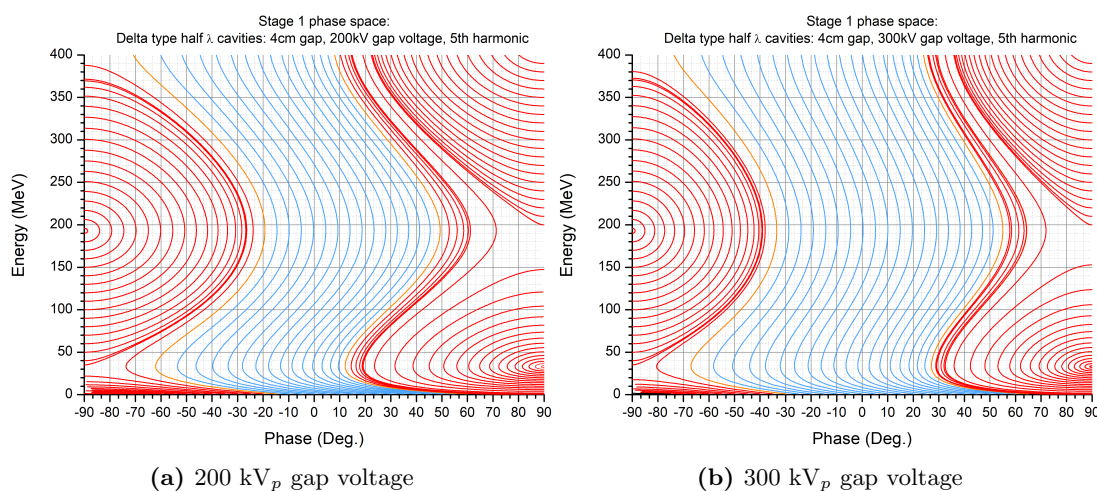


Figure 6.15: HEATHER stage 1 RF phase space plots for delta type double gap resonators with different accelerating gap voltages

6.5 Stage 2 RF

To keep the operating frequency of the cavities identical throughout the entire accelerating regime, 5th harmonic will be used for stage 2. As discussed, single gap cavities will be used, operating at 500 kV_p per cavity gap. Two 8cm single gap cavities were simulated in OPAL operating at 5th harmonic positioned as shown in Figure 6.16a. Figure 6.16a shows the particle phase as a function of energy across the accelerating regime. The phase acceptance for stage two was found to be $\sim 80^\circ$ across the entire acceleration regime, and the total phase slip approximately 36° . To reduce the phase slip, A higher accelerating voltage could be used across the cavity gap. An increased accelerating gap voltage of 600 kV_p was simulated to assess phase slip, which was found

6. ACCELERATION STUDIES AND RF CHARACTERISATION

to be an improved 30° , with a slightly increased phase acceptance of 90° as depicted in 6.16b.

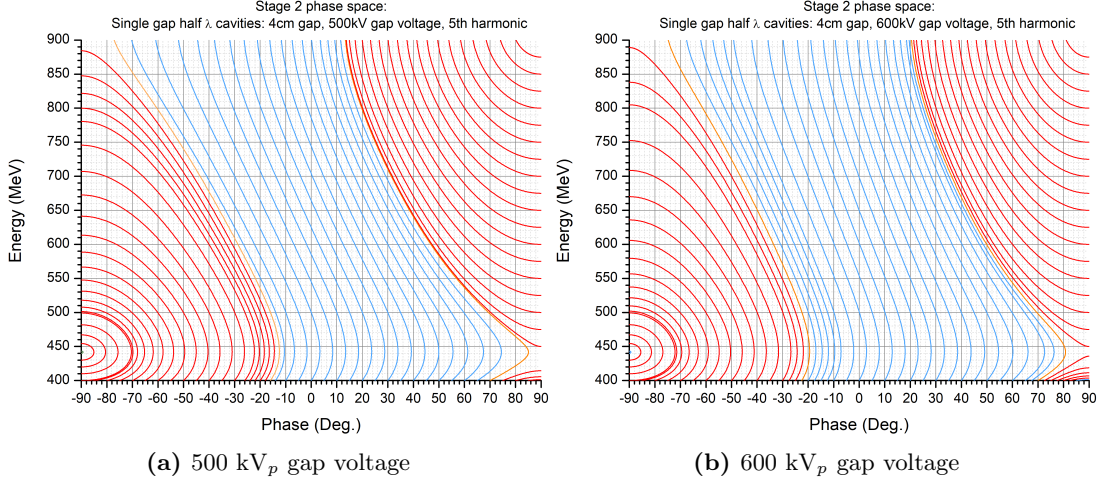


Figure 6.16: HEATHER stage 2 RF phase space plots for single type double gap resonators with different accelerating gap voltages

There is scope to use an 8cm gap to increase the accelerating voltage beyond 600 kV_p without reaching breakdown. However, the design is conservative, the 500 kV_p design discussed here will be used to accelerate particles in stage 2 from this point on in this thesis.

6.6 Chapter Summary

In this chapter an optimal fixed RF operating frequency has been established for the entire accelerating regime across both stages of the accelerator design. A full detailed RF design is beyond the scope of this thesis, but a realistic approach to selecting parameters to simulate has been discussed and compared to current RF systems in similar machines. The parameter selection addresses issues such as RF breakdown, cavity height, operating harmonic number and accelerating gap size. The stage 1 RF system has been chosen to be two half wavelength double gap delta type resonator, with a gap voltage of 300 kV_p , and stage 2 to be single gap RF cavities, with an accelerating voltage of 500 kV_p .

7

Beam Acceleration and Extraction Studies

In the previous chapter the RF parameters for each stage of HEATHER were discussed, the ideal particle was accelerated through both stages and different realistic cavity parameters were identified. Having identified optimal RF parameters and accelerating an ideal particle through both stages, this chapter looks at accelerating a beam through each stage of the accelerator with realistic emittances based on similar machines. Different emittances are optimised for acceleration through stage 1, and the changes in emittance discussed. Extraction from stage 1 is discussed and the injection parameters are optimised to maximise orbit separation. The extracted beam from stage 1 is then injected into stage 2, and, as for stage 1, the emittance across the accelerating regime is discussed. The injection parameters are then also optimised for stage 2 to identify the maximum orbit separation achievable at extraction without making changes to the magnetic field.

7.1 Pre-acceleration

The initial starting design energy for stage 1 will require pre-acceleration. The different types of accelerators that could be used have all been described in 3.1. For HEATHER, electrostatic acceleration is the most realistic option for pre-acceleration and the voltages required to accelerate He^{2+} to 1 MeV are achievable and not technologically limiting. Electrostatic acceleration is used to pre-accelerate at many established functioning facilities, including many of those discussed in Chapter 6: RIKEN [123] [124], PSI [112] [125], TRIUMF [126]. Other accelerators, such as a cyclotron, could be used

7. BEAM ACCELERATION AND EXTRACTION STUDIES

to pre-accelerate and potentially allow higher energy injection where more space is available, however the cost implications of this deem this inefficient. It is quite clear that an electrostatic accelerator to reach 1 MeV is the most reasonable option, however its footprint may be large and may be an issue. The cost, footprint and type of accelerator for pre-acceleration need to be investigated beyond this thesis.

7.2 Emittance

A beam can be described in 6 dimensions by its angle and position in each of the 3 orthogonal planes; x, y, z . The size of a charge particle beam in phase space is typically enclosed in an ellipse and called its emittance. Phase space describes an ensemble of particles by their position and angle. The general expression for the emittance is expressed by Equation 7.1.

$$\epsilon_w = \frac{A_{ww'}}{\pi} \quad w = x, y, z \quad (7.1)$$

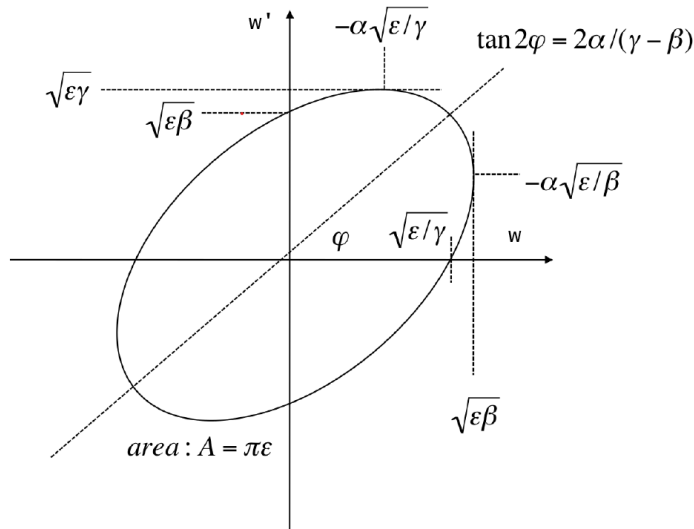


Figure 7.1: Depiction of emittance, adapted from [127]

Where $A_{ww'}$ is the area of the beam ellipse with beam width w , measured in mm and beam angle w' measured in mrad.

Without acceleration along a beam line the emittance remains invariant; its aspect ratio or orientation may change but its value is constant. Because the emittance is

invariant it can be related to the lattice, and using Equation 7.2 calculated using the Twiss parameters; α , β and γ

$$\epsilon = \gamma w^2 + 2\alpha w w' + \beta w'^2 \quad w = x, y, z \quad (7.2)$$

There are many different variations for the emittance, and in this thesis the RMS emittance will be used, described by Equation 7.3, and depicted in Figure 7.1 RMS is an abbreviation for root mean squared, and is a statistical way of achieving a magnitude value of the average in a system that includes negative numbers

$$\epsilon_{w_{RMS}} = \sqrt{\langle w^2 \rangle \langle w'^2 \rangle - \langle w w' \rangle^2} \quad w = x, y, z \quad (7.3)$$

In accelerators normalised emittance may be used, which can be calculated using equation 7.4. Under acceleration transverse momentum is conserved, but the longitudinal momentum is increasing, reducing the angle in the longitudinal plane and reducing the emittance. The reduction in emittance when accelerating a beam is called adiabatic damping. During acceleration the normalised emittance is conserved.

$$\epsilon_{normalised} = \beta \gamma \epsilon_w \quad (7.4)$$

7.3 Stage 1 Beam Acceleration

The beam emittance is constant in a non-accelerating system, but the emittance oscillates as the beam propagates around the machine. If the injected beam envelope does not match that of the accelerator at injection, particle oscillations will occur and cause emittance growth. The larger beam caused by emittance growth then makes the beam more susceptible to resonances; hence reducing beam quality and complicating extraction.

Without a full injection and pre-acceleration design, the exact beam emittance that will be injected into the accelerator is unknown. Instead, the emittances used are based on typical injected beams into similar particle accelerators, from standard particle sources. These will give a good indication of what is possible and allow the identification of what beam size it is possible to accelerate.

A range of 1, 2 and 5 π mmrad emittances in all planes were injected into stage 1, using a Gaussian distribution generated within OPAL to create the beam. As discussed in Chapter 5, the co-ordinate system for OPAL, y is the longitudinal direction, x the radial direction and z the vertical direction. The parameters necessary to generate a

7. BEAM ACCELERATION AND EXTRACTION STUDIES

beam in OPAL are the RMS beam width and RMS angle.

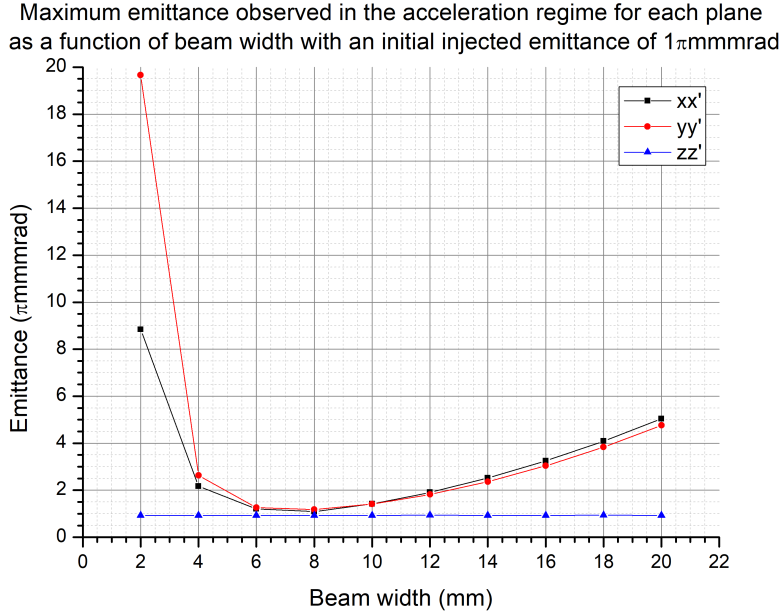


Figure 7.2: The maximum emittance observed in each plane as a function of beam width using the same initial injected emittance of $1\pi\text{mmrad}$ simulated in OPAL

To find the optimal injected emittance orientation, the emittance is kept constant and the beam width and angles need to be changed. A range of beam widths were iterated, and their corresponding angles are calculated for a fixed emittance. All planes were iterated simultaneously as demonstrated by Figure 7.2 showing the maximum emittance across the acceleration regime as a function of beam width of the injected beam. Figure 7.3 shows the emittance profile in which the least growth was observed in each plane from an initial injected beam with an emittance of $1\pi\text{mmrad}$.

The initial radius and angular momentum values used were the same for the single particle RF studies and will need to be corrected for a beam. Incorrect centering is just as detrimental to a mismatched beam and can lead to unwanted emittance growth and hence reduced beam quality. The radius and angular momentum of the beam was optimised as described in previous chapters. The entire process was repeated again for 2 and 5 πmmrad and Figures 7.4a to 7.4c show the final optimised emittances for all 3 initial emittances. It can be seen that there is some growth in the horizontal and longitudinal planes peaking at around 65 MeV. Some growth was anticipated as this is the closest working point on the tune map to the 2nd order resonance line

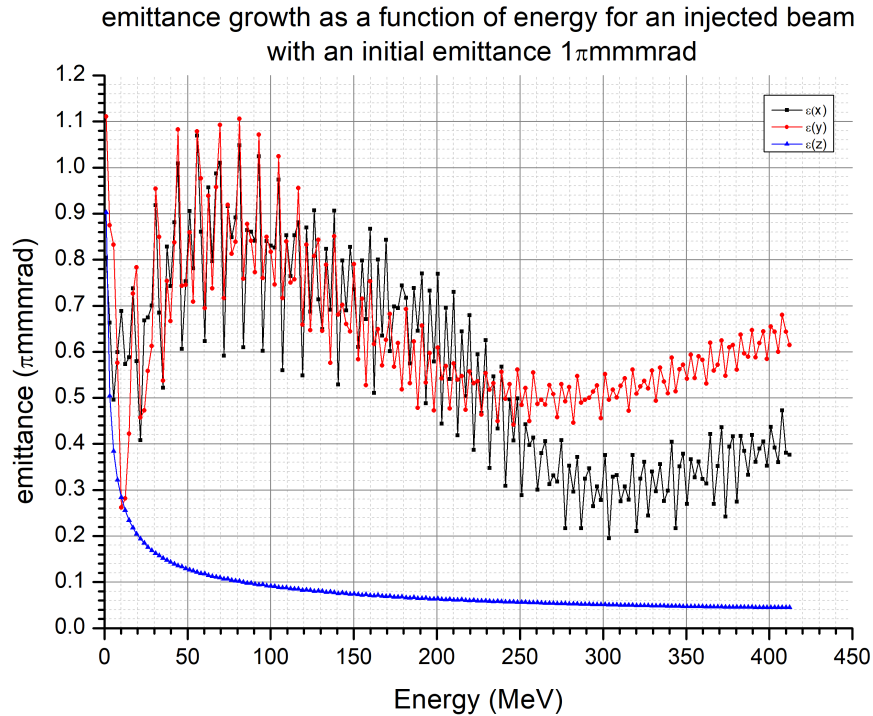
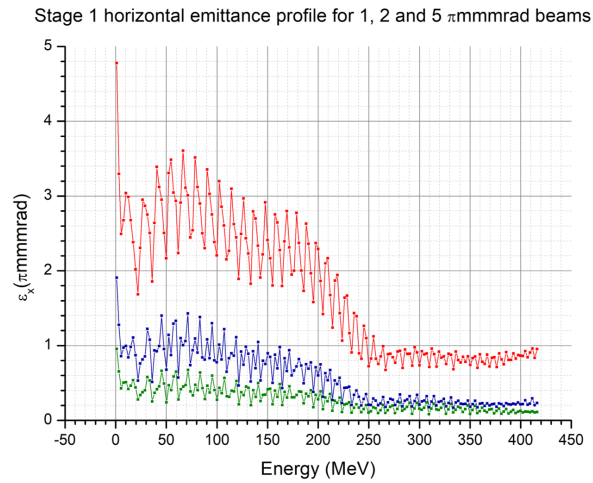


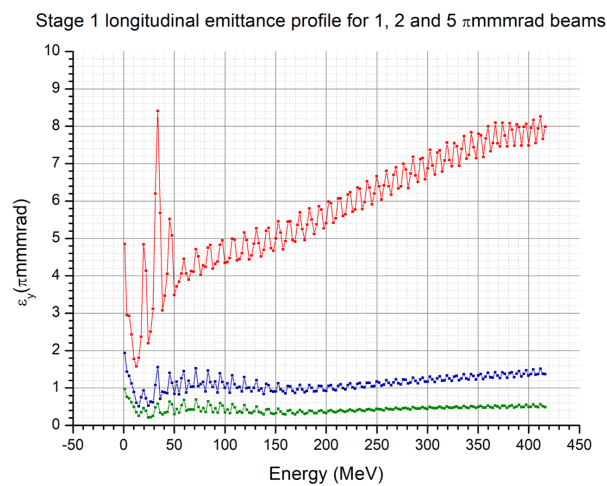
Figure 7.3: The optimised emittance as a function of energy for each plane from an initial injected emittance of 1π mmrad in each plane simulated in OPAL

(Figure 5.10). There appears to be no growth caused by the integer resonance crossing approximately around 5 MeV as seen on Figure 7.3. The integer resonance crossing is passed quickly over one turn and does not have enough time to effect the beam. The growth that does occur is present for many turns, effecting the beam and visually seen. As the injected emittance increases, the same relative emittance growth is observed, except longitudinally, where the emittance growth is much larger for 5π mmrad. This suggests that at a largest beam size the beam is much closer to the 2nd order resonance line.

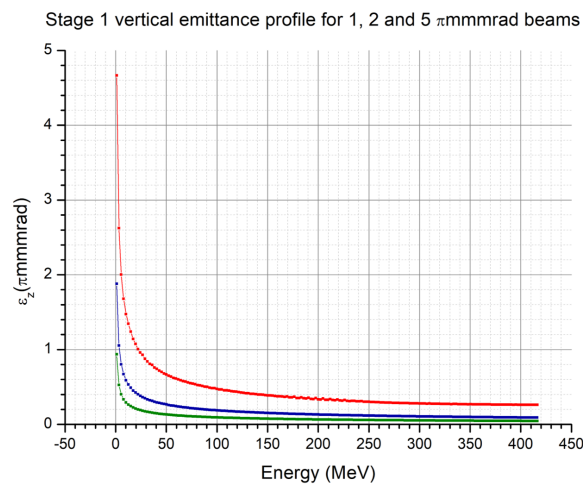
7. BEAM ACCELERATION AND EXTRACTION STUDIES



(a) Optimised $\mathcal{E}(x)$ for injected emittances 1,2 and 5 π mmrad simulated in OPAL



(b) Optimised $\mathcal{E}(y)$ for injected emittances 1,2 and 5 π mmrad simulated in OPAL



(c) Optimised $\mathcal{E}(z)$ for injected emittances 1,2 and 5 π mmrad simulated in OPAL

Figure 7.4: Stage 1 emittance profile for different initial injected emittances

7.4 Cyclotron Extraction

Once accelerated to the desired energy the beam needs to be extracted and removed from the accelerator. In one method for doing this the beam of particles passes in between a thin metallic plate, known as a septum, and an electrode. Creating an electric field between the septum and the electrode, the particles receive a kick and are steered off orbit and directed in between the electrode and septum where they are extracted from the machine, as shown in Figure 7.5 [128].

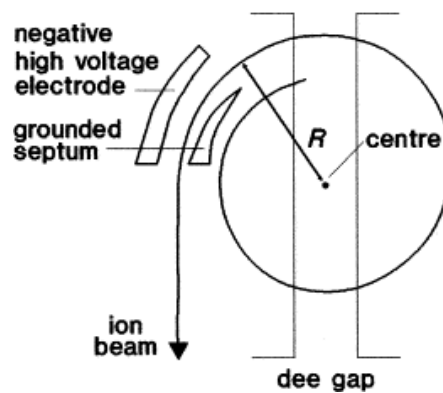


Figure 7.5: A depiction of cyclotron extraction by use of a septum, taken from [128]

As the energy of the particles increases, the radial separation between successive orbits reduces, which can be identified from Equation 3.9. Eventually in any cyclotron the orbits will begin to overlap, and multi-turn extraction may occur, changing the energy spread of the beam and causing losses on the septum. Losses on the septum can lead to further unwanted issues such as activation; creating unwanted secondaries. Activation and unwanted secondaries have the potential to increase the amount shielding required, but more importantly, the potential to harm from highly ionising radiation if maintenance is essential for function. Turn separation needs to be maximised to increase the probability that only the desired orbit is extracted. The necessary size needs to be enough to accommodate a septum for electrostatic extraction. Initial septum thicknesses have been found to be between $50\mu\text{m}$ and $250\mu\text{m}$. It is important to note the septum thicknesses quoted are for the thicknesses at the start of the septum as they typically increase in size radially, where the thickness can increase into several mm. To be conservative, the minimum orbit separation necessary should be 0.5mm . [129] [130] [131] [132] [133].

In cyclotrons the easiest way to increase turn separation is to increase the energy

7. BEAM ACCELERATION AND EXTRACTION STUDIES

gain per turn which can be done in either 2 ways; increasing the RF voltage or by increasing the number of cavities. For higher energy machines, the RF design may already be at the boundary of what is possible, and different ways of increasing orbit separation may be necessary by altering the magnetic field at the extraction radius [134].

Resonant extraction utilises betatron oscillations to separate successive orbits and can be done via brute force or processional. Brute force is the addition of coils to the magnets to create field bumps and pushes the beam onto a resonance. Processional resonant extraction is where the beam crosses a resonance and the betatron oscillations gradually increase around the equilibrium orbit and increase turn separation. As a result it crosses the resonance, changing the working point, affecting the particles path length and hence its frequency. The change in frequency between the two orbits crossing the resonance will induce a phase slip and additionally increase the turn separation [134].

Another method of extraction which is unsuitable for He^{2+} , but is still mentioned for completion, is stripping extraction. In this extraction method the beam is a negative ion and when the desired energy is reached the beam passes through a stripping foil, usually made of carbon, and the ions are stripped of electrons. This reverses the charge on the ion, and opportunely the magnets force on the particle is now reversed. Where the negative ion was processing around the machine the particle is steered away by cyclotron magnets, and down a beam line to be extracted [134].

7.5 Stage 1 Extraction

After optimising the beam and reducing the emittance growth by matching, the beam orbit separation at extraction needs to be investigated. To assess the orbit separation at extraction in more detail, the last 5 orbits were investigated at the middle of a valley, where the beam would be extracted. To assess the last 5 orbits, a radial probe was inserted at 45° and the particles radial position when crossing is recorded. The radial positions of the particle were then binned, using a bin size of 0.2mm. Current optimisation of the stable acceleration orbit focuses on as close to equidistant orbit separation as possible, as described and demonstrated in Chapter 5. By not achieving equidistant orbit separation, the orbit separation distance oscillates throughout acceleration, and on sequential orbits the bunches get closer or further away. This is known as orbit bunching. Orbit bunching could be used to increase the orbit separation at extraction. Bunching orbits closer together may allow latter orbits to spread out, achieved

by changing the injected beam radius and angular momentum.

The ideal acceleration orbit identified in Figure 7.6b shows peak to peak orbit separation at extraction for stage 1 to be $\sim 2.5\text{mm}$. For a beam this distance is expected to reduce, with increasing beam size, and there is the potential to overlap. The injection parameters found for the ideal orbit separation for a single particle were used when injecting a beam for three different studied emittances, 1, 2 and $5 \pi\text{mmrad}$, shown in Figure 7.6a. For the ideal particle the orbit separation in mm was peak to peak, however for the injected beams the orbit separation shown is between the largest radial particle and the closest radial particle between successive turns. The injection parameters were then optimised to better suit the separation between orbits for beams as opposed to a single particle, as shown in Figure 7.6b.

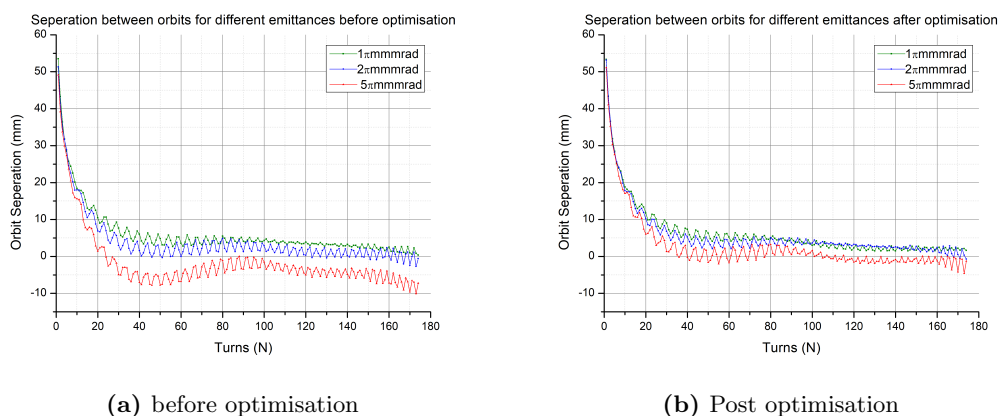


Figure 7.6: Radial successive orbit separation per turn for different injected beam sizes

From Figure 7.6 It can be seen that after optimising the injection parameters for the studied emittances, the orbit separation is much improved for all injected beam sizes. For the 1 and 2 πmmrad cases, there is no particle overlap throughout the entire acceleration regime, however overlap is observed after the first 100 turns for the injected 5 πmmrad . Looking in detail at the extraction orbits, the peak to peak distance and the 2σ distances between successive orbits were identified. As the distribution is Gaussian, there will typically be a tail of particles which extend beyond the majority of the particles. The 2σ boundaries will identify regions where 95% of the particles will be confined. The extraction orbit was identified as the first orbit with a peak energy greater than 400 MeV.

From Figure 7.7 it can be seen that all peak to peak distances are more than 3mm apart, and the extraction peak to peak distances are 3.95 and 5.71mm for $1\pi\text{mmrad}$

7. BEAM ACCELERATION AND EXTRACTION STUDIES

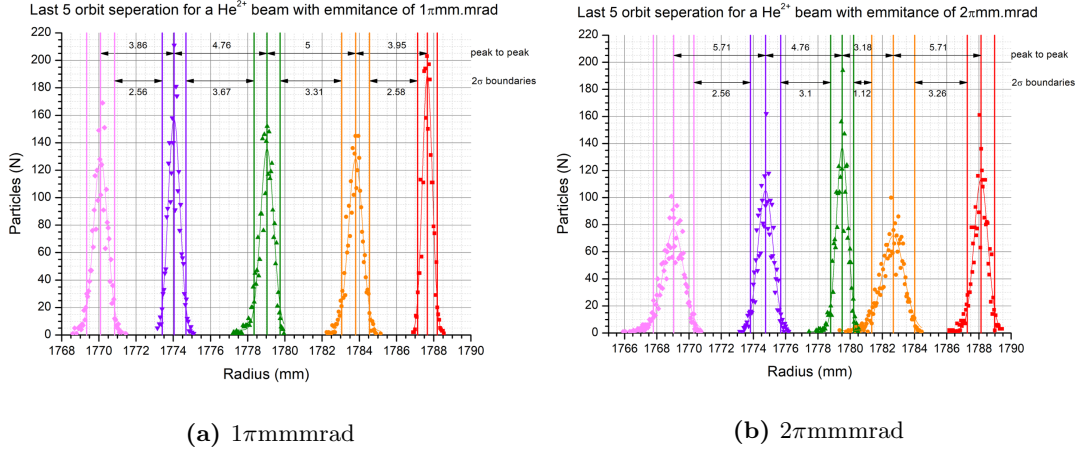


Figure 7.7: The radial profile of a He^{2+} beam for the last 5 turns for different initial beam sizes

and $2\pi\text{mmrad}$ beams, respectively. Assessing the distances between the 2σ boundaries of successive peaks shows distances of greater than 2.5mm between each peak except for between the 3rd and 4th peak for the $2\pi\text{mmrad}$ injected beam, where the distance is reduced to 1.12mm to allow for larger separation for the extraction orbit. Although not highlighted, there is a clear separation with no overlap of at least 1mm between all orbits for both cases, bar the 3rd and 4th peak for the 2nd case where there is tail overlap. Figure 7.8, the largest injected beam size of $5\pi\text{mmrad}$ has similar peak to peak distances compared to the smaller beam sizes but the wider beam reduces the 2σ distances, with an overlap between the 3rd and 4th peak, and there is no clear separation between orbits.

As identified earlier, a gap of 0.5mm should be sufficient to insert a septum in between successive orbits. A gap of 0.5mm and is more than achievable for 1 and $2\pi\text{mmrad}$ injected beams and no particles should directly hit the septum. This is not the case for the $5\pi\text{mmrad}$ injected beam. The simulations suggest there is enough space between the 2σ boundaries of the peaks for a septum, however the tails of the Gaussian distribution will likely be lost as they will hit the septum. Based on these results, the extracted $2\pi\text{mmrad}$ beam will be accelerated through stage 2.

7.6 Stage 2 Beam Acceleration

From Stage 1 the RMS beam width and emittance were taken exactly from the beam distribution at extraction from the initial injected $2\pi\text{mmrad}$ and were used identically

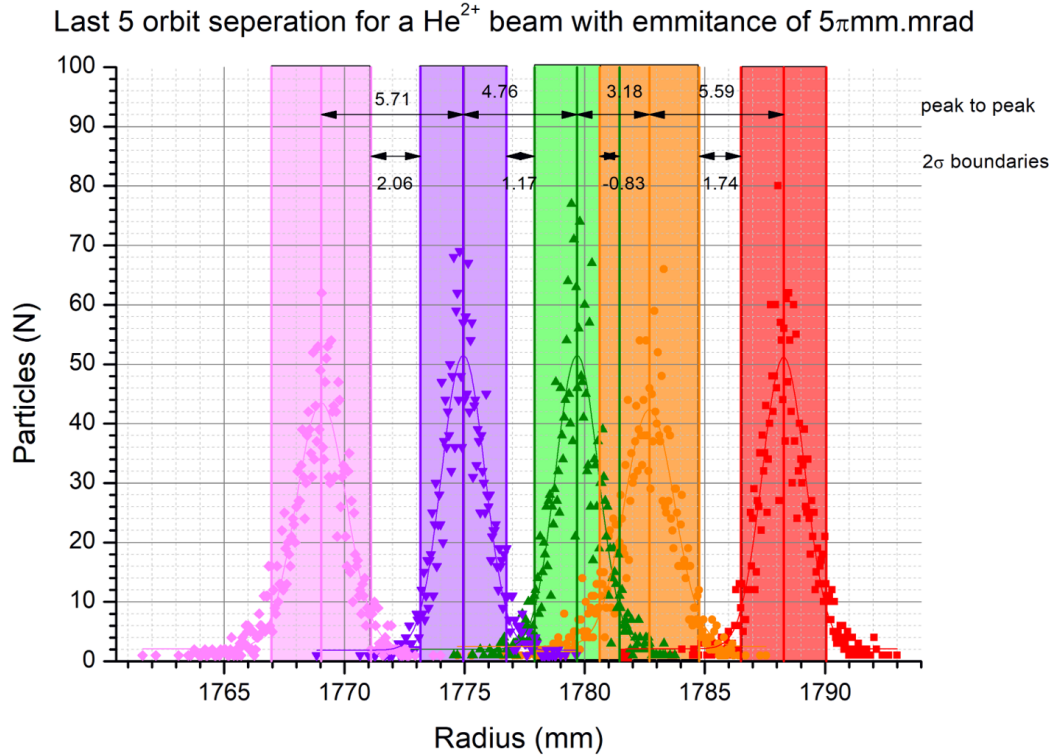


Figure 7.8: The radial profile of a He^{2+} beam for the last 5 turns for an He^{2+} beam with an initial emittance of $5\pi\text{mm.mrad}$

to insert a beam into stage 2. Initial optimisation changed the injection radius and angular momentum to produce equidistant orbits as shown in Figure 7.10 and then re-optimised to maximise the extraction orbit separation as depicted in Figure 7.11. The emittances in each plane are depicted in Figure 7.9 where no matching, as done for stage 1, was completed as there was no unusual growth from resonances.

Looking at the two optimised states of the last 5 orbits, it is clear from both cases that overlapping will occur, and losses will occur from hitting the septum. The peak to peak distance for the equidistant optimisation is approximately 2mm, however this has more than doubled to 4.13mm when bunching orbits radially. There is no 2σ boundary separation for the equidistant case however a separation of 1.75mm for the extraction orbit is present with bunching suggesting that it is possible to fit a septum in between the orbits, and it is estimated that losses on the septum will be a maximum of 4.2%. It is not foreseen that the bunched orbits will be an issue as they will be radially before

7. BEAM ACCELERATION AND EXTRACTION STUDIES

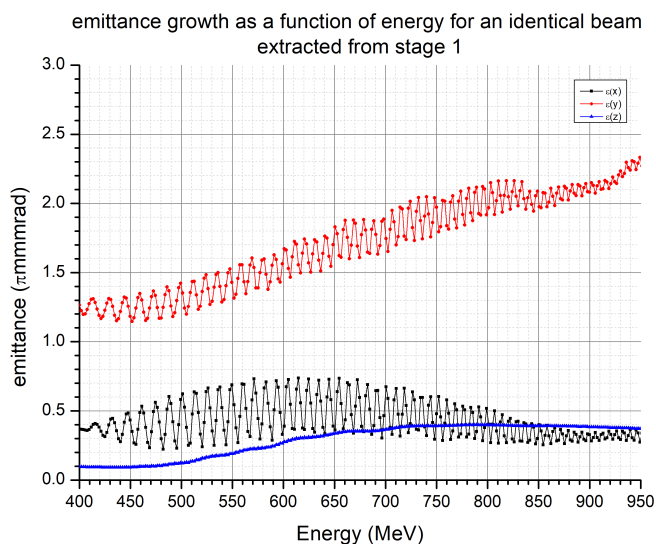


Figure 7.9: Stage 2 emittance growth across the acceleration regime

the inserted septum and will not affect the energy spread of the extracted beam. An example where orbits are bunched pre-extraction is the PSI ring cyclotron [116].

In practice, if the losses look like they will be a problem, there is potential to increase the gap size by using resonant extraction. From the working point diagram, it may be possible to achieve either brute force or processional extraction, as it appears to be heading towards an integer resonance. Larger orbit separation may also be achievable by reducing the emittance size, but it is still unlikely that there will be no overlap and no losses on the septum.

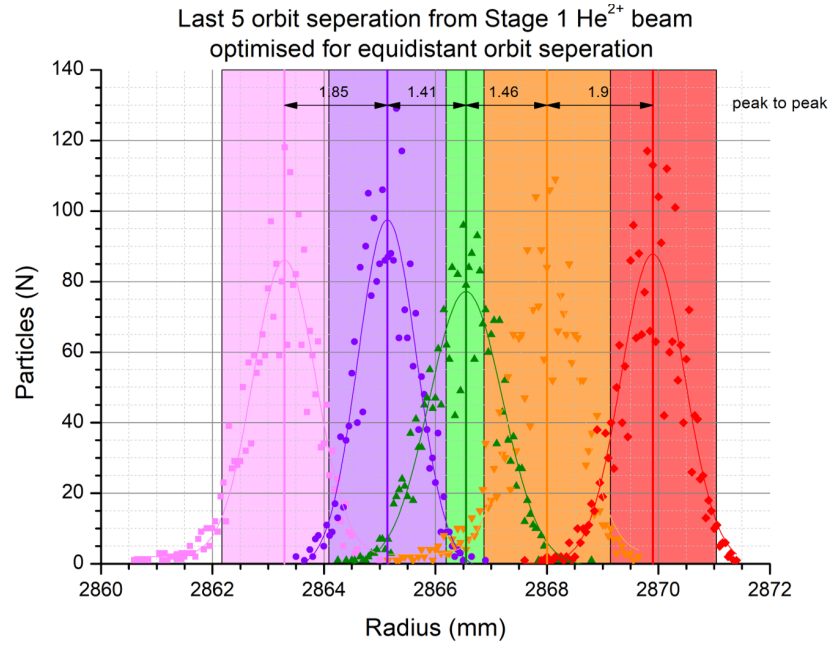


Figure 7.10: The radial profile of a He^{2+} beam from stage 1 with initial emittance of $2\pi\text{mmmrad}$ optimised to make the peaks equidistant

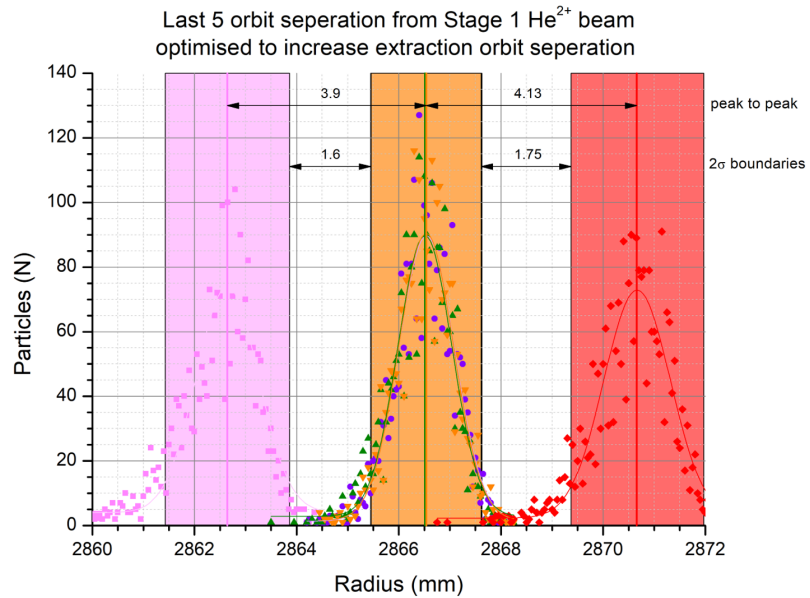


Figure 7.11: The radial profile of a He^{2+} beam from stage 1 with initial emittance of $2\pi\text{mmmrad}$ optimised to maximise the extraction peak separation orbit

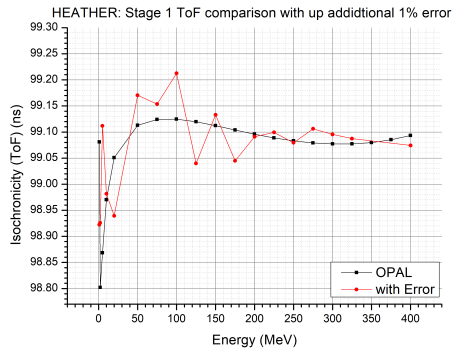
7.7 Magnetic Field Error

Magnets are never manufactured perfectly or identical to the design specification, and it is likely that there will be some discrepancy from the provided field map to what is achievable. Beyond this when manufactured and in place environmental factors such as temperature and local ferrous material can distort the magnetic field. To consider the potential effects of an imperfect field gradient two methods of magnetic error analysis are explored; the addition of up to $\pm 1\%$ of error on the magnetic fields and the addition or subtraction of up to a fixed value of error. Note that these errors are larger than normally achieved in magnet manufacture. Field Errors have only been introduced where a magnetic field is present, so there are no errors in the valley sections. Based on the previous optimisation work from it is expected that the introduced field map errors will have a larger effect on the isochronicity profile than the working point and disrupt the stable acceleration orbit.

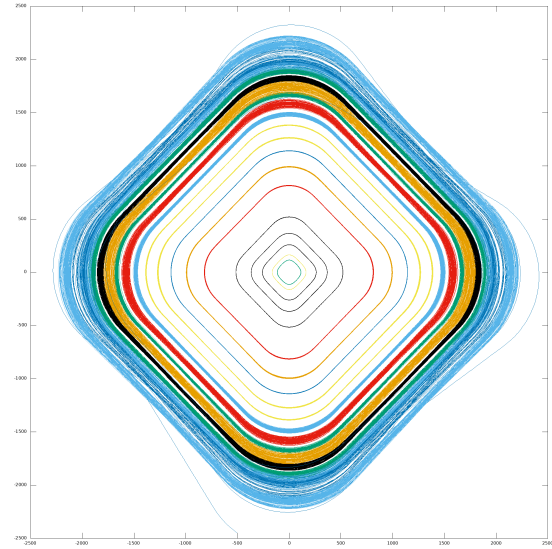
7.7.1 Stage $\pm 1\%$ error field map

Initially $\pm 1\%$ of the field was added to the field map for stage 1, by randomly assigning values to the field map before being read by OPAL and investigated. This initial concept was adventurous as the error will increase with the field gradient and more than likely exceed the size of the error. The errors were introduced and the isochronicity compared to the original field map in Figure 7.12a. It was not possible to calculate the tunes for the adjusted map. It became increasingly difficult to find stable orbits, as depicted by Figure 7.12b, which was due to the growth of the error. It can be seen the outer orbits have greater oscillations and a stable orbit could not be confined further.

It is thought that the radial field error made it difficult to find a stable acceleration orbit, however it was possible to accelerate a particle to the design energy. Unfortunately the design is very fragile, and when varying the initial phase of the particle to find the phase acceptance, the particle no longer reaches the design energy and is lost, as shown in Figure 7.13.



(a) Isochronicity variation with error



(b) 2π mmrad

Figure 7.12: Stable orbit properties introducing 1% error on the magnetic field

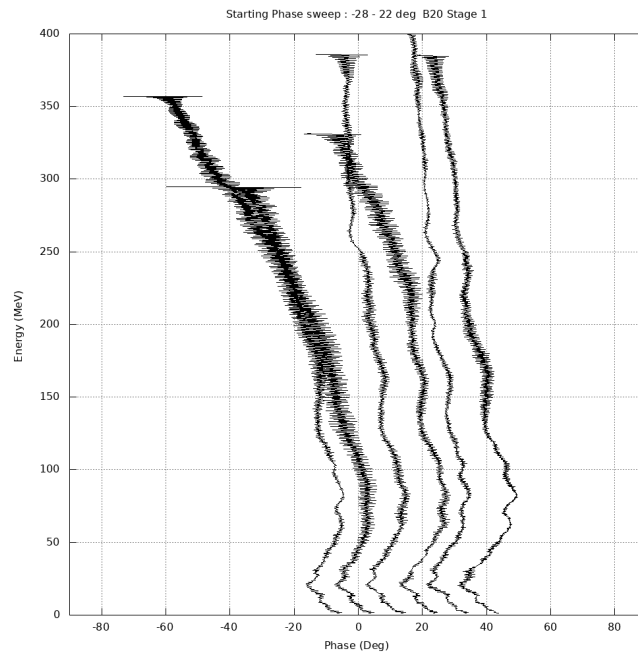


Figure 7.13: The RF phase space with an introduced percentage error. The accelerated is unstable, and the design energy is not reached when changing the initial phase of the particle

7. BEAM ACCELERATION AND EXTRACTION STUDIES

7.7.2 Stage 1 fixed error field map

This method of analysis used a fixed value of error along each point of the magnetic field, which is probably a more representative way of calculating the magnetic field error. Two fixed error values were used, 1% and 0.5% of the the lowest azimuthal magnetic field value; 3 Tesla. The stable orbits and isochronicity profile were not calculated for these field maps, as for the above error analysis the isochronicity seems reasonable, however acceleration was unsuccessful. Optimisation for the fixed error looked at the phase acceptance and compared it to the % error phase acceptance. Figures 7.14a and 7.14b show the phase space for 1% and 0.5% respectively. It can be seen that the phase acceptance with varying percentage in Figure 7.13 is comparable to the higher fixed error case, displayed by Figure 7.14a, suggesting that the size of the error is the cause of the instability. The reduced fixed error limit was found to be more acceptable, and a 30° phase acceptance was identified, advocating that this sort of error could be tolerated. This method used for studying errors is indicative, but a more apt method may be to go back to FACT and introduce errors for each magnetic order before generating the field map for OPAL, as opposed to adding it randomly afterwards.

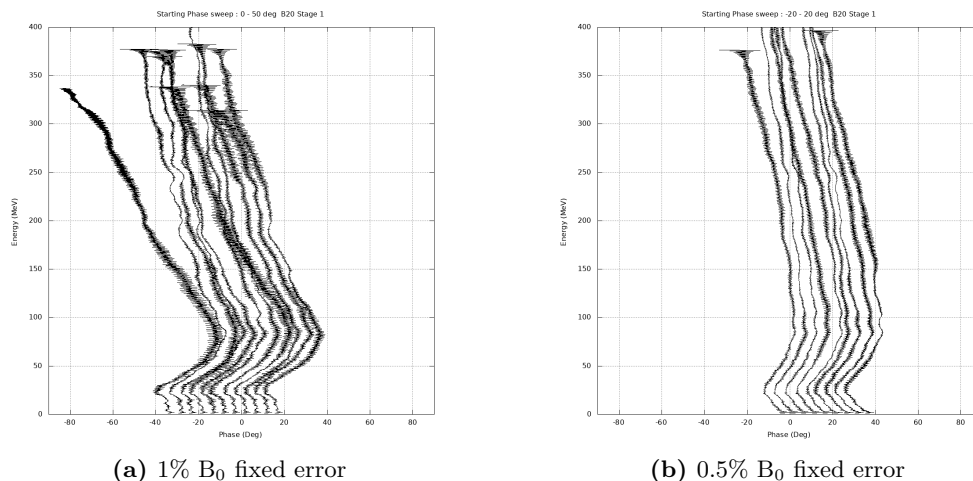


Figure 7.14: Depiction of the RF phase space with different fixed additional magnetic field error

8

Conclusions

With the current increasing popularity of particle therapy, the growth of proton therapy demonstrates the clinical interest globally in using particles for therapy. There are physical and clinical benefits when using ions heavier than protons, however the cost and size of these facilities make it very difficult to justify and implement. The limited availability also restricts research and the clinical rationale takes longer to generate. Beyond this, these machines that can accelerate ions are complex, and typically require specialist expertise to operate. A cheaper simpler compact alternative could increase the availability of ion therapy and enable further research in to heavier ions for radiotherapy.

A two stage non-scaling Fixed Field Alternating Gradient (nsFFAG) accelerator for the purpose of accelerating He^{2+} ions for particle therapy has been successfully designed. A nsFFAG design was chosen to provide a compact solution to provide fast CW acceleration of ions. The final achievable energy of 900 MeV clinically translates to approximately 30cm depth, and is necessary treat deep seated tumours.

The design was split into two stages, identified as stage 1 and stage 2. Stage 1 accelerates He^{2+} ions from 1 MeV to 400 MeV using a four sector magnet design. The field strength of the magnets causes overlapping of the fringe field at the inner radii which suppresses the vertical tune and decreases the path length. Once the orbits pass the fringe field overlap the isochronicity is within tolerances and the tune recovers. An integer resonance is crossed during acceleration, the crossing is fast and nearly perpendicular, so beam growth is minimised. Delta type double gap $\frac{1}{2}$ cavities with an accelerating voltage of 300kV per gap were found to be optimal for the design, operating at 50.46MHz.

Stage 2 is a racetrack design consisting of 6 sectors, accelerating from 400 MeV to

8. CONCLUSIONS

900 MeV. The racetrack design prevents any fringe field overlap, and provides more room for cavities, injection and extraction. The isochronicity for this stage was matched to within 1% of stage 1, enabling acceleration of the same frequency for both stages. The working point for this machine avoids integer resonance crossings but crosses a 2nd order resonance initially. Single gap resonant cavities were found to be optimal for this design, with an accelerating voltage of 500kV, operating at 50.46MHz.

Different beam sizes were accelerated that are typically representative of current accelerators, and a beam of 2π mmrad has been shown to be capable of being accelerated through both stages. The beam was matched into stage 1, and directly inserted into stage 2, and was accelerated through the accelerator without the need for matching. The initial accelerating beam parameters were optimised, and a clear 1mm between the last two orbits was identified; no losses are expected from the beam hitting the septum placed between the orbits when extracting. The initial beam parameters for stage 2 were optimised to maximise orbit separation for extraction. It was found that by overlapping the successive orbits before extraction, a larger separation between the last two orbits can be achieved. In this case there is some overlap, and minimal losses are expected on the septum. This work has demonstrated the potential of a nsFFAG for helium ion therapy.

8.1 Future work

There are still aspects of this design that need to be further explored which are beyond the scope of this thesis.

8.1.1 Particle source and pre acceleration

Pre acceleration was discussed in Chapter 7, but the particle source has not been considered. Although the beam emittance used was estimated using existing ion sources, the source and pre accelerator will determine the size of the beam entering stage 1. It looks likely the emittance will be smaller than anticipated, which will improve orbit separation for extraction.

8.1.2 Transfer lines

Two beam lines will need to be designed; from the pre-accelerator into stage 1, and stage 1 into stage 2. This will require a full detailed study, and software such as MADX [135] can be used to model the beam lines. From the simulations in Chapter 7 the

beam line design between stage 1 and stage 2 should require no matching and be a simple drift tube. The first beam line may require more work.

8.1.3 Magnet design

Although work has been completed on the magnet design, a full 3D model of the magnets needs to be completed. This will confirm the azimuthal gradient, the size of the pole gap, the magnet dimensions and error tolerances. This work will need to be completed in specialist software like Opera3D [136]. Detailed Magnet studies have already started for the other nsFFAG design in our group, PIP, [108] using Opera3D, as shown in Figure 8.1

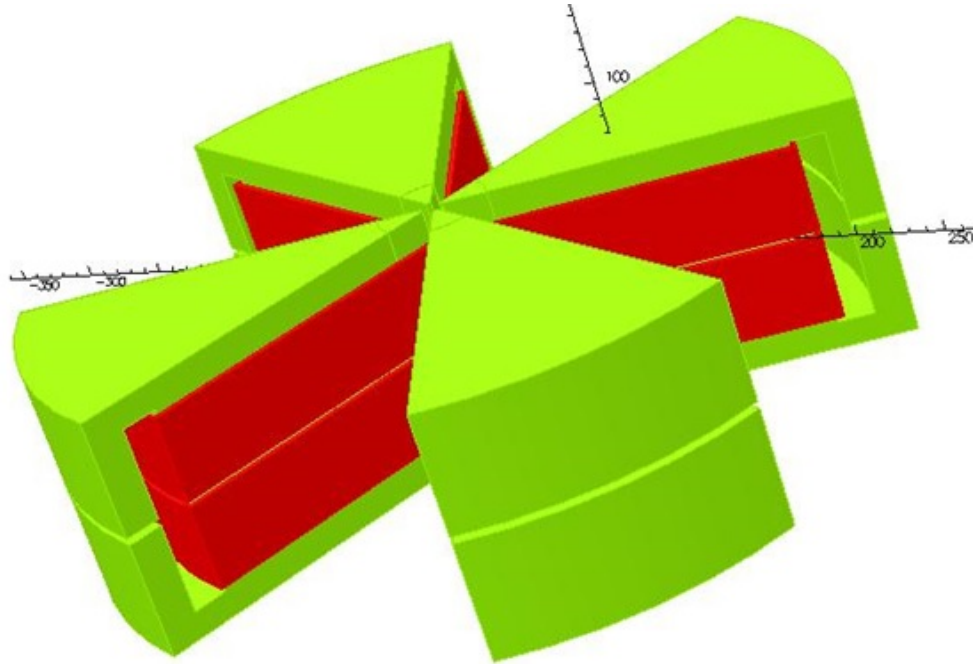


Figure 8.1: Magnet design work for PIP, a different FFAG design within the collaboration [108] [137].

8.1.4 RF design

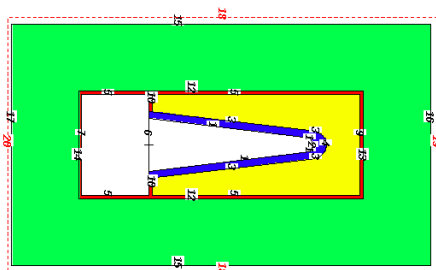
The RF system also requires a full detailed cavity design. Realistic properties were considered in this thesis, increasing the likelihood that the desired outcome will be

8. CONCLUSIONS

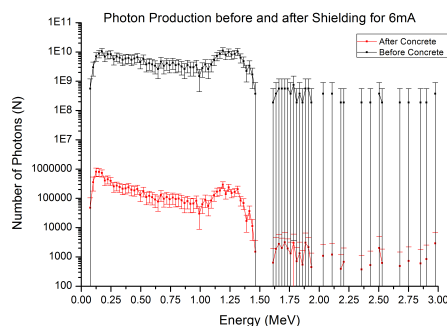
feasible, but ultimately this is unknown until the cavities are specifically designed. It is expected that a cavity design will be studied in finite element analysis software, e.g. computer simulation technology (CST) [138].

8.1.5 Variable Energy

Currently the design extracts at single energy, but there is an idea within the group to use harmonic jumping for variable energy extraction. If variable energy is not achievable the extracted beam will need to be degraded. The consequence of beam degradation for particles are the low secondaries produced, and the increased shielding necessary because of it. This could be investigated using Monte Carlo simulations to both degrade the beam, and calculate the shielding necessary. I have already completed work using MCNPX [139] for a similar project in collaboration with the Front End Test Stand (FETS) the Rutherford Appleton laboratory (RAL), UK [140]. The 3 MeV proton beam leaving the accelerator will be disposed of by depositing the beam into a beam dump, an aluminium conical shape surrounded by water. I used MCNPX to simulate a proton beam hitting the beam dump, and assessed the interactions between protons and aluminium, and looked to see if shielding being used would be sufficient (Figure 8.2). A full shielding design will go beyond this, taking into consideration annual dose restrictions for surrounding rooms and typical workloads of the machine. There is scope to complete this work with a Radiation Protection Advisor (RPA) and treat the shielding design as if it was going into a current hospital, following the relevant legislation [141] and guidelines [142].



(a) The FETS beam dump geometry built in MCNPX. The figure shows a slice in the YZ plane. Blue represents the beam dump.



(b) After inserting concrete shielding the photons penetrating the concrete are reduced by a factor of 10^3

Figure 8.2: MCNPX simulations on the Front End Test Stand (FETS) beam dump for shielding purposes

8.1.6 Extraction

Further detailed work needs to be carried out on the extraction on both stages. The use of the brute force method by introducing field bumps would be the easiest way to investigate this. It may be necessary to look at other codes to study this further.

8.1.7 Beyond the current design

There is also scope to modify the designs of the accelerators, and further alter the field maps. It could be possible to alter the field map to reach 900 MeV with one stage as opposed to two stages. This would reduce the footprint and make the project much cheaper. Both stages can exceed their design energy, with a phase slip, by up to 40%. This needs to be further investigated as the current design does not reach the necessary energy to image with ionised dihydrogen, but it is clear there is a possibility to do this. The RF for stage 2 could be redesigned to use 4 cavities in corner spaces, which could increase orbit separation.

8.2 Summary

In this thesis, the question as to whether it is feasible to accelerate He^{2+} to 900 MeV in a compact accelerator that could fit in current medical facilities, has been investigated and I believe it has been answered. The accelerator that has been designed, HEATHER, has demonstrated that a nsFFAG solution could be compact enough to fit in the basement of a hospital. Technological and physical boundaries have been considered, and a conservative approach taken as to not push these limitations. Manufacturing aspects have been considered, where all of the magnet parameters are identical, simplifying the process. Clinically the machine should be easy to use, like other medical isochronous cyclotrons, where minimal specialised staff are required to run the facility. The design itself is also split across two stages, where the first stage extracts a beam with energy of 100 MeV/u. Clinically stage one could be used without stage 2 for research purposes or for shallower tumour depths, for example, for paediatric patients.

8. CONCLUSIONS

Appendix A

Appendix

A.1 Enge Edge

below is an example input for FACT in the Enge Edge format.

NSFFAG 2 2 (this dictates the amount of magnets)

P12 1 (first line)

0.04727592878 0.01627840772 (start z, length)

1.56010565 0.5371874549 (start x, length)

P21 1 (second line)

0.01627840772 0.04727592878 (start x, length)

0.5371874549 1.56010565 (start x, length)

D1 0

0.01 (aperture)

D2 0

0.01(aperture)

B1 2 (1st magnet, number is magnet order)

3 (dipole)

-0.008 (quadrupole)

0.0746 (sextupole)

B2 2 (2nd magnet, number is magnet order)

3 (dipole)

-0.008 (quadrupole)

0.0746 (sextupole)

A.2 Kilpatrick equation

$$f = 1.64x^2 e^{-\frac{8.5}{x}}$$

$$\frac{f}{1.64} = x^2 e^{-\frac{8.5}{x}}$$

$$\frac{1.64}{f} = \frac{1}{x^2} e^{\frac{8.5}{x}}$$

$$\frac{1.28}{\sqrt{f}} = \frac{1}{x} e^{\frac{4.25}{x}}$$

$$\frac{5.24}{\sqrt{f}} = \frac{4.25}{x} e^{\frac{4.25}{x}}$$

using the product log function $y = xe^x$ $W(y) = x$

$$x = \frac{4.25}{W\left(\frac{5.24}{\sqrt{f}}\right)}$$

References

- [1] CANCER RESEARCH UK. **Cancer in the UK 2018.** https://www.cancerresearchuk.org/sites/default/files/state_of_the_nation_apr_2018_v2_0.pdf, 2018. 15
- [2] CANCER RESEARCH UK. **Vision for radiotherapy 2014 - 2024.** https://www.cancerresearchuk.org/sites/default/files/policy_feb2014_radiotherapy_vision2014-2024_final.pdf, 2014. 15
- [3] RAJAMANICKAM BASKAR, KUO ANN LEE, RICHARD YEO, AND KHENG-WEI YEOH. **Cancer and radiation therapy: current advances and future directions.** *International journal of medical sciences*, **9**(3):193, 2012. 15
- [4] HELLEN GELBAND, PRABHAT JHA, RENGASWAMY SANKARANARAYANAN, AND SUSAN HORTON. *Disease Control Priorities, (Volume 3): Cancer.* World Bank Publications, 2015. 15
- [5] WILHELM CONRAD RÖNTGEN. **Ueber eine neue Art von Strahlen.** *Annalen der Physik*, **300**(1):1–11, 1898. 15
- [6] VICTOR DESPEIGNES. **Observation concernant un cas de cancer de l'estomac traite par les rayons Rontgen.** *Lyon méd.*, **82**:428–430, 1896. 15
- [7] NICOLAS FORAY. **Victor Despeignes, the forgotten pioneer of radiation oncology.** *International Journal of Radiation Oncology• Biology• Physics*, **96**(4):717–721, 2016. 15
- [8] KONRAD LESZCZYNSKI AND SUSAN BOYKO. **On the controversies surrounding the origins of radiation therapy.** *Radiotherapy and oncology*, **42**(3):213–217, 1997. 15

REFERENCES

- [9] JOHN D COCKCROFT AND ERNEST TS WALTON. **Artificial production of fast protons.** *nature*, **129**(3250):242, 1932. 15, 39
- [10] TE ALLIBONE, FE BANCROFT, AND GS INNES. **The St. Bartholomew’s Hospital X-ray tube for one million volts.** *Journal of the Institution of Electrical Engineers*, **85**(516):657–673, 1939. 15
- [11] DAVID I THWAITES AND JOHN B TUOHY. **Back to the future: the history and development of the clinical linear accelerator.** *Physics in Medicine & Biology*, **51**(13):R343, 2006. 15
- [12] CHARLES WALTER MILLER. **An 8-MeV linear accelerator for X-ray therapy.** *Proceedings of the IEE-Part I: General*, **101**(130):207–221, 1954. 15
- [13] ROBERT R WILSON. **Radiological use of fast protons.** *Radiology*, **47**(5):487–491, 1946. 16, 32
- [14] ERNEST O LAWRENCE. **Method and apparatus for the acceleration of ions**, February 20 1934. US Patent 1,948,384. 10, 16, 43, 44
- [15] JOHN H LAWRENCE, JOHN A LINFOOT, JAMES L BORN, CORNELIUS A TOBIAS, AND EDWARD MANOUGIAN. **Heavy Particle Therapy in Acromegaly and Cushing’s Disease.** *Annals of Internal Medicine*, **63**(5):908–908, 1965. 16
- [16] DE BONNETT, A KACPEREK, MA SHEEN, R GOODALL, AND TE SAXTON. **The 62 MeV proton beam for the treatment of ocular melanoma at Clatterbridge.** *The British journal of radiology*, **66**(790):907–914, 1993. 16
- [17] PARTICLE THERAPY CO-OPERATIVE GROUP. **Particle Therapy Patient Statistics (per end of 2016).** https://www.ptcog.ch/archive/patient_statistics/Patientstatistics-updateDec2016.pdf. accessed August 2018. 16, 17, 34
- [18] PROTON PARTNERS INTERNATIONAL. **Proton Partners International.** https://www.proton-int.com/index.php?/article/news/proton-partners_international_announces_partnership_with_global_leaders_to_equip_uks_first_proton_beam_therapy_centres. accessed 2018. 17
- [19] NATIONAL HEALTH SERVICE (NHS). **Proton beam therapy.** <https://www.england.nhs.uk/commissioning/spec-services/highly-spec-services/pbt/>. accessed 2018. 17

-
- [20] A CRELLIN. **The Road Map for National Health Service Proton Beam Therapy.** *Clinical Oncology*, **30**(5):277–279, 2018. 17
- [21] PARTICLE THERAPY CO-OPERATIVE GROUP. **Particle therapy facilities in operation.** <https://www.ptcog.ch/index.php/facilities-in-operation>. accessed August 2018. 17, 35, 51
- [22] JR CASTRO, JM QUIVEY, JT LYMAN, GT CHEN, TL PHILLIPS, AND CA TOBIAS. **Radiotherapy with heavy charged particles at Lawrence Berkeley Laboratory.** *Journal of the Canadian Association of Radiologists*, **31**(1):30–34, 1980. 17
- [23] DANIEL K EBNER AND TADASHI KAMADA. **The emerging role of carbon-ion radiotherapy.** *Frontiers in oncology*, **6**:140, 2016. 17, 35
- [24] NATIONAL HEALTH SERVICE (NHS). **NHS England launches biggest upgrade to NHS cancer treatment in 15 years.** <https://www.england.nhs.uk/2016/10/radiotherapy-fund/>. accessed 2018. 18, 34
- [25] WD KILPATRICK. **Criterion for vacuum sparking designed to include both rf and dc.** *Review of Scientific Instruments*, **28**(10):824–826, 1957. 11, 19, 85, 86
- [26] H PAGANETTI. **Range uncertainties in proton therapy and the role of Monte Carlo simulations.** *Physics in medicine and biology*, **57**(11):R99–117, 2012. 22, 30, 62
- [27] MARK A RITTER, JAMES E CLEAVER, AND CORNELIUS A TOBIAS. **High-LET radiations induce a large proportion of non-rejoining DNA breaks.** *Nature*, **266**(5603):653, 1977. 22
- [28] MEGUMI HADA AND ALEXANDROS G GEORGAKILAS. **Formation of clustered DNA damage after high-LET irradiation: a review.** *Journal of radiation research*, **49**(3):203–210, 2008. 22
- [29] HIROHIKO TSUJII, TADASHI KAMADA, MASAYUKI BABA, HIROSHI TSUJI, HIROTOSHI KATO, SHINGO KATO, SHIGERU YAMADA, SHIGEO YASUDA, TAKESHI YANAGI, HIROYUKI KATO, ET AL. **Clinical advantages of carbon-ion radiotherapy.** *New Journal of Physics*, **10**(7):075009, 2008. 23, 35

REFERENCES

- [30] GLENN F KNOLL. *Radiation detection and measurement*. John Wiley & Sons, 2010. 10, 23, 25
- [31] SWANSEA UNIVERSITY. **Biological Effects of Ionising Radiation**. Swansea University Medical Radiation Physics Masters course, EGRM09 course notes. obtained 2012/2013. 23, 24
- [32] RADIOLOGICAL PROTECTION. **ICRP publication 103**. *Ann ICRP*, **37**(2.4):2, 2007. 23
- [33] OZRADONC. **Descriptors Of Dose Distribution**. <http://ozradonc.wikidot.com/descriptors-of-dose-distribution-photons>. accessed 2018. 10, 27
- [34] DAVID P DEARNALEY, VINCENT S KHOO, ANDREW R NORMAN, LESLEY MEYER, ALAN NAHUM, DIANA TAIT, JOHN YARNOLD, AND ALAN HORWICH. **Comparison of radiation side-effects of conformal and conventional radiotherapy in prostate cancer: a randomised trial**. *The Lancet*, **353**(9149):267–272, 1999. 26
- [35] HARALD PAGANETTI. *Proton therapy physics*. CRC Press, 2016. 26, 32
- [36] NATIONAL HEALTH SERVICE (NHS). **Side effects of Radiotherapy**. <https://www.nhs.uk/conditions/radiotherapy/side-effects/>. accessed 2018. 26
- [37] JOEP C STROOM, HANS CJ DE BOER, HENK HUIZENGA, AND ANDRIES G VISSER. **Inclusion of geometrical uncertainties in radiotherapy treatment planning by means of coverage probability**. *International Journal of Radiation Oncology* Biology* Physics*, **43**(4):905–919, 1999. 27
- [38] KY CHEUNG. **Intensity modulated radiotherapy: advantages, limitations and future developments**. *Biomed Imaging Interv J*, **2**(1):e19, 2006. 27
- [39] BIJAN ARJOMANDY. **Proton therapy advancement**. *Journal of Proton Therapy*, **1**(1), 2015. 10, 28
- [40] H PAGANETTI. **Nuclear interactions in proton therapy: dose and relative biological effect distributions originating from primary and secondary particles**. *Physics in Medicine & Biology*, **47**(5):747, 2002. 30

-
- [41] HH BARSCHALL, MB CHADWICK, DTL JONES, JP MEULDERS, H SCHUMACHER, PG YOUNG, LJ COX, GM HALE, U SCHREWE, JV SIEBERS, ET AL. **Nuclear data for neutron and proton radiotherapy and for radiation protection.** *ICRU Report*, **63**, 1999. 30
- [42] SIMON EIDELMAN, KG HAYES, KA EA OLIVE, M AGUILAR-BENITEZ, C AMSLER, D ASNER, KS BABU, RM BARNETT, J BERINGER, PR BURCHAT, ET AL. **Review of particle physics.** *Physics Letters B*, **592**(1-4):1–5, 2004. 10, 30, 31
- [43] JAMES F ZIEGLER, MATTHIAS D ZIEGLER, AND JOCHEN P BIRSACK. **SRIM—The stopping and range of ions in matter (2010).** *Nuclear Instruments and Methods in Physics Research Section B: Beam Interactions with Materials and Atoms*, **268**(11-12):1818–1823, 2010. 10, 33
- [44] VARIAN. **ProBeam® Compact Single-Room Proton Therapy Solution.** <https://www.varian.com/en-gb/oncology/products/treatment-delivery/probeam-compact-proton-therapy-solution>. accessed 2018. 34
- [45] THOMAS R BORTFELD AND JAY S LOEFFLER. **Three ways to make proton therapy affordable.** *Nature News*, **549**(7673):451, 2017. 34
- [46] MARK KNIGHT. private communication. 34
- [47] MEVION MEDICAL SYSTEMS. **Mevion proton therapy products.** <http://www.mevion.com/products>. accessed 2018. 34
- [48] HARALD PAGANETTI, ANDRZEJ NIEMIERKO, MAREK ANCUKIEWICZ, LEO E GERWECK, MICHAEL GOITEIN, JAY S LOEFFLER, AND HERMAN D SUIT. **Relative biological effectiveness (RBE) values for proton beam therapy.** *International Journal of Radiation Oncology* Biology* Physics*, **53**(2):407–421, 2002. 34
- [49] ALEJANDRO CARABE, MARYAM MOTEABBED, NICOLAS DEPAUW, JAN SCHUEMANN, AND HARALD PAGANETTI. **Range uncertainty in proton therapy due to variable biological effectiveness.** *Physics in Medicine & Biology*, **57**(5):1159, 2012. 34
- [50] AL ZIETMAN. **Too big to fail? The current status of proton therapy in the USA**, 2017. 34

REFERENCES

- [51] R AMOS, H BULBECK, NG BURNET, A CRELLIN, D EATON, PHILIP EVANS, E HALL, MA HAWKINS, KAREN J KIRKBY, R MACKAY, ET AL. **Proton Beam Therapy—the Challenges of Delivering High-quality Evidence of Clinical Benefit.** *Clinical Oncology*, **30**(5):280–284, 2018. 34
- [52] MARCO DURANTE AND HARALD PAGANETTI. **Nuclear physics in particle therapy: a review.** *Reports on Progress in Physics*, **79**(9):096702, 2016. 34, 37
- [53] MALIN HOLLMARK, JOHAN UHRDIN, DŽ BELKIĆ, IRENA GUDOWSKA, AND ANDERS BRAHME. **Influence of multiple scattering and energy loss straggling on the absorbed dose distributions of therapeutic light ion beams: I. Analytical pencil beam model.** *Physics in Medicine & Biology*, **49**(14):3247, 2004. 35, 38
- [54] JOSE R ALONSO. **Review of ion beam therapy: present and future.** 2000. 35, 37
- [55] PARTICLE THERAPY CO-OPERATIVE GROUP. **Particle therapy facilities under construction.** ”<https://www.ptcog.ch/index.php/facilities-under-construction>”. accessed August 2018. 35
- [56] TOSHIBA ENERGY SYSTEMS AND SOLUTIONS CORPORATION. **Heavy ion therapy.** <https://www.toshiba-energy.com/en/heavy-ion/product/layout-design.htm>. accessed 2018. 35
- [57] D ONDREKA AND U WEINRICH. **The Heidelberg Ion Therapy (HIT) accelerator coming into operation.** *Proceedings of EPAC08*, pages 979–81, 2008. 35
- [58] P URSCHÜTZ, O CHUBAROV, S EMHOFER, S GÖLLER, K HASS, C KLEFFNER, V LAZAREV, M LEGHISSA, HK ANDERSEN, M BUDDE, ET AL. **Status of the SIEMENS particle therapy accelerators.** *Proc. of IPAC*, **70**, 2010. 35
- [59] G BALBINOT, J BOSSER, A PARRAVICINI, C BISCARI, C VIVIANI, E BRESSI, A GHIGO, C PRIANO, M PULLIA, M CALDARA, ET AL. **CNAO Synchrotron Commissioning.** In *Conf. Proc.*, **110904**, pages 2496–2498, 2011. 35
- [60] MICHAEL BENEDIKT, JOHANNES GUTLEBER, U DORDA, ADRIAN FABICH, M PALM, AND W PIRKL. **Overview of the MedAustron design and technology choices.** Technical report, 2010. 35

-
- [61] M GALONSKA, S SCHELOSKE, R CEE, A GAFFRON, K HÖPPNER, CM KLEFFNER, A PETERS, AND T HABERER. **Commissioning of the carbon beam gantry at the Heidelberg Ion Therapy (HIT) accelerator.** *Proc. WAO, April*, 2010. 35
- [62] YOSHIYUKI IWATA, NAOYUKI AMEMIYA, HIROKI ARAI, TETSUYA FUJIMOTO, TAKASHI FUJITA, TAKUJI FURUKAWA, YOUSUKE HARA, SHUNYA MATSUBA, KOTA MIZUSHIMA, SHINICHIRO MORI, ET AL. **Present status of a superconducting rotating-gantry for carbon therapy.** In *13th Heavy Ion Accelerator Technology Conference (HIAT2015), Yokohama, Japan, 7-11 September 2015*, pages 288–290. JACOW, Geneva, Switzerland, 2016. 35
- [63] HEIDELBERG ION-BEAM THERAPY CENTER. **Carbon ion gantry at Heidelberg ion-beam therapy center (HIT).** https://www.klinikum.uni-heidelberg.de/fileadmin/pressestelle/PM_neu/10_2012/pm_132_12_Gantry_291012_2.jpg. accessed 2018. 10, 36
- [64] WILLIAM T CHU. **Overview of light-ion beam therapy.** 2006. 10, 37
- [65] DIETER SCHARDT, THILO ELSÄSSER, AND DANIELA SCHULZ-ERTNER. **Heavy-ion tumor therapy: Physical and radiobiological benefits.** *Reviews of modern physics*, **82**(1):383, 2010. 37
- [66] DEVRON H CHAR, JEANNE M QUIVEY, JOSEPH R CASTRO, STEWART KROLL, AND THEODORE PHILLIPS. **Helium ions versus iodine 125 brachytherapy in the management of uveal melanoma: a prospective, randomized, dynamically balanced trial.** *Ophthalmology*, **100**(10):1547–1554, 1993. 38
- [67] JOSEPH R CASTRO. **Results of heavy ion radiotherapy.** *Radiation and environmental biophysics*, **34**(1):45–48, 1995. 38
- [68] HERMANN FUCHS, MARKUS ALBER, THOMAS SCHREINER, AND DIETMAR GEORG. **Implementation of spot scanning dose optimization and dose calculation for helium ions in Hyperion.** *Medical physics*, **42**(9):5157–5166, 2015. 38
- [69] DEVRON H CHAR, STEWART M KROLL, AND JOSEPH CASTRO. **Ten-year follow-up of helium ion therapy for uveal melanoma.** *American journal of ophthalmology*, **125**(1):81–89, 1998. 38

REFERENCES

- [70] T TESSONNIER, A MAIRANI, S BRONS, P SALA, F CERUTTI, A FERRARI, T HABERER, J DEBUS, AND K PARODI. **Helium ions at the heidelberg ion beam therapy center: comparisons between FLUKA Monte Carlo code predictions and dosimetric measurements.** *Physics in Medicine & Biology*, **62**(16):6784, 2017. 38
- [71] M MARAFINI, R PARAMATTI, D PINCI, G BATTISTONI, F COLLAMATI, E DE LUCIA, R FACCINI, PM FRALLICCIARDI, C MANCINI-TERRACCIANO, I MATTEI, ET AL. **Secondary radiation measurements for particle therapy applications: nuclear fragmentation produced by 4He ion beams in a PMMA target.** *Physics in Medicine & Biology*, **62**(4):1291, 2017. 38
- [72] H GREINACHER. **Über eine Methode, Wechselstrom mittels elektrischer Ventile und Kondensatoren in hochgespannten Gleichstrom umzuwandeln.** *Zeitschrift für Physik*, **4**(2):195–205, 1921. 40
- [73] F HINTERBERGER. **Electrostatic accelerators.** 2006. 40, 42
- [74] UNKNOWN. **NAIG: Negative Air Ion Generator.** <http://vitency.com/electronics/naig.html>. accessed 2018. 40
- [75] ROBERT J VAN DE GRAAFF, KT COMPTON, AND LC VAN ATTA. **The electrostatic production of high voltage for nuclear investigations.** *Physical Review*, **43**(3):149, 1933. 40
- [76] LIBRETEXTS LIBRARIES. **The Van de Graaff Generator.** "https://tinyurl.com/y8fq92pm". accessed 2018. 41
- [77] SCIENCE AND TECHNOLOGY FACILITIES COUNCIL (STFC). **The life history of an internationally renowned laboratory nestled in the heart of Cheshire.** <https://stfc.ukri.org/public-engagement/activities-for-the-public/visit-daresbury-laboratory/daresbury-open-week/daresbury-timeline/>. accessed 2018. 41
- [78] NATIONAL ELECTROSTATICS CORP. **Tandem vs. Single Ended.** <http://www.pelletron.com/products/tandem-vs-single-ended/>. accessed 2018. 10, 42
- [79] HE WEGNER. **Tandem Accelerators.** *IEEE Trans. on Nuclear Science*, (3):81, 1969. 42

-
- [80] NRS TAIT AND RGP VOSS. **The nuclear structure facility 20/30 MV tandem accelerator.** *Part. Accel.*, **5**:181–197, 1973. 42
- [81] LYNN YARRIS. **Ernest Lawrence’s Cyclotron:Invention for the Ages.** <http://www2.lbl.gov/Science-Articles/Archive/early-years.html>. accessed 2018. 43
- [82] FRÉDÉRIC CHAUTARD. **Beam dynamics for cyclotrons.** 2006. 10, 47, 48, 50
- [83] DONALD W KERST. **Historical development of the betatron.** *Nature*, **157**(3978):90, 1946. 48
- [84] VLADIMIR ISAAKOVICH VEKSLER. **A new method of acceleration of relativistic particles.** *J. Phys.*, **9**:153–158, 1945. 50
- [85] ROB APPLEBY. **Cockcroft Institute lecture series.** https://sas.stfc.ac.uk/vportal/fileUploads/prod/A-70bc993c-3fa2-46cc-bb01-3c08d4d0b3f3-9ac302e6-c434-4d7d-b568-1c535b9dcdfc_rob_parts456.pdf. accessed 2018. 10, 50
- [86] HYWEL OWEN, ANTONY LOMAX, AND SIMON JOLLY. **Current and future accelerator technologies for charged particle therapy.** *Nuclear Instruments and Methods in Physics Research Section A: Accelerators, Spectrometers, Detectors and Associated Equipment*, **809**:96–104, 2016. 51
- [87] A RUGGIERO. *BRIEF HISTORY OF FFAG ACCELERATORS.* 52
- [88] BASROC. **FFAG accelerators.** <http://basroc.rl.ac.uk/ns-ffags.htm>. accessed 2018. 10, 52, 55
- [89] KR SYMON, DW KERST, LW JONES, LJ LASLETT, AND KM TERWILLIGER. **Fixed-field alternating-gradient particle accelerators.** *Physical Review*, **103**(6):1837, 1956. 52
- [90] TIHIRO OHKAWA. **Two-Beam Fixed Field Alternating Gradient Accelerator.** *Review of Scientific Instruments*, **29**(2):108–117, 1958. 52
- [91] A KOLOMENSKY. **A. Kolomensky, Zh. Eksp. Teor. Fiz. 33, 298 (1957).** *Zh. Eksp. Teor. Fiz.*, **33**:298, 1957. 52
- [92] LAWRENCE W JONES AND KENT M TERWILLIGER. **A small model fixed field alternating gradient radial sector accelerator.** 1956. 52

REFERENCES

- [93] LAWRENCE W JONES. **Kent M. Terwilliger; graduate school at Berkeley and early years at Michigan, 1949–1959.** In *AIP Conference Proceedings CONF- 8910344*, **237**, pages 1–21. AIP, 1991. 52
- [94] CAROL JOHNSTONE, W WAN, AND A GARREN. **Fixed field circular accelerator designs.** In *Particle Accelerator Conference, 1999. Proceedings of the 1999*, **5**, pages 3068–3070. IEEE, 1999. 52, 53
- [95] MK CRADDOCK. **FFAG optics.** https://www.cockcroft.ac.uk/events/ffag11/FFAG_talks/11/5.Craddock.pdf. Talk given at FFAG’11 accessed 2019. 54
- [96] M AIBA, K Koba, S MACHIDA, Y MORI, R MURAMATSU, C OHMORI, I SAKAI, Y SATO, A TAKAGI, R UENO, ET AL. **Development of a FFAG proton synchrotron.** In *Proceedings of EPAC*, **581**, 2000. 55
- [97] SL SHEEHY. **Fixed-Field Alternating-Gradient Accelerators.** *arXiv preprint arXiv:1604.05221*, 2016. 55
- [98] ROGER BARLOW, JS BERG, C BEARD, N BLISS, J CLARKE, MK CRADDOCK, J CRISP, R EDGECOCK, Y GIBOUDOT, P GOUDKET, ET AL. **EMMA—The world’s first non-scaling FFAG.** *Nuclear Instruments and Methods in Physics Research Section A: Accelerators, Spectrometers, Detectors and Associated Equipment*, **624(1)**:1–19, 2010. 55, 63, 93
- [99] R EDGECOCK. **EMMA-the World’s First Non-scaling FFAG.** In *Particle Accelerator Conference, 2007. PAC. IEEE*, pages 2624–2626. IEEE, 2007. 55
- [100] SCIENCE AND TECHNOLOGY FACILITIES COUNCIL (STFC). **EMMA.** <https://stfc.ukri.org/Images/emma/>. accessed 2018. 10, 56
- [101] K. J. PEACH, M. ASLANINEJAD, R. J. BARLOW, C. D. BEARD, N. BLISS, J. H. COBB, M. J. EASTON, T. R. EDGECOCK, R. FENNING, I. S. K. GARDNER, M. A. HILL, H. L. OWEN, C. J. JOHNSTONE, B. JONES, T. JONES, D. J. KELLIHER, A. KHAN, S. MACHIDA, P. A. MCINTOSH, S. PATTALWAR, J. PASTERNAK, J. POZIMSKI, C. R. PRIOR, J. ROCHFORD, C. T. ROGERS, R. SEVIOUR, S. L. SHEEHY, S. L. SMITH, J. STRACHAN, S. TYGIER, B. VOJNOVIC, P. WILSON, H. WITTE, AND T. YOKOI. **Conceptual design of a nonscaling fixed field alternating gradient accelerator for protons and**

-
- carbon ions for charged particle therapy.** *Phys. Rev. ST Accel. Beams*, **16**:030101, Mar 2013. 56
- [102] M BERZ AND K MAKINO. **COSY INFINITY Version 8.1. User's Guide and Reference Manual.** *Department of Physics and Astronomy MSUHEP-20704, Michigan State University*, 2002. 57, 61
- [103] DANIEL WINKLEHNER, ANDREAS ADELMANN, ACHIM GSELL, TULIN KAMAN, AND DANIELA CAMPO. **Realistic simulations of a cyclotron spiral inflector within a particle-in-cell framework.** *Phys. Rev. Accel. Beams*, **20**:124201, Dec 2017. 59, 60
- [104] ANDREAS ADELMANN, CHRISTIAN BAUMGARTEN, MATTHIAS FREY, ACHIM GSELL, VALERIA RIZZOGLIO, CHRISTOF METZGER-KRAUS, YVES INEICHEN, XIAOYING PANG, STEVE RUSSELL, CHUAN WANG, ET AL. **The OPAL (Object Oriented Parallel Accelerator Library) Framework.** Technical Report PSI-PR-08-02, Paul Scherrer Institut, (2008-2017). 61
- [105] DR. ALEXANDER WITTIG. **FACT FFAG GUI Manual.** Technical report, Particle Accelerator Corporation, (2012). 61
- [106] CAROL JOHNSTONE. private communication. 61, 62, 64
- [107] MK CRADDOCK AND KR SYMON. **Cyclotrons and fixed-field alternating-gradient accelerators.** *Reviews of accelerator science and technology*, **1**(01):65–97, 2008. 63
- [108] DAVID BRUTON, CAROL JOHNSTONE, ROGER BARLOW, REBECCA SEVIOUR, AND ROB EDGECOCK. **A compact and high current FFAG for the production of radioisotopes for medical application.** 2016. 11, 13, 67, 68, 123
- [109] WORLD HEALTH ORGANISATION. **Child growth standards, head circumference for age.** http://www.who.int/childgrowth/standards/second_set/chts_hcfa_boys_p/en/. accessed 2018. 71
- [110] PETER K SIGG. **RF for cyclotrons.** 2006. 85
- [111] SYTZE BRANDENBURG. **RF for Cyclotrons.** In *Accelerators for Medical Applications*, 2015. 85, 90

REFERENCES

- [112] MIKE SEIDEL, S ADAM, A ADELMANN, C BAUMGARTEN, YJ BI, R DOELLING, H FITZE, A FUCHS, M HUMBEL, J GRILLENBERGER, ET AL. **Production of a 1.3 MW proton beam at PSI.** *IPAC10*, page 1309, 2010. 85, 105
- [113] TJ BOYD JR. **Los Alamos Group Report No**, 1982. 85
- [114] SARAH COUSINEAU, JEFF HOLMES, AND YAN ZHANG. **Lecture 3 - RF Acceleration in Linacs. Part 1.** In *Fundamentals of Accelerator Physics and Technology with Simulations and Measurements Lab*, Old Dominion University, 2011. 87
- [115] MIKE SEIDEL AND ANTON C MEZGER. **Performance of the PSI high power proton accelerator.** 89
- [116] NATHANIEL POGUE, ANDREAS ADELMANN, AND LUKAS STINGELIN. **Opal Simulations of the PSI Ring Cyclotron and a Design for a Higher Order Mode Flat Top Cavity.** In *8th Int. Particle Accelerator Conf.(IPAC'17), Copenhagen, Denmark, 14â 19 May, 2017*, pages 3891–3894. JACOW, Geneva, Switzerland, 2017. 89, 116
- [117] WERNER JOHO. **the Cyclotron Facilities at PSI.** <https://indico.psi.ch/getFile.py/access?resId=25&materialId=slides&confId=3484>. accessed 2018. 89
- [118] ANNA KOLANO AND ROGER BARLOW. **A precise beam dynamics model of the PSI injector 2 to estimate the intensity limit.** In *Proc IPAC 2014*, pages 1630–1631. JACoW, 2014. 89
- [119] PAUL SHERRER INSTITUT. **The ring cyclotron.** https://www.psi.ch/media/ImageBoard/igp_39422268f3bbf766680e6f9fc65640ae_bi2005m03_0014_0001_di_v.jpg. accessed 2018. 89
- [120] TAKASHI FUJISAWA, Y KUMATA, I YOKOYAMA, K OGIWARA, I TAKESHITA, S KOHARA, Y CHIBA, Y OIKAWA, AND M NAGASE. **Radio frequency system of the RIKEN ring cyclotron.** 1987. 90
- [121] N SAKAMOTO, M FUJIMAKI, A GOTO, M KASE, O KAMIGAITO, R KOYAMA, K SUDA, K YAMADA, AND S YOKOUCHI. **RF system for heavy ion cyclotrons at RIKEN RIBF.** In *Proc. of the Int. Conf. on Heavy Ion Accelerator Technology (HIAT'09), Venice, Italy*, pages 69–73, 2009. 90

-
- [122] RIKEN NISHINA CENTER FOR ACCELERATOR-BASED SCIENCE. **RIKEN Ring Cyclotron (RRC)**. <https://www.nishina.riken.jp/facility/images/RRC.jpg>. accessed 2018. 90
- [123] YASUSHIGE YANO. **The RIKEN RI beam factory project: A status report**. *Nuclear Instruments and Methods in Physics Research Section B: Beam Interactions with Materials and Atoms*, **261**(1-2):1009–1013, 2007. 105
- [124] M KASE, E IKEZAWA, N FUKUNISHI, O KAMIGAITO, H OKUNO, M KIDERA, H RYUTO, T NAKAGAWA, M KOMIYAMA, N SAKAMOTO, ET AL. **Present status of the riken ring cyclotron**. In *Proceedings of the 17th International Conference on Cyclotrons and their Applications*, 2004. 105
- [125] M OLIVO, E MARIANI, AND JOSEPH SHERMAN. **The PSI 870 keV high intensity Cockcroft–Walton preinjector**. *Review of scientific instruments*, **63**(4):2714–2716, 1992. 105
- [126] J BEVERIDGE, EW BLACKMORE, PF BOSMAN, G DUTTO, W JOHO, RD RICHES, V RODEL, LW ROOT, AND BL WHITE. **Initial operating experience with the TRIUMF 300 keV H-injection system**. *IEEE Transactions on Nuclear Science*, **22**(3):1707–1710, 1975. 105
- [127] HELMUT WIEDEMANN ET AL. *Particle accelerator physics*, **314**. Springer, 2007. 12, 106
- [128] KAREL STRIJCKMANS. **The isochronous cyclotron: principles and recent developments**. *Computerized medical imaging and graphics*, **25**(2):69–78, 2001. 12, 111
- [129] H BLOSSER, D JOHNSON, D LAWTON, F MARTI, R RONNINGEN, AND J VINCENT. **A compact superconducting cyclotron for the production of high intensity protons**. In *Proceedings of the 1997 Particle Accelerator Conference (Cat. No. 97CH36167)*, **1**, pages 1054–1056. IEEE, 1997. 111
- [130] KAIZHONG DING, YF BI, GEN CHEN, YONGHUA CHEN, SHUANGSONG DU, HANSHENG FENG, JIAN GE, OLEG KARAMYSHEV, GALINA KARAMYSHEVA, JUNJUN LI, ET AL. **Study of the beam extraction from superconducting cyclotron SC200**. In *Proc. Cyclotrons*, **2016**, page 87, 2016. 111

REFERENCES

- [131] D VANDEPLASSCHE, W BEECKMAN, W KLEEVEN, S ZAREMBA, JL DELVAUX, L MEDEIROS-ROMAO, JC AMÉLIA, Y JONGEN, AND J FERMÉ. **Extraction simulations for the IBA C70 cyclotron.** In *these Proceedings*, 2007. 111
- [132] S ALFREDSON, F MARTI, P MILLER, D POE, AND G STORK. **Electrostatic septum for kilowatt heavy ion beams.** In *AIP Conference Proceedings*, **600**, pages 133–135. AIP, 2001. 111
- [133] J DEKAMP AND F MARTI. **Thermomechanical calculations of a cyclotron deflector.** In *Proceedings of the 1997 Particle Accelerator Conference (Cat. No. 97CH36167)*, **1**, pages 278–280. IEEE, 1997. 111
- [134] PAULI HEIKKINEN. **Injection and extraction for cyclotrons.** 1994. 112
- [135] L DENIOU ET AL. **The MAD-X Program, User’s Reference Manual.** *Geneva, Switzerland*, 2017. 122
- [136] VECTOR FIELDS. **OPERA-3d Reference Manual.** *Vector Fields Limited, England*, 2004. 123
- [137] ROB EDGECOCK. private communication. 13, 123
- [138] MICROWAVE STUDIO. **Computer Simulation Technology (CST).** *Online: www.cst.com*, 2015. 124
- [139] LAURIE S WATERS ET AL. **MCNPX user’s manual.** *Los Alamos National Laboratory*, 2002. 124
- [140] ALAN LETCHFORD, ALESSIO BOSCO, RICHARD D’ARCY, STEPHEN GIBSON, MICHAEL DUDMAN, SCOTT LAWRIE, DAN FAIRCLOTH, PETER SAVAGE, SIMON JOLLY, GARY BOORMAN, ET AL. **Status of the RAL Front End Test Stand.** 2015. 124
- [141] **The Ionising Radiations Regulations 2017.** http://www.legislation.gov.uk/ukxi/2017/1075/pdfs/ukxi_20171075_en.pdf. 124
- [142] PATRICK HORTON AND DAVID EATON. *Design and Shielding of Radiotherapy Treatment Facilities.* 2053-2563. IOP Publishing, 2017. 124